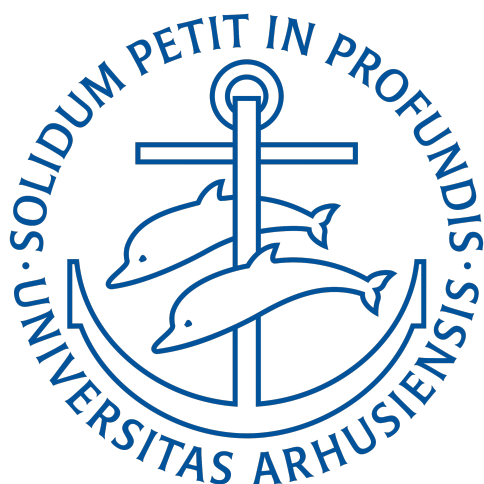


Synthesis, Structure and Electronic
Properties of Novel Single Layer Transition
Metal Chalcogenides



Fabian Arnold

PhD Dissertation

November 2017

Aarhus University

Abstract

The discovery of graphene and the possibility of the synthesis of high quality samples has shifted the focus in the physics community from the three-dimensional (3D) world to the new and remarkable properties of two-dimensional (2D) materials. Shortly after the synthesis of graphene, several other 2D materials with significantly different and fascinating properties have been synthesized¹⁻³. These properties, and the ability to synthesize atomically thin layers of these materials, make them attractive for a variety of applications including optoelectronic and spintronics^{4,5}. However, the synthesis of 2D materials is rather challenging, and the quality and properties of the material does not solely depend on the growth conditions, but also the substrate upon which the single layer (SL) is synthesized^{6,7}.

In this thesis the epitaxial growth of thin film iron chalcogenides (IC), in particular FeSe on Bi₂Se₃ and FeTe on Bi₂Te₃ are presented, and the synthesis of SL transition metal dichalcogenide (TMDC) V_{1+x}S₂ on Au(111) is demonstrated and studied. By means of angle-resolved photoemission spectroscopy (ARPES), X-ray spectroscopy (XPS), X-ray photoelectron diffraction (XPD), scanning tunneling microscopy (STM) and low energy electron diffraction (LEED), the electronic and crystal structure of these materials are characterized to provide complementary data. The experimental results are compared with density-functional theory calculations (DFT) and simulated XPD patterns.

The structural and electronic properties indicate a synthesis of 3-5 monolayers (MLs) FeSe on Bi₂Se₃ with the applied growth method. Photoemission results point to the persistence of a heavily n-doped topological surface state of Bi₂Se₃ beneath the FeSe overlayer. Moreover, no sign of a superconducting gap for any investigated thickness is found at a temperature of 5 K.

The photoemission spectra of cleaved bulk Fe_{1.08}Te is used to disentangle the photoemission data of FeTe thin films on Bi₂Te₃, which grow in three domains, rotated by 0, 120°, and 240° with respect to the high symmetry direction of the substrate. Furthermore, the Fermi contour of the FeTe thin films can be constructed by using the photoemission results from bulk Fe_{1.08}Te. By monitoring the development of the substrate's electronic structure upon covering the surface with FeTe, indications of charge transfer from the thin film to the substrate are found and a well-defined strong electron doped topological surface state is observed. Upon doping with alkali metals no significant change of the film's electronic structure is observed. This behavior can be ascribed to the high density of states of the thin film close to the Fermi level and is further supported by ab-initio calculations.

The structural characterization of epitaxially grown SL V_{1+x}S₂ on Au(111) reveals the existence of three distinct phases introduced simply by annealing in ultra high vacuum (UHV). While the first two phases can be identified as the octahedral (1T) configuration with slightly different lattice constant, the third phase exhibits a structural morphology, which is not in agreement with any V_{1+x}S₂ bulk compound we are aware of. We attribute the phase transitions to S loss from the V_{1+x}S₂ single layer during the annealing process. Furthermore, the electronic band structure shows that all the phases are metallic.

Resumé

Opdagelsen af graphen og mulighederne for at fremstille prøver af høj kvalitet har medført et ændret fokus i fysikerkredse fra den tredimensionelle (3D) verden til todimensionelle (2D) materialer med nye bemærkelsesværdige egenskaber. Efter fremstillingen af graphen blev demonstreret er adskillige andre 2D materialer med anderledes og fascinerende egenskaber blevet syntetiseret¹⁻³. Disse egenskaber og muligheden for at fremstille materialer med atomar tykkelse gør materialerne særdeles attraktive for adskillige anvendelsesområder såsom optoelektronik og spintronik^{4,5}. Syntesen af 2D materialer er dog forholdsvis udfordrende. Kvaliteten og egenskaberne af et given materiale afhænger ikke blot af syntesebetingelserne men også af substratet for 2D materialet^{6,7}.

I denne afhandling præsenteres epitaksial vækst af tynde film af jernchalcogenider såsom FeSe på Bi₂Se₃ og FeTe på Bi₂Te₃, og syntesen af et enkelt lag af overgangsmetalchalcogeniden V_{1+x}S₂ på Au(111) demonstreres og studeres. Den elektroniske og krystallinske struktur af disse materialer karakteriseres med de komplementære teknikker vinkelopløst fotoemissionsspektroskopi (ARPES), røntgenspektroskopi (XPS), røntgenfotoelektrondiffraktion (XPD), skannende tunnelmikroskopi (STM) og lavenergi elektrondiffraktion (LEED). De eksperimentelle resultater sammenlignes med beregninger indenfor tæthedsfunktionalteori (DFT) og simulerede XPD mønstre.

De strukturelle og elektroniske egenskaber indikerer vækst af 3-5 mono-

lag (MLs) af FeSe på Bi_2Se_3 med den anvendte syntesemetode. Resultater fra fotoemission peger på en vedholdende kraftigt n-doteret topologisk overfladetilstand i Bi_2Se_3 under FeSe laget. Der er ikke fundet tegn på et superledende gab for nogle af de undersøgte tykkelser ved en temperature på 5 K.

Fotoemissionsspektre fra en kløvet bulk krystal af $\text{Fe}_{1.08}\text{Te}$ bruges til at skelne fotoemissionsdata fra FeTe tyndfilm på Bi_2Te_3 , som gror i tre domæner roteret med vinkler på 0, 120° og 240° med hensyn til højsymmetriske retninger i substratet. Det var også muligt at konstruere Fermikonturen af FeTe tyndfilm ved hjælp af fotoemissionsdata fra bulk $\text{Fe}_{1.08}\text{Te}$. Der blev fundet indikationer på ladningsoverførsel fra tyndfilmen til substratet, og en veldefineret kraftigt elektrondoteret topologisk overfladetilstand blev observeret ved at følge udviklingen af substratets elektroniske struktur efter vækst af FeTe på overfladen. Der blev ikke fundet nogen mærkbar ændring af filmens elektroniske struktur efter dotering med alkalimetaller. Denne opførsel tilskrives tyndfilmens høje tilstandstæthed tæt på Ferminiveaue, hvilket understøttes yderligere af ab-initio beregninger.

Den strukturelle karakterisering af enkelte lag af V_{1+x}S_2 , fremstillet ved hjælp af epitaksial vækst på Au(111), afslører tre distinkte faser som frembringes ved simpel opvarmning under ultrahøj vakuum (UHV) betingelser. De to første faser identificeres som den octahedrale (1T) konfiguration med en smule anderledes gitterkonstant. Den tredje fase udviser en strukturel morfologi, der ikke stemmer overens med nogle V_{1+x}S_2 bulk komponenter, som vi kender til. Vi fortolker faseovergangene som en udskillelse af S fra V_{1+x}S_2 monolaget under opvarmningsprocessen. Den elektroniske struktur viser at alle faserne er metalliske.

Preface

This dissertation has been submitted to the faculty of Science and Technology at Aarhus University in Denmark in order to fulfil the requirements for obtaining a Ph.D. degree in Physics. The research described herein was conducted under the supervision of Professor Philip Hofmann at the Department of Physics and Astronomy, Aarhus University, Denmark, between December 1st 2014 to November 30th 2017.

The majority of the work has been performed at the SGM3 beamline for angle-resolved photoemission on ASTRID2 at the Institute for Storage Ring Facilities in Aarhus (ISA) and at a stand alone STM-chamber dedicated for sample preparation and characterization located in the SGM3 laboratory. Parts of the scanning tunneling microscopy data in this thesis were obtained in collaboration with the group headed by Professor Alexander Khajetoorians (Institute for Molecules and Materials at Radboud University, Nijmegen/Netherland) and the group headed by Professor Roland Wiesendanger (Interdisciplinary Nanoscience Center Hamburg (INCH), Universität Hamburg, Hamburg/Germany). A period of time was spent at international synchrotron facilities, in particular at the SuperESCA beamline at the Elettra synchrotron radiation facility in Trieste (Italy) for X-ray photoelectron diffraction experiments.

Acknowledgements

The work presented in this dissertation is the product of a three-year-long journey where I had the pleasure to work and collaborate with amazing and talented people from all around the world. I am deeply grateful to all the people mentioned below.

First and foremost I want to thank my advisor Philip Hofmann for giving me the opportunity to do a Ph.D. in his group, for involving me in many interesting projects and for given me the freedom to pursue my own ideas. I really appreciate all his contributions of time, support, ideas, scientific guidance and invaluable discussions.

I am grateful to all the people, past and present, from the group for making long hours in the dark basement of the physics department so lovely and memorable. Special thanks to Marco Bianchi for being a great mentor and introducing me into the world of UHV and ARPES and for cheering me up if the experiment did not work as planned. Thanks to Jill Miwa, who is probably the nicest Canadian in the world. I will always remember the great scientific discussions and her great sense of humor. Also a special thanks to Charlotte Sanders for supporting me in my work with such a positive spirit. It was a pleasure working with her on so many fruitful project. I would further like to thank all other members of the group: Maciej Dendzik for being a great roommate during the conferences and external beamtimes; Matteo Michiardi for being the best foosball partner; Antonija G. Cabo for joining me for many social events

and having a weekly beer with me in the friday bar; Arlette S. Ngankeu for being a great office mate during the last three years; Raluca M. Stan for fun times at the STM-chamber, Sanjoy Kr Mahatha for his help in the lab and his positive and supporting attitude, Henriette E. Lund for being an awesome and supportive Master Student, Søren Ulstrup for nice discussions about science and beer, Federico Andreatta for his kind words, Davide Curcio for sharing his fitting skills with me, Ann Julie Holt for showing me the true (Norwegian) meaning of my name, Klara Volckaert for her laugh and her positive spirit and Kévin Guilloy for his software skills. Thanks to all the ISA people and the workshop.

I am indebted to all the groups I have collaborated with, both internally at the Aarhus University and externally. A special thanks goes to Jonas Warmuth for the great collaboration on the FeTe project. I would also like to thank all the other people I have collaborated with: Martin Bremholm, Alex Kajetoorians, Andreas Eich, Umut Kamber, Jens Wiebe, Roland Wiesendanger, Jan Honolka, Jan Fikáček, Tim Wehling, Albert Bruix, Daniel Wegner, Silvano Lizzit, Paolo Lacovig, Luca Bignardi, Harsh Bana, Elisabetta Travaglia and Daniel Lizzit.

All of you have made the last three years highly memorable, both scientifically and personally.

I would like to extend my deepest gratitude to my parents, Peter and Birgit, and my sister Silke, for the incredible support and backup in the last three years and throughout my whole life. Thanks to my aunt Kirsten for her supportive phone calls. Many thanks to the rest of my family and all of my friends for trying to understand what I do. And finally, I want to thank my girlfriend Dorette for her love, support and patience when I need it the most. You remind me that science is not the only thing in the world.

Fabian Arnold

30.11.2017. Aarhus, Denmark

List of Publications

Publications relevant for the thesis

I F. Arnold, R. Stan, A. Bruix, S. Mahatha, H. E. Lund, D. Curcio, H. Bana, E. Travaglia, L. Bignardi, P. Lacovig, D. Lizzit, M. Bianchi, J. A. Miwa, M. Bremholm, S. Lizzit, Ph. Hofmann, and C. Sanders. Crystalline and electronic structure of reversible phase change transitions of single layer $1T-V_{1+x}S_2$ on Au(111). *In manuscript*.

I performed ARPES, XPS, XPD, STM and LEED experiments and analyzed the experimental data. I wrote the first draft of the manuscript.

II F. Arnold, J. Warmuth, M. Michiardi, J. Fikáček, M. Bianchi, J. Hu, Z. Mao, J. A. Miwa, U. R. Singh, M. Bremholm, R. Wiesendanger, J. Honolka, T. Wehling, J. Wiebe and Ph. Hofmann. Electronic Structure of $Fe_{1.08}Te$ bulk crystals and doping dependence of epitaxial FeTe thin films on Bi_2Te_3 . *Submitted*.

I performed ARPES and LEED experiments and analyzed the experimental data. I wrote the first draft of the submitted manuscript.

III A. Eich, N. Rollfing, F. Arnold, C. Sanders, P. R. Ewen, M. Bianchi, M. Dendzik, M. Michiardi, J.-L. Mi, M. Bremholm, D. Wegner, Ph. Hofmann, and A. A. Khajetoorians. Absence of superconductivity in ultrathin layers of FeSe synthesized on a topological insulator. *Phys. Rev. B*, 94:125437, 2016.

I performed ARPES and LEED experiments and analyzed the experimental data. I wrote the first draft of the chapter "Electronic Structure Characterization" and parts of the chapter "Structural Characterization" of the submitted manuscript.

Other publications

1. H. Thierschmann, F. Arnold, M. Mittermüller, L. Maier, C. Heyn, W. Hansen, H. Buhmann and L. W. Molenkamp. Thermal control and generation of charge currents in coupled quantum dots. *Phys. Status Solidi A* 213:582–590, 2016.
2. H. Thierschmann, R. Sánchez, B. Sothmann, F. Arnold, C. Heyn, W. Hansen, H. Buhmann and L. W. Molenkamp. Three-terminal energy harvester with coupled quantum dots. *Nat. Nanotechnol.*, 10:854–858, 2015.
3. H. Thierschmann, F. Arnold, M. Mittermüller, L. Maier, C. Heyn, W. Hansen, H. Buhmann and L. W. Molenkamp. Thermal gating of charge currents with Coulomb coupled quantum dots. *New J. Phys.*, 17:113003, 2015.
4. F. Albert, C. Hopfmann, A. Eberspächer, F. Arnold, M. Emmerling, C. Schneider, S. Höfling, A. Forchel, M. Kamp, J. Wiersig, and S. Reitzenstein. Directional whispering gallery mode emission from Limaçon-shaped electrically pumped quantum dot micropillar lasers. *Appl. Phys. Lett.* 101:021116, 2012.

Abbreviations

2D	Two-dimensional
3D	Three-dimensional
ARPES	Angle-resolved photoemission spectroscopy
ASTRID	Aarhus Storage Ring in Denmark
BCS	Bardeen, Cooper and Schrieffer
BZ	Brillouin zone
CB	Conduction band
CBM	Conduction band minimum
CDW	Charge density wave
DFT	Density-functional theory calculation
DMDS	Dimethyl disulfide
EDAC	Electron Diffraction in Atomic Clusters
EDC	Energy distribution curve
ENS	Entrance slit
EXS	Exit slit
FWHM	Full width half maximum
HFM	Horizontal focusing mirror
HOPG	Highly ordered pyrolytic graphite
IC	Iron chalcogenide
IMFP	Inelastic mean free path
LDOS	Local density of states
LEED	Low energy electron diffraction
LL	Load-lock

MBE	Molecular beam epitaxy
MC	Main chamber
MDC	Momentum distribution curve
ML	Monolayer
MCP	Multichannel plate
PFM	Post focusing mirror
PC	Preparation chamber
SBZ	Surface Brillouin zone
SGM	Spherical grating monochromator
SL	Single layer
SS	Surface state
STM	Scanning tunneling microscopy
STS	Scanning tunneling spectroscopy
UV	Ultraviolet
TMDC	Transition metal dichalcogenide
VB	Valence band
VBM	Valence band maximum
VFM	Vertical focusing mirror
UHV	Ultra-high vacuum
XPD	X-ray photoelectron diffraction
XPS	X-ray spectroscopy

Contents

Abstract	i
Resumé	iii
Preface	v
Abbreviations	xi
1 Introduction	1
1.1 Two-Dimensional Materials	1
1.2 Thesis Outline	2
2 Experimental Techniques	5
2.1 Angle-Resolved Photoemission Spectroscopy	5
2.1.1 The Photoemission Process	6
2.1.2 Spectral Function	8
2.1.3 X-ray Spectroscopy: Photoemission from Core Levels	10
2.1.4 ARPES Spectra Acquisition and Analysis	12
2.2 Experimental Setup	15
2.2.1 ASTRID2 and SGM3 Beamline	16
2.2.2 SGM3 Endstation	17
2.2.3 STM-Chamber	18
2.3 Techniques for Structural Analysis	19
2.3.1 Scanning Tunneling Microscopy	20
2.3.2 Low Energy Electron Diffraction	21
2.3.3 X-Ray Photoelectron Diffraction	23

3	Iron Chalcogenides	27
3.1	Introduction	27
3.1.1	2D Iron Chalcogenides	27
3.1.2	Crystal and Electronic Structure of Bi_2Se_3 and Bi_2Te_3	28
3.1.3	Crystal and Electronic Structure of FeSe and FeTe	30
3.2	FeSe Thin Films on Bi_2Se_3	34
3.2.1	Growth of FeSe Thin Films on Bi_2Se_3	34
3.2.2	Structural Analysis of FeSe Thin Films on Bi_2Se_3	34
3.2.3	Electronic Structure of FeSe Thin Films on Bi_2Se_3	38
3.3	Bulk $\text{Fe}_{1.08}\text{Te}$	43
3.3.1	Structural and Electronic Analysis of Bulk $\text{Fe}_{1.08}\text{Te}$	43
3.4	FeTe Thin Films on Bi_2Te_3	49
3.4.1	Growth of FeTe Thin Films on Bi_2Te_3	49
3.4.2	Structural Analysis of FeTe Thin Films on Bi_2Te_3	49
3.4.3	Electronic Structure of FeTe Thin Films on Bi_2Te_3	51
3.4.4	Electronic Structure of Alkali Doped FeTe Thin Films on Bi_2Te_3	55
3.5	Conclusion Iron Chalcogenides	57
4	Single Layer V_{1+x}S_2 on $\text{Au}(111)$	59
4.1	Introduction	59
4.1.1	Bulk and Two-Dimensional Transition Metal Dichalcogenides	59
4.1.2	Crystal and Electronic Structure of V_{1+x}S_2	61
4.2	Synthesis of Single Layer V_{1+x}S_2 on $\text{Au}(111)$	63
4.3	Structural Analysis of Single Layer V_{1+x}S_2 on $\text{Au}(111)$	65
4.3.1	Three Phases: Characterization with STM and LEED	65
4.3.2	Structural Determination by XPS and XPD	78
4.4	Electronic Structure of Single Layer V_{1+x}S_2 on $\text{Au}(111)$	87
5	Conclusion and Outlook	93
5.1	Summary	93
	Bibliography	97

Chapter 1. Introduction

This chapter provides a general introduction into two-dimensional (2D) materials and a brief outline about the chapters presented in this thesis.

1.1 Two-Dimensional Materials

2D materials are by definition substances which solely consist of a few layers of atoms. Due to confinement in two-dimensions electrons can move freely along the plane of the interface but, the motion is restricted in the third dimension. This simple example already demonstrates that thinning down a macroscopic bulk crystal in one-dimension may modify the electronic structure of the material and that dimensionality is in general a defining parameter for a material's properties. For decades, the existence and stability of 2D materials were debated, and it was commonly assumed that 2D crystalline materials might not be experimentally realized at finite temperature⁸.

However, the discovery of graphene, a single layer (SL) of graphite, showed that the theoretical restriction solely apply to infinite crystals and that a rippled structure could render 2D materials stable^{9,10}. Surprisingly, graphene has a rather long history and was first theoretical described in 1947¹¹. Around twenty years later graphene was unintentionally observed by low energy electron diffraction (LEED) and Auger spectroscopy experiments on single crystals of platinum^{12,13} and nickel¹⁴ but disregarded as unwanted contamination forming from carbon segregation from the bulk crystal during annealing. The rise of 2D materials started in 2004 when Geim and Novoselov intentionally isolated graphene by exfoliating graphite crystals with the scotch tape method¹⁵. The enormous interest in graphene is based on its unique combination of electronic and structural properties making graphene a flexible 2D conductor with high mechanical strength and therefore a promising candidate for electronic applications^{16,17}. Furthermore, graphene is the base for novel and interesting physics such as quantum Hall effect^{18,19} and massless Dirac fermions²⁰. The importance of graphene

was underlined by the Nobel prize in physics for Geim and Novoselov in 2010²¹.

In the light of this success, the ideas and methodology obtained from graphene studies were extended to other layered materials consisting also of weakly van der Waals bonded layers which can be exfoliated from the bulk crystal. Several materials were successfully synthesized as 2D materials and showed electronic and structural properties that are significantly different from their bulk parent compound, and possibly interesting for novel technologies. Transition metal dichalcogenides (TMDCs) and iron chalcogenides (ICs) were among the first new materials to be isolated in the 2D limit. Both material systems exhibit intriguing novel properties beyond graphene such as high temperature interfacial superconductivity, band gap opening and spin orbit coupling effects and are therefore interesting candidates to study in more detail the electronic properties of 2D confined electrons^{1-3, 22, 23}.

In this thesis, epitaxial growth procedures are explored to synthesize high quality 2D materials in particular, for the thin film ICs FeSe on Bi₂Se₃ and FeTe on Bi₂Te₃ and as well for SL V_{1+x}S₂ on Au(111). The growth method and crystal structure are studied by scanning tunneling microscopy (STM), low energy electron diffraction (LEED), X-ray spectroscopy (XPS) and X-ray photoelectron diffraction (XPD). The electronic structure of these systems is investigated with high-resolution, synchrotron-based, angle-resolved photoemission spectroscopy (ARPES). A brief introduction to the materials explored in this thesis will be provided at the beginning of the corresponding chapters.

1.2 Thesis Outline

This thesis contains a variety of surface science methods and experiments to investigate the crystalline and electronic structure of the 2D ICs FeSe and FeTe grown on Bi₂Se₃ and Bi₂Te₃ (chapter 3), respectively, and the SL TMDC V_{1+x}S₂ on Au(111) (chapter 4). In chapters 3 and 4, a separate introduction for the respective topics, as well as a list of the collaborators on the project, are given before the results and the discussion are presented. In the following an overview of the structure of this thesis is outlined:

- **Chapter 2** introduces the experimental techniques used in this thesis for the electronic and structural characterization of the studied materials. The focus is on ARPES and XPS and the underlying physics. Moreover, the experimental setup for the ARPES measurement and the SGM3 beamline at ASTRID2 are

discussed. Lastly, the structural characterization methods STM, LEED and XPD are briefly described. Parts of this chapter might be similar to those given in Ref.²⁴. Therefore, sections of text bear close resemblance and the figures might be identical to Ref.²⁴.

- **Chapter 3** presents methods for the synthesis of the thin film, FeSe on Bi₂Se₃ in section 3.2 and FeTe on Bi₂Te₃ in section 3.4. The morphology and the electronic structure of the thin films is discussed and in the case of FeTe compared with the results of the bulk parent compound from section 3.3. Section 3.2 is naturally inspired from the article [III] listed in the publications section and Ref.²⁴; section 3.3 and 3.4 present results from the article [II] listed in the publications section. Therefore, sections of text bear close resemblance and the figures might be identical to [II], [III] and Ref.²⁴.
- **Chapter 4** is devoted to SL V_{1+x}S₂ on Au(111) synthesized in three distinct crystalline phases. The crystal structure and morphology are characterized and a structural model is designed for each of the three phases. Further, the electronic band structure results are compared with density-functional theory calculations (DFT). Chapter 4 is naturally inspired by results from the article [I] listed in the publications section. Therefore, sections of text bear close resemblance and the figures might be identical to [I].
- **Chapter 5** summarizes the results of this thesis and gives a brief outlook for future and planned work on the presented material systems.

Chapter 2. Experimental Techniques

The focus of this chapter is on the theoretical description and the experimental setup of ARPES, which is the main experimental technique used throughout this thesis. The underlying physical principles of the photoemission process are presented, followed by a description of the experimental setup for ARPES at the *Aarhus Storage Ring in Denmark 2* (ASTRID2) lightsource. Lastly, a brief introduction to complementary surface sensitive techniques such as XPS, STM, LEED, and XPD is presented.

2.1 Angle-Resolved Photoemission Spectroscopy

The underlying principle of ARPES is the photoelectric effect which was discovered by Hertz²⁵ and later explained by Einstein²⁶. Here, monochromatic light with sufficient energy is shone on the material of interest which leads to the photoemission of electrons from occupied electronic states of the material. The key aspect of an ARPES experiment is the possibility to access the electronic structure of the material by analyzing the kinetic energy and the momentum of the photoemitted electron with an electron analyzer. Besides measuring the electronic structure, ARPES can also be exploited to provide information about fundamental particle interactions such as strong electron correlations or electron-phonon coupling. This section will discuss in detail the underlying physical principles of ARPES, while the experimental description of the ARPES setup is given in section 2.2.

2.1.1 The Photoemission Process

In simple words photoemission is the process of emitting electrons from a material by interaction with photons. An intuitive picture of the underlying processes is provided by the phenomenological three-step model of photoemission²⁷. In the first step, an electron is excited from its initial state to a final state in the material by absorbing a photon. The kinetic energy of the final state electron has to fulfill energy conservation as shown in fig. 2.1(a) and is represented in the following equation:

$$E_{kin} = h\nu - E_{bin} - \Phi_w, \quad (2.1)$$

where $h\nu$ is the energy of the absorbed photon, E_{bin} is the binding energy of the electron in the initial state and Φ_w is the work function of sample. Photon energies in the range of 0.1-2.0 keV are typically used to excite strongly bonded core level electrons which would be observed in the energy spectrum as well defined non-dispersive peaks. The binding energy position as well as the shape of the core level peak are element specific and even sensitive to small changes in the chemical environment. This technique is called XPS and can be used for chemical characterization of samples or compounds. Lower photon energies (5-100 eV) are usually used to gain access to the dispersing valance bands near the Fermi level which is exploited in ARPES measurements. Note that according to equation 2.1, the photon energy has to be at least greater than the work function Φ_w (usually 4-5.5 eV) to emit photoelectrons and to measure ARPES spectra.

In the second step, the final state photoelectron migrates to the surface and is scattered elastically and inelastically. The probability of scattering events is described by the inelastic mean free path (IMFP) and follows a “universal curve”²⁸. For energies used in ARPES experiments scattering events occur around every 5-7 Å, making ARPES a highly surface sensitive technique. It is worth noting that the IMFP exhibits a global minimum at a kinetic energy of around 70 eV which enables one to tune the sensitivity to measure either the bulk or surface properties in ARPES and XPS measurements.

The third and final step is sketched in fig. 2.1(b). The final state electron is transmitted into a free electron state in the vacuum by leaving the sample through the surface. For simplicity reasons the potential change between surface and vacuum is usually modeled as a step potential, neglecting the more complicated potential environment at the surface-vacuum interface. For momentum resolved techniques such as ARPES it is worth mentioning that the surface-vacuum interface breaks the

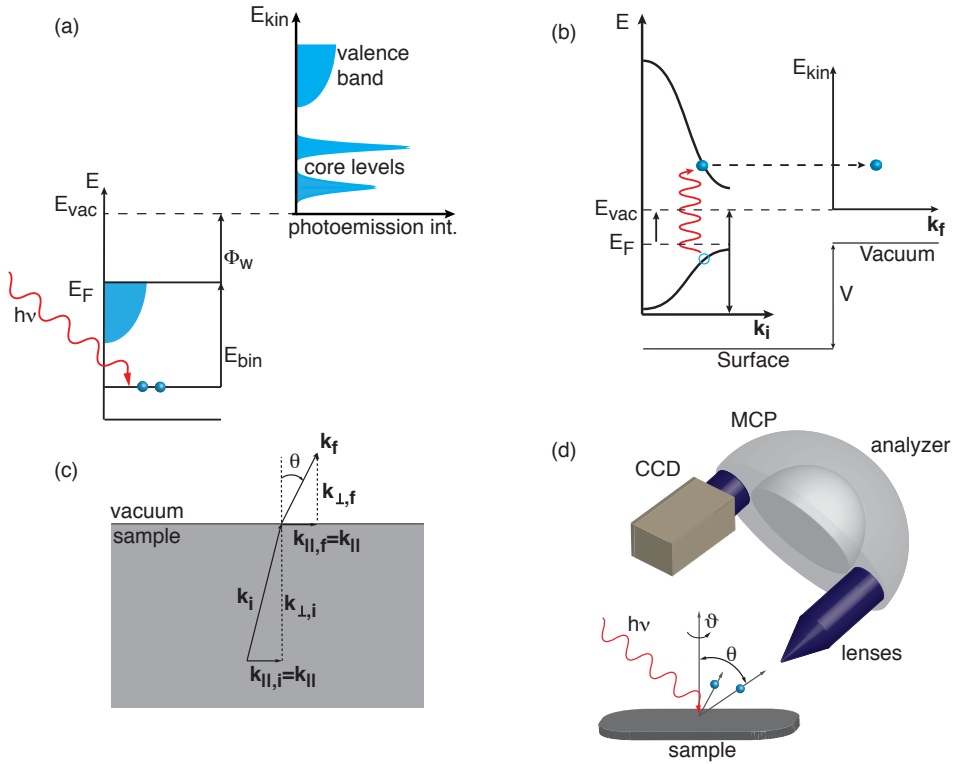


Figure 2.1: (a) Energy scheme for the photoemission process. A photon with the energy $h\nu$ excites an electron (blue circle) in the solid. The detected kinetic energy E_{kin} of the photoelectron is a function of the energy of the photon, the binding energy E_{bin} and the work function of the material Φ_w . Figure (a) is inspired by Ref.²⁷. (b) Schematic of the photoemission process explained by the three step model. From the valence band an electron is excited by a direct optical transition. The lattice momentum enables matching the initial wave function of the electron with a free-electron final state in the vacuum. The potential step V describes the surface-vacuum interface, which introduces a potential offset between the vacuum and crystal. (c) Refraction process of the photoelectron at the material-vacuum transition. The parallel component to the surface \mathbf{k}_{\parallel} is conserved, the perpendicular component \mathbf{k}_{\perp} is not conserved. (d) Schematic of the ARPES measurement setup with a light beam shone on a sample. The photoelectrons are emitted from the sample in an azimuthal (ϑ) and polar (θ) angle and then focused by electrostatic lenses before enter the entrance slit of the analyzer. The electrons are discriminated by the electric field between the two hemispheres of the analyzer leading to angle and energy resolution. A multichannel plate (MCP) works as amplifier of the photoelectrons' signal and produces an image on a phosphor screen. A CCD camera acquires finally the image produced on the screen.

translational symmetry of the system which leads to a change in the component of momentum perpendicular to the surface \mathbf{k}_\perp whereas the parallel component \mathbf{k}_\parallel is conserved as shown in fig. 2.1(c). Considering the negligible small photon momentum compared to the electron momentum in ARPES the information about the valence band dispersion can be obtained by measuring the distribution of emitted photoelectrons in terms of azimuthal (ϑ) and polar (θ) angle (fig. 2.1(d)) and the kinetic energy of the photoelectron E_{kin} :

$$\mathbf{k}_\parallel = \mathbf{k}_{\parallel,i} = \mathbf{k}_{\parallel,f} = \sqrt{\frac{2m_e E_{kin}}{\hbar}} \sin(\theta) (\cos(\vartheta)\hat{\mathbf{x}} + \sin(\vartheta)\hat{\mathbf{y}}), \quad (2.2)$$

where m_e is the free electron mass. To first approximation, equation 2.1 and 2.2 can perform the transformation from angular to momentum space $I(\vartheta, \theta, E_{kin}) \rightarrow I(\mathbf{k}_\parallel, E_{bin})$, if \mathbf{k}_\perp is neglected. Therefore, this method is convenient to measure the dispersion in electronic band structure of 2D electrons in ICs or SL TMDCs^{29,30}.

2.1.2 Spectral Function

The excitation of a photoelectron leads to the formation of a photohole that is left behind and to a perturbation of the remaining system²⁷. The light-matter interaction is hereby described by a Hamiltonian \mathcal{H}_{int} of the form:

$$\mathcal{H}_{int} = \frac{e}{2m_e c} (\mathbf{A} \cdot \mathbf{p} + \mathbf{p} \cdot \mathbf{A}), \quad (2.3)$$

where \mathbf{p} is the electronic momentum operator and \mathbf{A} the electromagnetic vector potential and c the speed of light in the vacuum. We assume that the electron is instantly removed from the system and is not interacting with the remaining particles meaning that the effective potential is not affected during the photoemission process. This so called sudden approximation is in principle solely valid for high energy photons but simplifies the problem here²⁷. The photoelectron can therefore be regarded as a single particle with an initial state $\Phi_i^{\mathbf{k}}$ and a final state wave function $\Phi_f^{\mathbf{k}}$. The left behind photohole is, however, described as a (N-1) particle term with an initial state ψ_i^{N-1} and final ionized state m presented by ψ_m^{N-1} . And the total initial ψ_i^N and final state ψ_f^N can be written as:

$$\psi_i^N = A \Phi_i^{\mathbf{k}} \psi_i^{N-1} \quad (2.4)$$

and:

$$\psi_f^N = A \Phi_f^{\mathbf{k}} \psi_m^{N-1}, \quad (2.5)$$

where A is an antisymmetry operator for the Pauli principle. The transition probability for an optical excitation between these states in an external electromagnetic field can be determined by Fermi's Golden rule and the Hamiltonian in equation 2.3:

$$\begin{aligned}\Gamma_{i \rightarrow f} &= \frac{2\pi}{\hbar} |\langle \psi_f^N | \mathcal{H}_{int} | \psi_i^N \rangle|^2 \delta(E_f^N - E_i^N - h\nu) \\ &= \frac{2\pi}{\hbar} |M_{i,f}^{\mathbf{k}}|^2 |\langle \psi_m^{N-1} | \psi_i^{N-1} \rangle|^2 \delta(E_{kin} + E_m^{N-1} - E_i^N - h\nu),\end{aligned}\quad (2.6)$$

where $|\langle \psi_m^{N-1} | \psi_i^{N-1} \rangle|^2$ is the probability that the photohole is left excited in the m state after the excitation, the initial and final energies of the N -particle system are described by $E_i^N = E_i^{N-1} - E_{bin}^{\mathbf{k}}$ and $E_f^N = E_m^{N-1} + E_{kin}$, with $E_{bin}^{\mathbf{k}}$ the binding energy with the momentum \mathbf{k} and the kinetic energy E_{kin} of the photoelectron, lastly the term $M_{i,f}^{\mathbf{k}} = \langle \Phi_f^{\mathbf{k}} | \mathcal{H}_{int} | \Phi_i^{\mathbf{k}} \rangle$ is the single-particle matrix element. The integration over all possible transitions from the initial to final states is proportional to the observed photoemission intensity in ARPES and can be determined by considering the Fermi-Dirac distribution f_{FD} :

$$\mathcal{I}(\mathbf{k}, E_{kin}) \propto \sum_{i,f} f_{FD}(E_i) \Gamma_{i \rightarrow f} = f_{FD}(E_{kin}) \sum_{i,f} |M_{i,f}^{\mathbf{k}}|^2 \mathcal{A}(\mathbf{k}, E_{kin}), \quad (2.7)$$

with the photohole spectral function \mathcal{A} :

$$\mathcal{A}(\mathbf{k}, E_{kin}) = \sum_m |\langle \psi_m^{N-1} | \psi_i^{N-1} \rangle|^2 \delta(E_{kin} + E_m^{N-1} - E_i^N - h\nu). \quad (2.8)$$

Equation 2.7 shows that the intensity of the ARPES signal solely depends on the spectral function \mathcal{A} and the matrix element $M_{i,f}^{\mathbf{k}}$. The matrix element describes the light-matter interaction and depends on the polarization, the energy and the incident angle of the incoming light and is therefore capable of modulating the intensity of the ARPES spectra or even lead to full suppression of photoemission features^{29,31}. The spectral function in equation 2.8 can be rearranged to a more usable form by applying the Green function formalism:

$$\mathcal{A}(\mathbf{k}, \omega) = \frac{\pi^{-1} |\sum''(\mathbf{k}, \omega)|}{(\hbar\omega - \epsilon(\mathbf{k}) - \sum'(\mathbf{k}, \omega))^2 + \sum''(\mathbf{k}, \omega)^2}, \quad (2.9)$$

where $\hbar\omega$ is the electron energy with respect to the Fermi level, $\epsilon(k)$ is the single-particle dispersion, $\sum'(\mathbf{k}, \omega)$ and $\sum''(\mathbf{k}, \omega)$ are the real and imaginary part of the

electronic self-energy $\Sigma(\mathbf{k}, \omega)$, respectively. The real part of the self energy influences the band velocity and so the dispersion and curvature of the spectra. The imaginary part describes the finite lifetime due to many body effects such as electron-electron, electron-phonon and electron-impurity interactions. The many body effect is inversely proportional to the spectral width meaning the broader the feature the smaller the lifetime. Thus photoemission intensity provides not only information about the band structure but also about quasiparticle interactions during the photoemission process. Note that for constant-energy cuts, also called momentum distribution curves, through the spectral function posses a Lorentzian. For the simplest case a linear energy dispersion $\epsilon(\mathbf{k}) = v\hbar k$, equation 2.9 exhibits the Lorentzian maximum at $k_{peak} = \frac{1}{v\hbar}(\hbar\omega - \Sigma'(\omega))$ and has a full width at half maximum of $FWHM = 2 \left| \frac{\Sigma''(\omega)}{v\hbar} \right|$.

2.1.3 X-ray Spectroscopy: Photoemission from Core Levels

A further photoemission technique, besides ARPES, is XPS which is photoemission from deeply bounded core level electrons in a photon energy range of 0.1 keV to 2.0 keV. The main difference between ARPES and XPS is the lack of momentum dispersion of the locally bounded core level electrons. The binding energies of XPS spectra is not only element specific but also holds important information about the chemical and structural environment of the emitter atom of the photoelectron, as it will be discussed more in detail in section 2.3.3. Furthermore, spin-orbit splitting may also lead to a splitting of an element peak by a defined element and orbital specific binding energy shift. Especially for complicated spectra one can utilize the known energy of spin-orbit components in order to correctly assign the core level peaks. A splitting, however, can also indicate a non-equivalent location of the atoms in the crystal structure as seen for Au surface reconstructions³² or for charge density waves (CDW)³³. Another effect which can create additional peaks are the so called shake-up and shake-off satellite peaks. Shake-up components are associated with photoelectrons losing energy usually during the excitation of plasmons before leaving the material and appear as an additional peak in the core level spectra at higher binding energy³⁴. In the case of shake-down satellites a localized initially unoccupied valence state lowers in energy in the present of the core hole which leads to a transfer of a valence electrons into the localized state. This filled state shields more effectively the core hole which results in a higher kinetic energy of the photoelectrons and therefore to a peak component at lower binding energy in the core level spectra³⁴.

In order to perform quantitative chemical and structural analysis with XPS the photoemission spectrum has to be described with the correct theoretical model. In a naïve picture, without any broadening effects, the photoemission of core level electrons should yield a δ -function. However, this does not apply in reality and we have to consider broadening effects as the core hole life-time and vibrational broadening. The finite hole lifetime is connected with the natural linewidth which originates from the photoemission process itself. The creation of the photohole leads to an excited state of the atom from which it can decay non-radiatively (X-ray fluorescence) or radiatively (Auger emission). In consideration of the Heisenberg Uncertainty Principle, $\Delta E_0 \geq \frac{\hbar}{\tau}$, which connects the energy of the core hole ΔE_0 directly with core hole lifetime τ , one can see that a smaller core lifetime (equal to higher decay probability of the excited state) results in a broadening of energy width of the resulting core level peak. This broadening effect can be described by the Lorentzian function:

$$I_L(E_{bin}) = \frac{I_0}{\pi} \frac{\Delta E_0/2}{(E_{bin} - E_{bin}^0)^2 + \Delta E_0^2/4}, \quad (2.10)$$

where I_0 is the maximum intensity for a peak at the binding energy E_{bin}^0 with a full width half maximum (FWHM) of ΔE_0 .

In the case of metals the high density of states present near the Fermi level enables electron-hole pair formation, resulting in partly a reduction of the kinetic energy of the photoelectrons which leads to asymmetric line shapes shifted towards higher binding energy in the core level spectra. To account for this phenomenon the function proposed by Doniach-Šunjić³⁵ can be used:

$$I_{DS}(E_{bin}) = I_0 \frac{\Gamma_E(1 - \alpha_{DS}) \cos \left[\frac{1}{2} \pi \alpha_{DS} + (1 - \alpha_{DS}) \arctan \left(\frac{2(E_{bin} - E_{bin}^0)}{\Delta E_0} \right) \right]}{[(E_{bin} - E_{bin}^0)^2 + (1/2 \Delta E_0)^2]^{1/2(1 - \alpha_{DS})}}, \quad (2.11)$$

where Γ_E is the Euler's Gamma function, α_{DS} the asymmetry factor, E_{bin}^0 the binding energy of the core level peak and ΔE_0 the FWHM of the Lorentzian line as in equation 2.10. It is worth noting that for $\alpha_{DS} = 0$ the Doniach-Šunjić function transforms into the Lorentzian line shape as seen in equation 2.10.

The linewidth of the core level spectra is further dependent on the lattice vibrations, the instrumental resolution and disorder contributions. All these factors can be taken into account by convolving equation 2.11 with a Gaussian.

A further necessary point for analyzing core level spectra is the appropriate choice of the background. The most basic background choice is a linear or polynomial one

and can be used for "standard backgrounds". However, for strong asymmetric backgrounds the so called Shirley background function can compensate³⁶. In this thesis, all presented core level spectra are fit with a Doniach-Šunjić function convoluted with a Gaussian and using an appropriate background.

2.1.4 ARPES Spectra Acquisition and Analysis

To perform ARPES measurements several requirements for the measurement setup and the sample have to be considered. The sample surface should have a low density of step edges, a low defect density and free of adsorbates since all these factors can all lead to additional scattering of the emitted photoelectrons. In the case of the synthesis of high quality SL TMDCs on Au(111), contamination such as oxygen or carbon might lead to defect formation and unwanted side products in the material, which can harm the sample's properties. This can be prevented by removing adsorbates on the Au(111) surface before the growth by standard Ne⁺ sputtering/annealing and monitoring of the ultra-high vacuum (UHV) pressure during the growth process. In the case of layered bulk samples, removing the top surface with the scotch tape or top-post cleaving method in UHV minimizes the contamination by adsorbates. It is also worth noting that the presence of multiple rotational domains potentially complicates the interpretation of the crystals electronic dispersion.

To access the full potential of ARPES a tunable, monochromatic and brilliant light source is needed. Synchrotron radiation fulfills these requirements. To prevent additional scattering of the photoelectron outside the sample, all ARPES measurement are performed in UHV. Band mapping in ARPES requires accurate control of the angle between analyzer and sample, which is demanding in UHV from a technical point.

For simultaneous acquisition of the emission angle and the kinetic energy of the emitted photoelectrons a hemispherical analyzer is used. The analyzer consists of three main parts: the electronic lens system, a hemispherical capacitor and a 2D detector as shown in fig. 2.2. In this thesis all ARPES measurements were performed using a SPECS Phoibos 150 analyzer, which will be used as model system to describe the working principle of ARPES in the following paragraphs.

Photoemitted electrons which enter the lens system are retarded to a chosen energy called the pass energy E_p . The filtering according to the kinetic energy of the electron is executed in the mirror plane, also called the dispersive plane, of the analyzer, as seen in fig. 2.2(a): two negative applied electric fields in between the

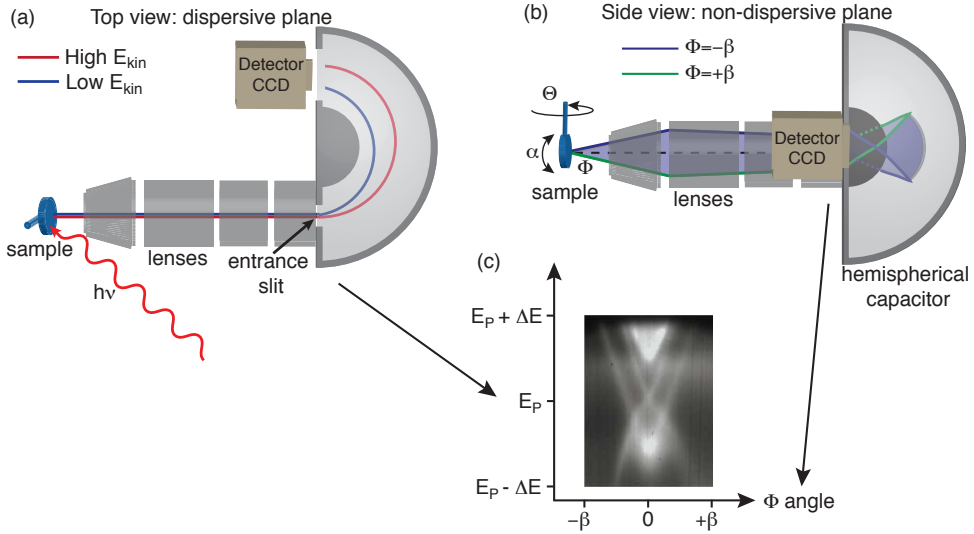


Figure 2.2: Schematic of the geometry of the ARPES experiment and the basic working principle of the hemispherical analyzer. (a) In the dispersive plane the electric field in between the two hemispheres enables the energy discrimination of low (blue) and high kinetic energy (red) photoelectrons. (b) Schematic of the non-dispersive plane of the hemispherical analyzer. The photoelectrons which are emitted within the lens mode acceptance angle of $\Phi = -\beta$ (blue) and $+\beta$ (green) are focused by the lenses and its angular distribution is projected onto the detector and imaged with the CCD camera. (c) Example of an acquired ARPES spectra with the hemispherical detector. The shown spectra is discussed more in detail in section 3.2. By adjusting the tilt angle α and the polar angle Θ one gains access to the defined area of interest of the electronic structure of the material system under investigation. Adapted and modified from Ref.³⁷.

two hemispheres deflect the trajectories of the incoming electrons depending on their kinetic energy working as a bandpass filter with an energy window of $E_p \pm \Delta E$. The measured energy window ΔE can be set by the retarding ratio parameter $r = E_{kin}/E_p$, which enables the investigation of photoelectrons with a desired kinetic energy. The pass energy E_p simultaneously directly influences the resolution of the detector ΔE_A according to:

$$\Delta E_A = \frac{E_p(S_1 + S_2)}{4R}, \quad (2.12)$$

where S_1 and S_2 are the widths of entrance and exit slits, and R is the mean radius of the analyzer ($R = 150$ mm for the SPECS Phoibos 150). As seen in equation 2.12 a small energy resolution is obtained with a low pass energy and thin slits which will also narrow the energy range and lower the electron count rate on the detector.

In the non-dispersive plane the photoelectrons are discriminated according to the emission angle Φ (fig. 2.2(b)). The lens system determines the acceptance angle $\pm\beta$ of the photoelectrons and can be adjusted during the measurement to observe the required angular range on the detector. The discrimination of the photoelectrons is performed in the hemispherical analyzer as sketched in fig. 2.2(b) where at the end of the analyzer the intensity of the incoming electrons is amplified by micro channels plates (MCP) before the photoemission spectra is projected onto a phosphorous screen and imaged by a CCD camera. In this way, the hemispherical analyzer produces photoemission intensity profiles dependent on the kinetic energy E_{kin} versus the acceptance angle Φ at a fixed tilt angle α and polar angle Θ and provides a cut through the Brillouin zone (BZ) of the material's electronic structure as shown in fig. 2.2(c). However, to access the information of the whole BZ, maps of several cuts have to be stacked together by changing the polar angle Θ . For the transition from angular space to momentum space the angles defined in fig. 2.2(b) have to be considered:

$$k_x = \sqrt{\frac{2m_e E_{kin}}{\hbar^2}} [\cos \alpha \sin \Phi - \sin \alpha \cos \Theta \cos \Phi] \quad (2.13)$$

$$k_y = \sqrt{\frac{2m_e E_{kin}}{\hbar^2}} \cos \Phi \sin \Theta. \quad (2.14)$$

To first order approximation, the angular resolution is translated into k-resolution Δk_{\parallel} by:

$$\Delta k_{\parallel} = \sqrt{\frac{2m_e E_{kin}}{\hbar^2}} \cos \Phi \Delta \Phi, \quad (2.15)$$

where $\Delta\Phi$ describes the angular resolution¹ that depends on the chosen lens mode. Equation 2.15 shows that the k-resolution can be improved using smaller photon energies or decreasing the emission angle *i.e.* measuring the dispersion near normal emission.

Notably, the data acquisition in ARPES is accompanied by artifacts for the kinetic energy and for the angular dimension. The former, *i.e.* the spherical aberration, is due to the geometry of the hemispherical analyzer and describes that electrons with the same kinetic energy appear at different kinetic energies on the phosphorous screen as a function of the emission angle. This can be compensated for the use of curved entrance slits. For the latter photoelectrons emitted at the same angle but different energy are detected at different emission angles. This so called chromatic aberration can be corrected after data acquisition with the SPECS software.

To perform quantitative analysis of the ARPES spectra, several broadening effects such as the energy-resolution of the light source, finite energy and momentum resolution have to be considered. Therefore, the intensity of the photoemission process in equation 2.7 has to be convoluted with a Gaussian broadening $G(\Delta\omega, \Delta k_{\parallel})$ and the background \mathcal{I}_0 has to be added to compensate for secondary electron emission:

$$\mathcal{I}(\omega, \mathbf{k}_{\parallel}) = [\mathcal{A}(\omega, \mathbf{k}_{\parallel})M(\omega, \mathbf{k}_{\parallel})f_{FD}(\omega)] \otimes G(\Delta\omega, \Delta k_{\parallel}) + \mathcal{I}_0(\omega), \quad (2.16)$$

where $\Delta\omega$ is the combined energy resolution of the light source and the contribution from the analyzer. Intensity profiles along the energy direction, *i.e.* energy distribution curve (EDC), or cuts along momentum direction, *i.e.* momentum distribution curve (MDC), usually exhibit Lorentzian or Voigt shape profiles on top on a polynomial background.

2.2 Experimental Setup

The ARPES results presented in this thesis were all acquired at the SGM3 endstation at ASTRID2, which is shown in fig. 2.3. Several of the presented techniques were used in collaboration with other institutes. The STM measurements for section 3.2 and partly for chapter 4 were performed in collaboration with the group of Prof. Alexander Khajetoorians (Radboud University) and for section 3.3 and 3.4 with the group of Prof. Roland Wiesendanger (Universität Hamburg). Complementary STM mea-

¹Values of typically 0.1° angular resolution can be reached.

measurements were performed in house with an Aarhus style STM³⁸. The XPD data were conducted at the SuperESCA beamline (Elettra Sincrotrone Trieste). The following discussion is limited on the experimental setup at Aarhus University.

2.2.1 ASTRID2 and SGM3 Beamline

In 2014 ASTRID2, a small high brilliance synchrotron storage ring, was commissioned at Aarhus University in Denmark³⁹. The old synchrotron ASTRID was modified to a booster ring for ASTRID2 (fig. 2.3(a) and (b)). With a diameter of 15 m ASTRID2 can host electrons with an energy of 580 MeV and an electron current up to 200 mA. The electrons are forced by magnetic fields to circulate in the storage ring and every time the electron trajectory bends light is emitted. This principle is exploited for the production of high monochromatic and polarized light in undulators where a series of coupled magnets force the electron in a “zig-zag” trajectory producing polarized light.

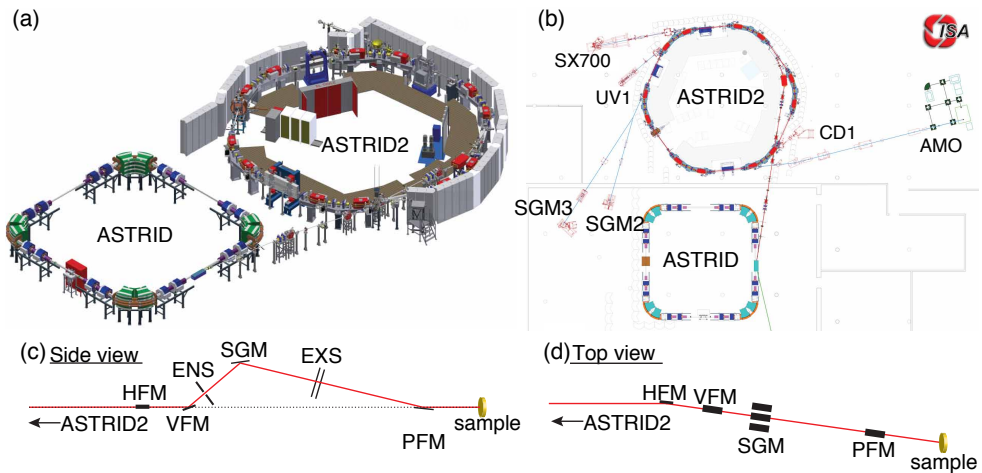


Figure 2.3: (a) Schematic image of ASTRID and ASTRID2. (b) The beamline and endstation overview in the ISA facility. (c) Side- and (d) top views of the SGM3 beamline optics, respectively. Adapted from Ref.⁴⁰.

By changing the distance between the magnets the photon energy can be tuned continuously over a wide range and allows for atomic and molecular physics, photobiology, UV spectroscopy or surface science studies. The photoemission data presented in this thesis were acquired at the Spherical Grating Monochromator 3 (SGM3) beamline. The basic components of the SGM3 beamline are shown in fig. 2.3(c) and (d). The light entering the beamline is first focused on the entrance slit (ENS)

by the horizontal (HFM) and the vertical focusing mirror (VFM). The synchrotron light (10 - 150 eV) is monochromated by the spherical grating monochromator (SGM), transmitted through the exit slit (EXS), and then aligned by the post focusing mirror (PFM) before reaching the sample. The spot size of the beam on the sample in the endstation is around $200 \mu\text{m} \times 50 \mu\text{m}$.

2.2.2 SGM3 Endstation

The SGM3 endstation consists of four independent UHV chambers which are all separated by valves as shown in fig. 2.4. The first chamber is the load-lock (LL), where samples are introduced into the UHV system without exposing the subsequent chambers to higher pressures. The LL (base pressure $\approx 7 \times 10^{-8}$ mbar) is connected to the preparation chamber (PC) which contains a sputter gun and an annealing stage for sample preparation, an Aarhus type STM for surface characterization, gas lines and evaporators for surface modifications and a mass spectrometer. The molecular beam

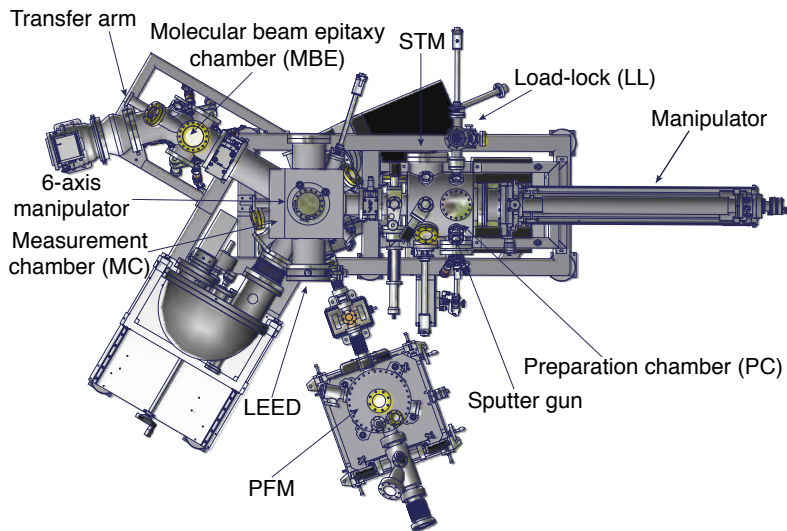


Figure 2.4: Schematic of the endstation of the SGM3 beamline. The SGM3 endstation consists of four separated chambers (LL, PC, MC and MBE chamber) connected by valves. The samples are inserted into the UHV system via the LL chamber. STM measurements and surface treatment are carried out in the PC. In the MC the ARPES and LEED measurements are performed on the 6-axis manipulator. The growth of the 2D materials is done in the MBE chamber. The post focusing mirror chamber (PFM) connects the SGM3 endstation with ASTRID2.

epitaxy (MBE) chamber (base pressure $\approx 10^{-10}$ mbar) contains several metal electron beam evaporators and filaments including iron (Fe) and Vanadium (V) for metal deposition, a custom-built H₂S doser and a heating stage and is therefore suitable for the synthesis of thin film ICs and SL V_{1+x}S₂. The grown samples can be directly measured in the main chamber (MC) by LEED or ARPES on a five axis manipulator. With the closed-cycle He cryostat the sample stage reaches a temperature of around 90 K. Recently, the MC manipulator was replaced with a 6-axis manipulator which can obtain a temperature of 35 K with a more powerful He cryostat². In all chambers the temperature of the sample during annealing or cooling is monitored by a K-type thermocouple attached to the back of the sample.

In addition, a home build UHV suitcase can be attached to the MBE chamber which enables the transfer of samples between separate UHV analytical systems without breaking vacuum. The suitcase is further equipped with a battery powered ion-pump and is compatible with both Aarhus style and Omicron style sample holders which enables to ship samples to measurements setups in whole Europe.

2.2.3 STM-Chamber

A part of the author's PhD was dedicated to the design and construction of a stand alone STM chamber in collaboration with the post-doc Marco Bianchi. Fig. 2.5(a) shows the independent chamber which is used for the synthesis of SL TMDCs on different metal substrates (e.g. Au(111), Ag(111), Pt(111)) and characterizing the grown samples with the STM to monitor and modify the growth procedures of the SL TMDCs. The STM-chamber consists of two chambers separated by a valve. The first chamber is the LL which allows to introduce samples into the UHV chamber without breaking vacuum in the MC. The MC, which is shown in fig. 2.5(b), has a base pressure of around 8×10^{-10} mbar and is used for sample preparation, sample growth and characterization. For preparation or cleaning purpose the sample can be heated up to 800°C using a hot filament and cooled down with liquid nitrogen in the sample stage of the manipulator. The temperature is measured directly at the back of the sample and at the manipulator with a K-type thermocouple. Cleaning of the sample can be achieved by sputtering with Ne⁺ ions. Furthermore, the MC is equipped with a double electron beam evaporator and a leak valve for backfilling the MC with dimethyl disulfide (DMDS) (not visible in fig. 2.5(b)) which is a possible S

²Data presented in chapter 3 were acquired with the 5-axis manipulator and in chapter 4 with the 6 axis manipulator.

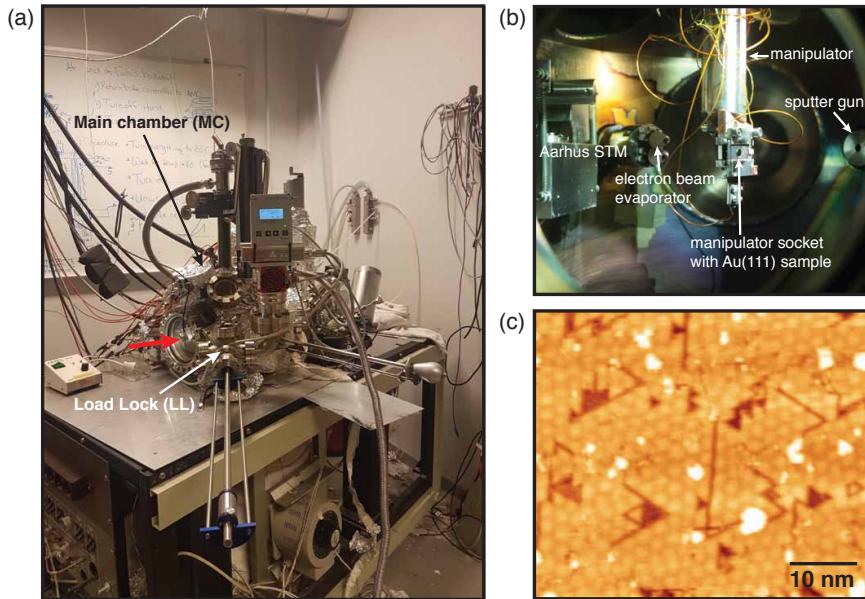


Figure 2.5: (a) Image of the STM-chamber. The red arrow marks the view port through which the photo, shown in panel (b), was taken. (b) Image of the MC with the manipulator, the manipulator socket with an Au(111) crystal, Aarhus STM, electron beam evaporator and sputter gun. (c) STM image of one of the first synthesized SL $V_{1+x}S_2$ on Au(111) in the STM chamber. Tunneling parameters: $V_s = 825$ mV, $I_t = 0.3$ nA.

source for growing high quality SL TMDCs⁴¹. The as-grown samples can be directly characterized by the STM or if necessary capped with DMDS molecules and transferred to the SGM3 endstation for further photoemission experiments. In order to reduce the overall mechanical noise during STM measurements, the STM chamber is equipped with pneumatic damping legs and can be solely pumped by an ion pump instead of also being pumped by the turbomolecular pump which can induce noise of (in this case) 1500 Hz. Fig. 2.5(c) shows a STM image of one of the first synthesized SL $V_{1+x}S_2$ on Au(111) samples in the STM-chamber which is discussed further in chapter 4.

2.3 Techniques for Structural Analysis

Structural analysis techniques reveal directly information about the material's crystal structure and quality. For a complete understanding of the morphology of the material

complementary techniques have to be exploited. In the following section STM, LEED and XPD are introduced.

2.3.1 Scanning Tunneling Microscopy

The working principle of STM is the quantum mechanical tunneling of electrons between an atomically sharp tip and a conductive sample, which are few Ångström apart (fig. 2.6(a))⁴². By applying a bias voltage V_s a distance depended tunnel current I_t can be measured through the tip-sample potential gap:

$$I_t \propto V_s e \left(-\frac{\sqrt{8m_e \Phi_w}}{\hbar} d \right), \quad (2.17)$$

where d is the sample-tip distance and Φ_w the average work function. The equation above shows that the tunnel current changes by an order of magnitude if the sample-distance varies around 1 Å allowing one to monitor the surface structure with atomic resolution. Imaging the surface with atomic resolution requires a very precise movement of the tip by so called piezoelectric motors. To achieve a real space image of the surface, the STM tip scans in two STM operating modes, constant height or constant current mode. For constant current mode the whole surface is scanned line by line, while the proportional-integral-derivative (PID) feedback loop adjusts the height of the tip above the sample surface to maintain a constant tunnel current I_t , whereas in constant height mode the tunnel current is adjusted to maintain a constant height above the sample surface during the scan. In fact, STM is imaging the local density of states (LDOS) of the sample convoluted with the LDOS of the tip, however, in some cases this can be interpreted as surface topography. Therefore, STM is an excellent technique to investigate locally physical effects on the sample's surface in real space. An example of an atomically resolved image of highly ordered pyrolytic graphite (HOPG) is shown in (fig. 2.6(b)).

An additional STM technique is the scanning tunneling spectroscopy (STS) which provides local information about the density of states in the sample as a function of the binding energy. Here, the STM tip is held at constant distance at a fixed position over the sample and the applied bias voltage is swept through a specified range. By measuring the tip-sample current as a function of the bias voltage, an I-V-curve is obtained whose derivative is proportional to the LDOS. This technique requires an extremely stable system during the measurement and a precise calibration of the STM.

In parts of this work the Aarhus type STM was used for imaging the surface of

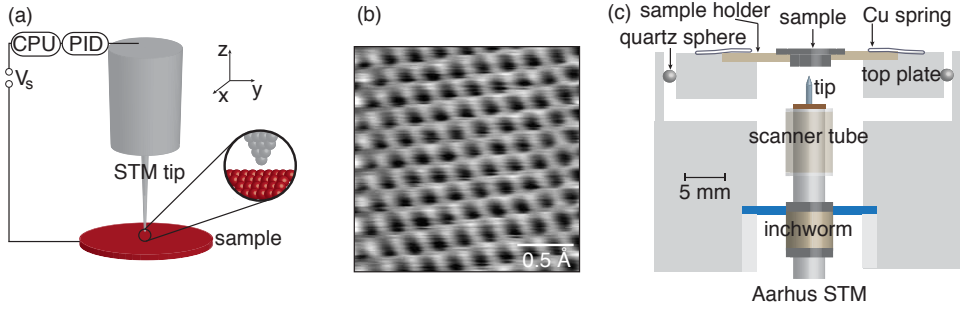


Figure 2.6: (a) Basic setup of a STM. (b) Atomic resolution STM image of HOPG acquired at room temperature with the Aarhus type STM. Tunneling parameters: $V_s = 0.98$ nA, $I_t = 76$ mV. (c) The schematic design of the Aarhus STM. Inspired by Ref.⁴³.

the sample. The compact design of the so called “thimble-size” STM enables it to be directly attached to a chamber by a flange (fig. 2.6(c))³⁸. The approach of the tip is realized by an inchworm motor which consists of two clamping piezos placed at the upper and lower limit and one expanding piezo in the center moving along a quartz tube. By applying the right sequence of voltages on the three piezos the tip will move in an inchworm-like manner towards the sample. Precise movement during scanning is ensured by the scanner tube. The sample holder is thermally and electrically insulated by three quartz spheres reducing electrical noise and thermal drift during STM measurements. To reduce mechanical noise the sample is fixed in the sample holder by two tight Cu springs and the whole STM is suspended by springs. It is worth noting that the STM used in this thesis, was situated near (and at) ASTRID2 where electrical and mechanical noise were expected. Surprisingly, the electrical isolation and mechanical damping implemented in the existing Aarhus style STM proved to be sufficient, and atomically resolved images of the sample surface could be achieved.

2.3.2 Low Energy Electron Diffraction

With LEED the global structural properties of a sample can be investigated which makes it ideal as a complementary technique to STM. The principle of LEED is based on the electron diffraction phenomenon, where a collimated electron beam is elastically scattered on the surface and the resulting diffraction pattern can be observed on a fluorescent screen³⁷. The IMFP for low energy electrons (10-300 eV)

used in LEED is rather short and therefore the electrons probe effectively only the surface of the material. Therefore, LEED patterns are an efficient option to extract global information about the surface structure, the quality and the composition of a material.

The basic setup of a typical LEED apparatus is shown in fig. 2.7(a) consisting of an electron gun producing low-energy monochromatic electrons, several retarding grids used for focusing the elastic scattered electrons and filtering the inelastically scattered electrons, and lastly a fluorescent screen. For electrons hitting the sample surface at normal incidence, the Laue condition is as following:

$$\Delta \mathbf{k}_{\parallel} = \mathbf{k}_{\parallel,f} - \mathbf{k}_{\parallel,i} = \mathbf{k}_{\parallel,f} = h\mathbf{b}_1 + k\mathbf{b}_2, \quad (2.18)$$

where $\mathbf{k}_{\parallel,i}$ ($\mathbf{k}_{\parallel,f}$) is the momentum parallel to the sample surfaces of the incoming (scattered) electrons, h and k are integers and \mathbf{b}_i (where $i=1$ and 2) are the reciprocal lattice vectors of the material. With equation 2.18 and taking the geometry of the LEED setup into account as seen in fig. 2.7(a) the distance d_{hk} from the center of the fluorescence screen to a diffraction spot can be determined:

$$d_{hk} = R \sin(\Theta_{hk}) = R \frac{|\Delta \mathbf{k}_{\parallel}|}{|\mathbf{k}_f|} = R \sqrt{\frac{\hbar^2}{2m_e E_{kin}}} |h\mathbf{b}_1 + k\mathbf{b}_2|, \quad (2.19)$$

where R is the radius of the screen, E_{kin} is the kinetic energy of the scattered electrons and \mathbf{k}_f the momentum of the scattered electrons. The diffraction points can be observed directly by eye or camera on the fluorescent screen and assigned to the reciprocal lattice vectors \mathbf{b}_i with equation 2.19, as seen in fig. 2.7(b) for the example of Au(111). Defects and/or disordered adsorbates increase diffuse electron scattering and lead to broadening of the diffraction points thereby indicating the cleanliness and quality of the sample. In the case of bare Au(111) the surface purity can be judged by the formation of the so called herringbone reconstruction which leads to additional satellite spots in LEED as seen in fig. 2.7(b), contamination on the surface can lift the reconstruction and cause the satellite spots in the LEED pattern to disappear⁴⁴.

Furthermore, the orientation of the adlayer with respect to the substrate can rather easily be determined by LEED as the corresponding diffraction pattern holds information about the substrate crystal lattice and the adlayer. Information about the thin film adlayer on a substrate can be obtained by considering the observed moiré pattern. Note that the existence of multiple rotational domains on the surface lead to the formation of corresponding rotated reciprocal lattice vectors in the diffraction pattern and the interpretation of the LEED image may be rather difficult.

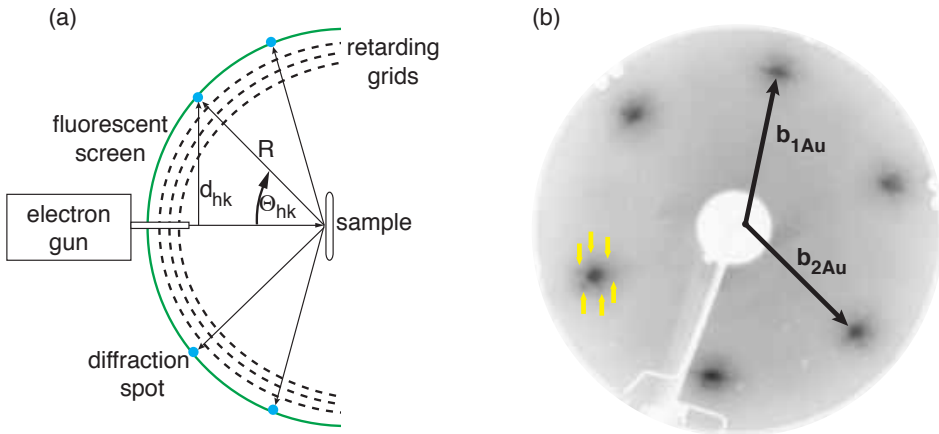


Figure 2.7: (a) Schematic of the LEED experiment and its working principle. The dashed black lines represent the retarding grids, the green line the fluorescent screen and the blue dots the diffraction spots. (b) Example of a LEED pattern of a clean Au(111) surface. The hexagonal reciprocal lattice vectors \mathbf{b}_{1Au} and \mathbf{b}_{2Au} are indicated with black arrows. Moiré satellites are visible around each Au(111) diffraction spot and indicated for one Au(111) main spot with yellow arrows.

The fast access to the surface crystal structure of a material makes LEED a precious starting point for understanding the crystal morphology of a sample.

2.3.3 X-Ray Photoelectron Diffraction

A technique which is particularly suitable for the structural analysis of 2D systems is XPD. This technique is based on the photoelectric effect but instead of imaging the electronic structure, as in ARPES, one obtains structural information about the material system⁴⁵. XPD exploits the fact that the core level photoelectrons are scattered elastically and inelastically during the transport from the emitters (emit the photoelectrons) to the vacuum. Fig. 2.8 shows schematically the photoelectron diffraction process: in photoelectron diffraction experiments the emitter atom (grey ball) emits a core level photoelectron excited by monochromatic X-rays. The generated primary electron wave Φ_0 can be directly detected or inelastic scattering events can occur with the surrounding environment (blue and green balls) which generate the electron waves Φ_j , Φ_k and Φ_f , $\Phi_{f,g}$. The interference of the primary electron wave Φ_0 and the scattered electron waves creates a unique diffraction pattern, *i.e.* XPD pattern,

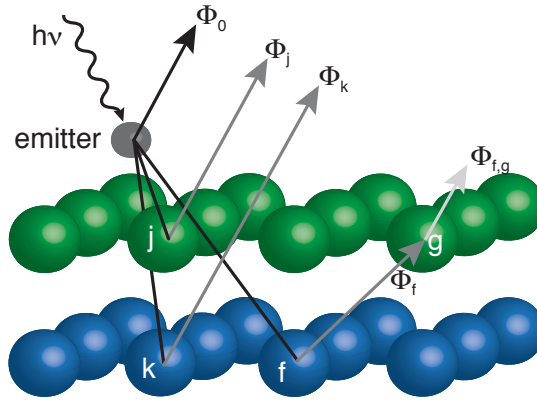


Figure 2.8: Schematic of the processes involved in the photoelectron diffraction process. The emitter (grey ball) generates the primary electron wave Φ_0 by photoemission. The scattering of the primary wave on the atoms j, k and f (green and blue balls) produce the secondary waves Φ_j, Φ_k and Φ_f . $\Phi_{f,g}$ is a double scattered wave on the scatterers f and g .

for emitters in the same chemical environment. The elastic scattering leads solely to an overall decrease in the intensity of the core levels and its contribution to structural information is merely marginal. In contrast the inelastic scattering processes can enhance or reduce the core level intensity depending on the geometry around the emitter, the detection angle and the kinetic energy of the photoelectron.

One can distinguish in XPD between two scattering events: forwards and backwards. In the case of forward scattering events the scatterer is placed in between the emitter and the detector and the resulting diffraction pattern holds information about the emitter position and the location of the atoms in front of the emitter. Forward scattering is dominated by electrons with a kinetic energy greater than 150 eV. On the contrary, structural information under the emitter are received by backscattering events. Here, the scatterer is placed behind the emitter and it is prevalent for photoelectrons with a kinetic energy less than 150 eV. In order to obtain detailed quantitative information about the crystal structure, core level spectra as a function of polar (Θ) and azimuthal (ϑ) angles have to be acquired and compared with multiple scattering calculations. The intensity modulation in the XPD pattern provides important structural information about the local geometry around the emitter atoms. The modulation function of the diffraction pattern is defined as:

$$\chi = \frac{I - I_0}{I_0}, \quad (2.20)$$

where I is the measured intensity of the core level and I_0 is a smooth spline fitted to the intensity distributions along the azimuthal angle⁴⁵. This method filters out the photoelectron modulations from smooth variations in intensity due to e.g. experimental artifacts.

In this thesis, the XPD simulations are performed by the Electron Diffraction in Atomic Cluster (EDAC) package⁴⁶. In order to simulate the diffraction pattern with the EDAC package an atom cluster has to be designed on which multiple scattering theory is performed to model the XPD pattern. The simulated XPD pattern for two allotropes of VS_2 , 1H and 1T (described in detail in chapter 4), for the bottom S $2p_{3/2}$ core level and the corresponding designed crystal lattice models for the simulation are shown in fig. 2.9. The difference in the simulated stereographic projection in fig. 2.9(a) and (b) shows that it is possible to distinguish instantly between the 1H and 1T configuration of VS_2 , which is rather difficult with STM or LEED. Therefore, XPD is an excellent tool to receive information of the position of ordered adsorbates on a material or access the atomic lattice of layered structures as TMDCs.

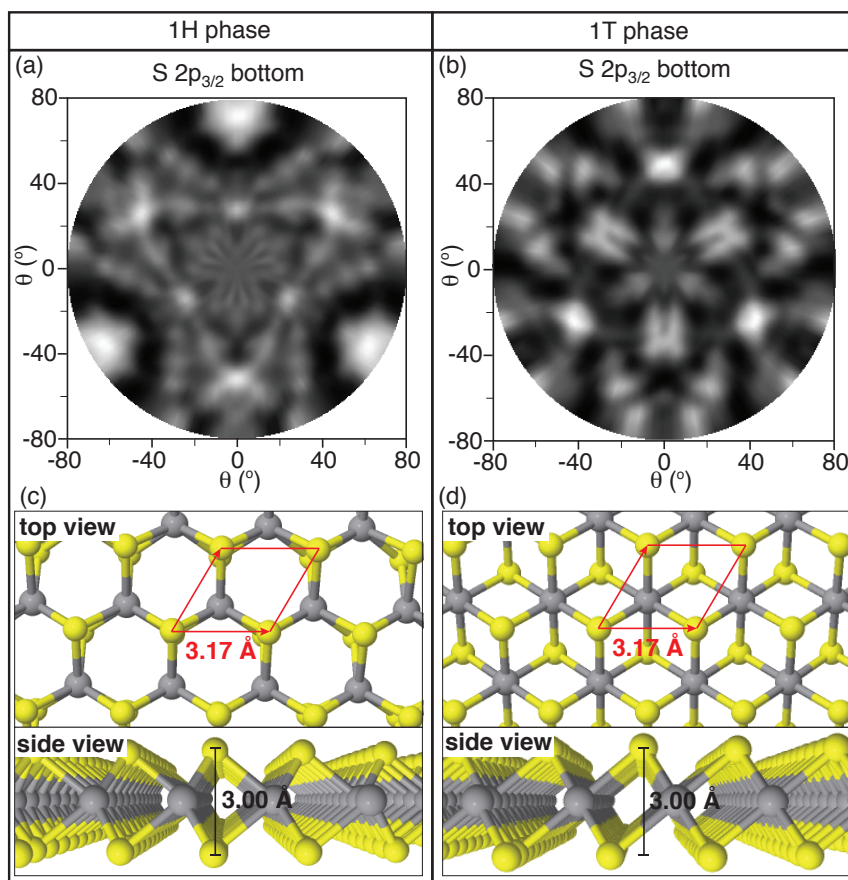


Figure 2.9: Simulated stereographic projections of the modulation function for the bottom S $2p_{3/2}$ core level of (a) the 1H and (b) 1T configuration of VS_2 , respectively. Simulations are performed at a kinetic energy of 239 eV of the photoelectrons. Bright represents high intensity, dark low intensity. Ball and stick models for the (c) 1H and (d) 1T configuration for the corresponding crystal lattice model used for the simulations of the XPD pattern. Yellow balls mark the S atoms and grey balls mark the V atoms. The unit cell is marked with red arrows. The lattice constants used for the XPD simulation are indicated in the panels.

Chapter 3. Iron Chalcogenides

This chapter focuses on the methods employed for the synthesis and characterization of FeSe and FeTe thin films on the topological insulators Bi_2Se_3 and Bi_2Te_3 , respectively. The crystal structure and morphology of the thin films is discussed based on STM and LEED measurements. The electronic structure of the thin films and the underlying substrate is investigated. In the following the historical background on the research field of superconductivity is presented before the crystal and predicted electronic structure of the substrate and the adlayer is discussed.

3.1 Introduction

3.1.1 2D Iron Chalcogenides

Over a century ago superconductivity on pure mercury (Hg) was discovered by Kamerlingh Onnes and was later theoretical explained by Bardeen, Cooper and Schrieffer (BCS) in 1957^{47,48}. In the BCS theory the resistance-free flow of electrical charges is described by the formation of electron pairs, so called Cooper pairs, through an attractive interaction that is mediated by phonons. The BCS theory predicts an upper limit of the critical temperature (T_C) of 30 K for electron pairing caused by lattice vibrations. In 1986, however, a T_C of 35 K was realized in a barium-lanthan-cuprate by Bednorz and Müller and led to a new class of superconductors, the unconventional superconductors⁴⁹. Underlining the importance of this work, the Noble prize in physics was awarded to Bednorz and Müller in 1987. In these materials pairing does not solely occur from the conventional electron-phonon coupling, instead it is a consequence of an unconventional pairing mechanism. The key ingredients for high temperature superconductivity, however, are not clearly identified yet and it is rather an unsettled question if phonons⁵⁰, magnetic fluctuations⁵¹, two-dimensional effects^{52,53} or charge doping^{54,55} are responsible for the unconventional behavior. Among the discovered

unconventional superconductors in recent years, SL FeSe grown on SrTiO₃, a system which is also superconducting in the bulk^{56,57}, has attracted considerable attention due to a T_C well above the BCS limit combined with a simple crystal structure. Therefore, FeSe is used as a model system to understand the underlying processes in high-temperature interfacial superconductivity^{22,23,58,59}. While several studies reveal that the superconductivity properties in this system can be modified by tailoring the film thickness, the doping or the substrate of the FeSe thin film, little work has been performed on FeTe thin films, a cousin compound of FeSe. As these ICs share a similar lattice structure and consist of a related atomic composition similar electrical properties might be expected in a naïve picture. However, FeTe thin films grown on the topological insulator Bi₂Te₃⁶⁰ exhibits superconductivity solely below 6 K⁶¹, in contrast to the non-superconducting bulk phase.

The crystal and electronic structure of FeSe thin films and FeTe thin films synthesized on the related topological insulators Bi₂Se₃ and Bi₂Te₃, respectively, are investigated in this work, in order to understand better the source of the different electronic properties.

3.1.2 Crystal and Electronic Structure of Bi₂Se₃ and Bi₂Te₃

Bi₂Se₃ and Bi₂Te₃ exhibit the same structure: a rhombohedral lattice with the space group $R\bar{3}m$ (fig. 3.1(a))⁶². Out of simplicity the nomenclature is therefore generalized to Bi₂X₃. Bi₂X₃ consists of stacked quintuple layers ordered in a [X-Bi-X-Bi-X] sequence along the [111] direction and separated by a van der Waals gap. The weak van der Waals bonding enables the exposure of a clean (111) surface simply by cleaving with the scotch tape method, exposing only the chalcogenides X on the top. The simple and fast access to a clean surface and the tendency of Bi₂X₃ to release X upon annealing (necessary for the formation of the FeX thin films), has qualified Bi₂X₃ as substrate of choice for the synthesis of FeSe and FeTe thin films.

It is worth mentioning that Bi₂Se₃ and Bi₂Te₃ belong in the class of topological insulators which attracted considerable attention in the physics community due to the unusual electronic properties: the bulk is isolating while the surface exhibits localized two-dimensional conducting channels, which hold intriguing properties such as characteristic spin texture⁶⁵. It is important to point out that the formation of these two-dimensional states is not a consequence of the details of the surface, *i.e.* the general structure or reconstruction effects, but instead given by the topology of the

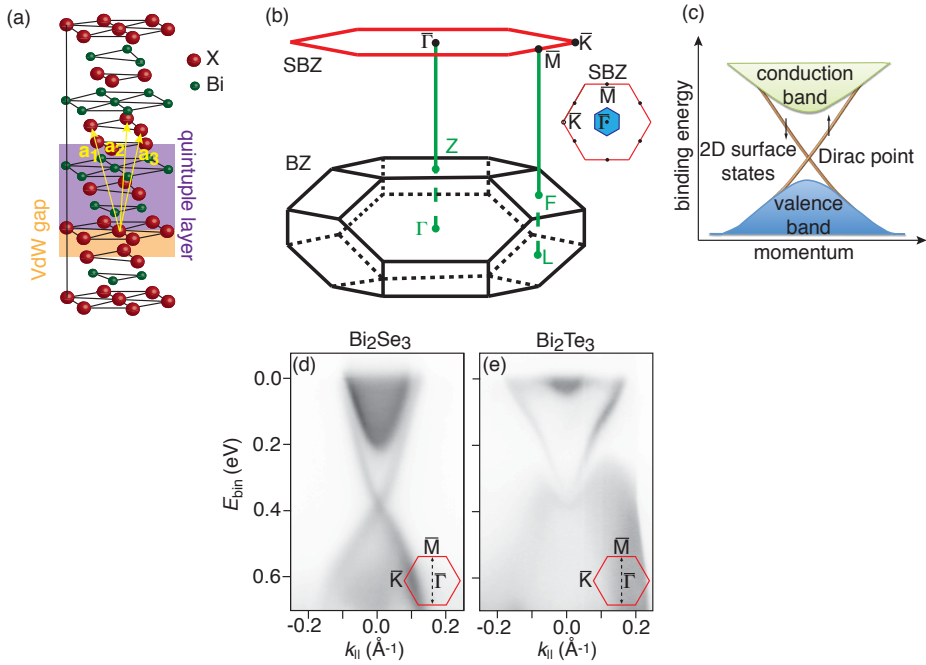


Figure 3.1: (a) Crystal structure of the quintuple layered stacked Bi₂X₃. The vectors \mathbf{a}_1 , \mathbf{a}_2 , \mathbf{a}_3 indicate the lattice vectors of the primitive cell. (b) Bulk (black) and projected SBZ (red) of Bi₂X₃ labeled with high symmetry points. The inset shows the projected SBZ with characteristic hexagonal warped topological surface state in blue (adapted and modified from Ref.⁶³). (c) Schematic band structure of a topological insulator with the topological surface state and the Dirac point in the band gap. The topological surface state is indicated with orange lines and the spin-splitting with up-pointing and down-pointing arrows. Bottom row: low energy band structure of (d) Bi₂Se₃ and (e) Bi₂Te₃ acquired with ARPES (adapted from Ref.⁶⁴). The inset shows the cut along the direction through the BZ for the presented band structures.

bulk band structure. Therefore, it is interesting to inspect the characteristic electronic features of the topological insulators Bi_2Se_3 and Bi_2Te_3 more in detail.

The bulk BZ and projected surface Brillouin zone (SBZ) of Bi_2X_3 are shown in fig. 3.1(b). In the hexagonally shaped SBZ the high symmetry points are marked with \bar{M} (SBZ edges), \bar{K} (SBZ corners) and around the SBZ center at $\bar{\Gamma}$ the characteristic hexagonal warped topological surface state is visible (inset: blue hexagon)^{66,67}. Fig. 3.1(c) shows the schematic band structure dispersion through $\bar{\Gamma}$ with the valence band (VB), the conduction band (CB) and the characteristic topological surface state (orange lines) with the spin-split bands crossing the energy gap. Low energy photoemission spectra along $\bar{\Gamma}$ - \bar{M} direction for Bi_2Se_3 and Bi_2Te_3 are shown in fig. 3.1(d) and (e), respectively. For Bi_2Se_3 the conduction band minimum (CBM) is located at $\bar{\Gamma}$, creating a direct gap with the Dirac point positioned right above the valence band maximum (VBM)⁶⁸. In the case of Bi_2Te_3 the VB exhibits a M-like shape and the topological surface state partly falls in the VB. For both Bi_2Se_3 and Bi_2Te_3 an intrinsic n-doping is observed that is usually caused by chalcogenide vacancies giving access to CB of the materials¹.

3.1.3 Crystal and Electronic Structure of FeSe and FeTe

Bulk FeSe and FeTe crystallize in a layered PbO-crystal structure with the space group $P4/nmm$ of which two stacked layers are shown in (fig. 3.2(a)). Each layer consists of a [X-Fe-X] sequence which are bonded by weak van der Waals forces suggesting a minor dispersion perpendicular to the surface plane. These kinds of materials are commonly referred as quasi two-dimensional materials. Note that for the 2D-case, two different definitions for the unit cell are established in the case of FeX as seen in fig. 3.2(b): The crystallographically correct unit cell (purple dashed lines) consists of two Fe and two Te atoms, one above and one below the Fe plane and is used generally for ARPES and STM measurements. The corresponding BZ is usually called “folded” or “2-Fe” BZ. The smaller unit cell (green dashed lines) is utilized for experiments sensitive to the Fe positions, such as neutron scattering, and contains only one Fe atom and is the same unit cell that would be obtained by ignoring the X atoms altogether. This BZ is mainly referred as “unfolded” or “1-Fe” BZ. The corresponding BZ for bulk FeX and both 2D BZs are shown in fig. 3.2(c) and (d), respectively.

Note that is rather challenging to obtain stoichiometric FeX and usually excess Fe

¹For undoped Bi_2X_3 the Dirac point is located near the Fermi level.

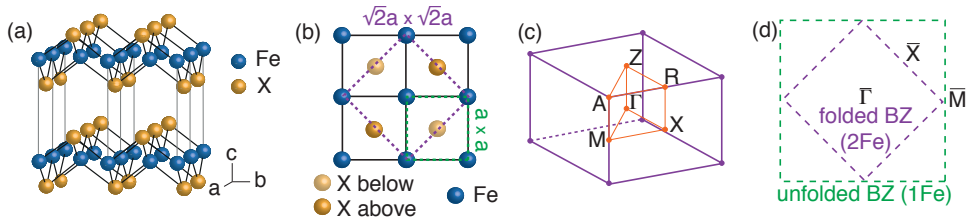


Figure 3.2: (a) Side view of two stacks of the PbO-crystal structure of FeX. (b) Top view of a SL of FeX, indicating X below and above the Fe plane. Dashed purple and dashed green lines represent the folded (2-Fe) and unfolded (1-Fe) unit cells, respectively. (c) Bulk BZ of FeX labeled with the high symmetry points. (d) Folded (dashed purple) and unfolded (dashed green) BZ for a SL of FeX.

forms in between the van der Waals gaps which alters the properties of the material. In the case of bulk Fe_{1+y}Se a small quantity of around $y = 0.03$ excess Fe results already in a suppression of superconductivity^{69–71} and for bulk Fe_{1+y}Te excess Fe influences the magnetic order in the system^{72–74}. However, even if the basic structure of FeSe and FeTe are very similar, in terms of electronic properties and correlated electronic character essential differences are observed in these materials.

In contrast to FeSe, FeTe performs a magneto-structural phase transition at a Néel temperature of $T_N = 60\text{--}70\text{ K}^2$, separating the paramagnetic tetragonal ($>T_N$) and the antiferromagnetic monoclinic ($<T_N$) phase^{72–74}. Due to similar lattice constants of the two phases, however, no difference on a local scale can be observed in terms of purely structural atomic resolution STM images acquired with a non-magnetic tip.

A closer look at the predicted FeTe and FeSe bulk Fermi surface in fig. 3.3(a) and (d), respectively, reveals that a non-negligible dispersion in the crystal momentum perpendicular to the surface (k_\perp) is observable. Thus the view as a quasi 2D system is not valid in terms of the electronic properties and the fully 3D band structure is taken into account. Therefore, instead of labelling center, edge and corner with high symmetry points Γ , X and M , these points are marked according to the projected SBZ $\bar{\Gamma}$, \bar{X} and \bar{M} corresponding to the bulk Γ - Z , X - R and M - A directions (fig. 3.2(c)).

While the comparison of fig. 3.3(a)-(b) and (d)-(e) reveals that the hexagonal warped Fermi contours at the corners of the BZ consist of electron pockets, the large quasi 2D tubes around $\bar{\Gamma}$ originate from hole pockets. In the case of FeTe the non-

²Depends on the amount of excess Fe in bulk Fe_{1+y}Te .

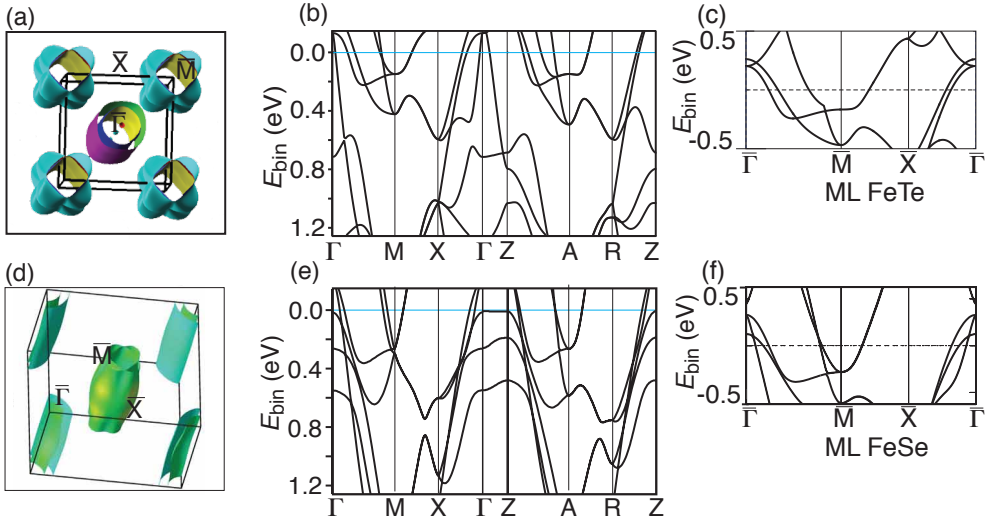


Figure 3.3: Overview of the predicted electronic structures of bulk and monolayer FeTe and FeSe. (a) Predicted Fermi surface of bulk FeTe and (b) corresponding band structure along high symmetry directions. The light blue line indicates the Fermi level obtained by DFT-calculations. (c) Predicted band structure of ML FeTe. The dashed black line indicates the Fermi level obtained by DFT-calculations. FeTe DFT-calculations performed by the group of Prof. Tim Wehling. (d) Predicted Fermi surface of bulk FeSe and (e) corresponding band structure along high symmetry directions. The light blue line indicates the Fermi level obtained by DFT-calculations. Adapted from Ref.⁷⁵ and modified. (f) Predicted band structure of ML FeSe. The dashed black line indicates the Fermi level obtained by DFT-calculations. Adapted from Ref.⁷⁶ and modified.

negligible k_{\perp} dispersion is most clearly observable for the innermost hole pocket, while for FeSe the lack of the small hole pocket at $\bar{\Gamma}$ suggests a smaller interlayer coupling compared to FeTe.

For the monolayer (ML) case in FeTe shown in fig. 3.3(c), the clearest change in the electronic structure is the suppression of the innermost hole pockets, expected from the d_{xz}/d_{yz} orbital character of this band⁷⁷. This characteristic feature for the bulk parent compound might be suitable to provide important information about the dimensionality of the synthesized FeTe thin films in ARPES experiments. In the case of freestanding ML FeSe (fig. 3.3(f)), however, no major changes between the bulk and SL in the electronic structure along the high symmetry direction are observable. Note that it was previously experimentally observed by Ref.²³ that the Fermi surface contour of superconducting ML FeSe changes from a large electron pocket centered

at \bar{M} to two small electron pockets located next to \bar{M} and a hole pockets at $\bar{\Gamma}$ for the non-superconductive multi-film³ phase.

It is worth mentioning that DFT cannot account for the influence of strong electronic correlated effects on the band structure calculations^{78,79}. One consequence is the so called renormalization factor which allows, in the case of ICs, to compress the calculated band structure in binding energy in order to achieve a better agreement with the experimental photoemission data. Moreover, the predicted band structure and Fermi surface features of FeTe and FeSe is rather strongly dependent on the lattice parameters of FeTe and FeSe^{75,80–82}. Therefore, in this work, the DFT-predicted band structures are used as qualitative support for the experimental photoemission data.

³Multi-film means more than one SL of FeSe.

3.2 FeSe Thin Films on Bi₂Se₃

This section is dedicated to the epitaxial growth of FeSe thin films on Bi₂Se₃ and the characterization of the thin films. Firstly, the growth mechanism is briefly outlined. The crystal structure and morphology of FeSe thin films are characterized with STM and LEED and further investigated for superconductivity with STS. The STM data presented in the following chapter were acquired by the group of Prof. Alexander Khajetoorians (Radboud University). Finally, the electronic structure of FeSe thin films on Bi₂Se₃ is discussed.

3.2.1 Growth of FeSe Thin Films on Bi₂Se₃

The basic growth procedure for obtaining FeSe thin films on Bi₂Se₃ was adapted from Ref.⁸³. High quality Bi₂Se₃ crystals, which were synthesized as described in Ref.^{84,85}, were pre-cleaved several times in air until a smooth surface was obtained. In addition, the crystal was cleaved by the scotch tape method in vacuo to expose a clean and adsorbate free surface. Subsequently, the cleaved sample was transferred in situ to check the quality of the sample's surface with LEED, STM and ARPES. On clean high quality Bi₂Se₃ a distinct hexagonal crystal lattice in STM (fig. 3.5(a)), a hexagonal diffraction pattern in LEED (fig. 3.5(c)) and in ARPES the characteristic Dirac cone of the topological surface state (fig. 3.1(d)) are observable. In the next step, the Bi₂Se₃ sample was transferred in situ into a dedicated growth chamber for the synthesis of FeSe thin films. Firstly, iron was deposited on the Bi₂Se₃ surface for two minutes with an electron beam evaporator at room temperature. During the iron deposition the chamber pressure was kept at approx. 1.5×10^{-9} mbar. Se segregates to the surface during annealing of the sample to 570 K for 45 minutes, and reacts with the deposited Fe, forming the FeSe overlayer⁸³. To prevent contamination of the sample the chamber pressure was kept below 2.0×10^{-8} mbar during the annealing process.

3.2.2 Structural Analysis of FeSe Thin Films on Bi₂Se₃

A typical topographic image of the as grown sample exhibits coexisting phases of the Bi₂Se₃ substrate and the FeSe thin films as shown in fig. 3.4(a). The signature of the thin film is the striped moiré which originates from the lattice mismatch between the hexagonal Bi₂Se₃ surface unit cell and the square FeSe surface unit cell. The linear moiré structure exhibits a periodicity of 6.7(0.7) nm and exhibits three rotational

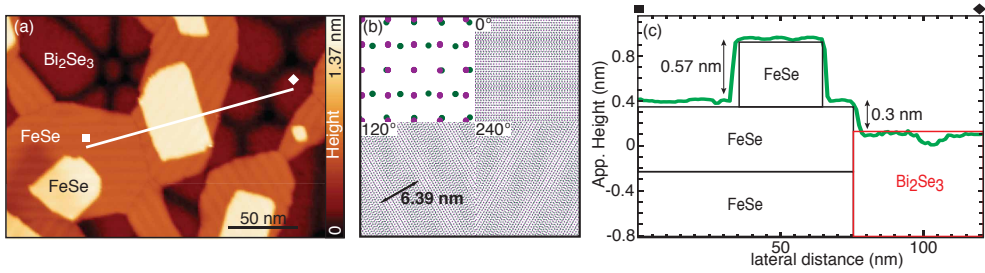


Figure 3.4: (a) Topographic STM image of FeSe thin films on Bi₂Se₃ with a coverage of around 65%. Tunneling parameters: $V_s = 500$ mV, $I_t = 50$ pA. The moiré superstructure and the dislocation network are clearly observable. The white line represents the direction of apparent height profile shown in (c). STM data measured with an Omicron LT-STM at 5 K. (b) Schematic ball model of the moiré superstructure. Bi₂Se₃ hexagonal surface lattice (green balls) and FeSe square lattice (purple balls) form the observed moiré superstructure in rotations of 0, 120° and 240° with respect to each other. (c) Measured apparent height profile (green line) extracted from STM data and superimposed with a layer model (red square Bi₂Se₃, black square FeSe).

domains rotated by 0, 120° and 240°. The experimentally observed moiré pattern can be modeled by a simple ball model superimposing the FeSe square surface lattice (purple balls) on the hexagonal substrate surface lattice (green balls) as shown in fig. 3.4(b). The theoretical moiré pattern exhibits a periodicity of 6.39 nm and the three rotational moiré patterns are obtained by rotating the sub-lattices to 0, 120° and 240° with respect to each other. The Bi₂Se₃ areas are characterized by quasi-hexagonal regions (diameter 20-40 nm) separated by darker regions indicating a lower apparent height. Similar structures were already observed on the same system⁸³ and further in a study of binary alloys originating from a buried dislocation network⁸⁶. The formation of the quasi-hexagonal region is associated with the penetration of a dislocation network into the Bi₂Se₃, caused by the segregation of S during the FeSe layer formations.

The apparent height profile in fig. 3.4(c) reveals that the terrace height difference between two FeSe layers is 0.57(0.02) nm, comparable to the bulk FeSe value of 0.5518 nm^{56,87} and in very good agreement with previously studies of FeSe thin films on Bi₂Se₃ with an apparent height of 0.573 nm⁸³. There is an additional, smaller observed height difference between two FeSe islands: it is around 0.3 nm and does not vary significantly with the applied bias voltage. The apparent height profile, interpreted in terms of the depicted layer model, reveals that the FeSe layers are mainly

embedded in the Bi_2Se_3 surface; and furthermore that the formation of at least double or triple layer FeSe is indicated rather than ML FeSe. Even though the exact number of FeSe layers cannot be determined by STM, taking the well observable moiré structure in the topographic image into account the assumption that the adlayers consist of no more than 3-5 MLs is further supported.

Atomic resolution STM measurements are performed on the thinnest FeSe thicknesses, which are identified as such by their having the greatest intensity variations in the moiré pattern. Note that this layer thickness is also the predominant thickness observed on the samples. The atomically resolved STM images in fig. 3.5(a) and (b) show the hexagonal surface unit cell of Bi_2Se_3 before the growth, with a lattice constant of 0.418(0.006) nm, and the square unit cell of the FeSe adlayer, with a lattice constant of 0.38(0.01) nm. The intensity modulation in fig. 3.5(b) is assigned to the moiré superstructure, which is even better visible in the atomically resolved image. Furthermore, the FeSe thin film exhibits two types of defects, A and B. Type A defects show two enhanced brighter spots on neighboring atom sites and are ascribed to a Se atom on or close to an Fe vacancy⁸⁸ or an Fe site^{53,89,90}. The signature of type B defects are a darker suppression at an atomic site at the top of the thin film and its origin is unknown.

The structural characterization is complemented with LEED measurements of the pristine Bi_2Se_3 and the FeSe thin films on Bi_2Se_3 , as seen in fig. 3.5(c) and (d). The bare Bi_2Se_3 surface exhibits the characteristic hexagonal reciprocal lattice in LEED; for the FeSe adlayer a square diffraction pattern for each of the three rotational domains is observable (indicated by brown, yellow and orange arrows), accompanied with dotted streaks-like satellite spots at each of the primary spots. The satellites are caused by the 1D-moiré structure. The lattice constants and moiré periodicity determined by LEED are 0.38(0.01) nm and 6.3(0.2) nm, respectively, and agree well with the STM values.

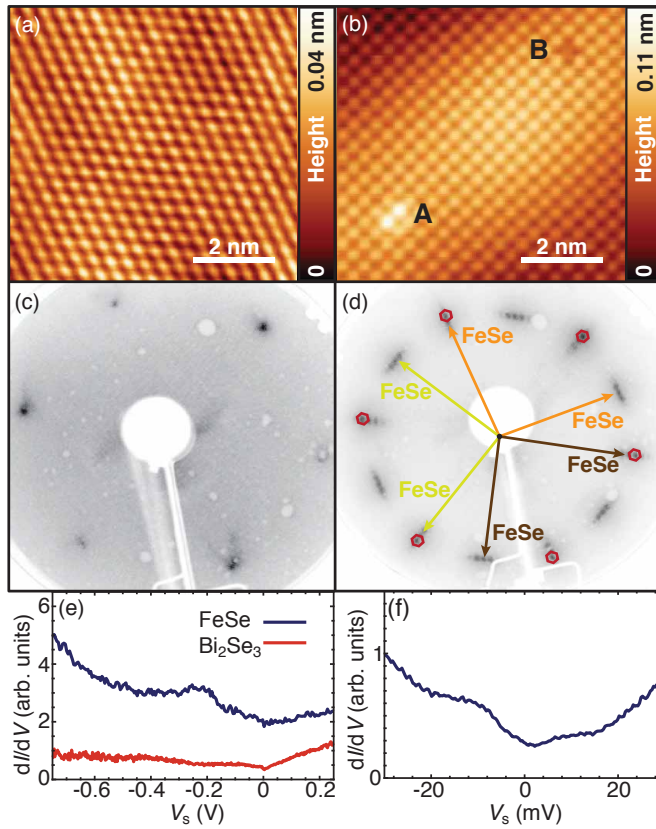


Figure 3.5: Top: atomically resolved STM images at 5 K of (a) clean Bi₂Se₃ before the growth and (b) FeSe thin films on Bi₂Se₃. The defects A and B are marked (more information in the text). Middle: LEED images for a kinetic energy of 50.2 eV at 90 K for (c) clean Bi₂Se₃ before the growth and (d) FeSe thin films on Bi₂Se₃. The LEED pattern of FeSe thin films on Bi₂Se₃ consists of a superposition of three square reciprocal unit cells corresponding to the FeSe domains rotated by 120° (marked with brown, orange and yellow colored arrows) and the hexagonal surface lattice of Bi₂Se₃ (red hexagons). The dotted streaks at main diffraction spots of FeSe are attributed to the linear moiré superstructure. Bottom: (e) large range STS spectra taken on FeSe thin films (blue, shifted for better visibility) and the Bi₂Se₃ (red). A peak at -225 meV for FeSe thin films is visible. Tunneling parameters: blue: $V_s = 1$ V, $I_t = 500$ pA, $V_{mod} = 4$ mV; red: $V_s = 250$ mV, $I_t = 500$ pA, $V_{mod} = 0.5$ mV. (f) A characteristic high-resolution STS spectrum near the Fermi energy acquired on the thinnest FeSe thickness. No superconducting gap is observable. Tunneling parameters: $V_s = 50$ mV, $I_t = 500$ pA, $V_{mod} = 0.5$ mV.

3.2.3 Electronic Structure of FeSe Thin Films on Bi₂Se₃

ARPES is a spatially averaging techniques that probes simultaneously, in the case of FeSe on Bi₂Se₃, the bare substrate and the adlayer, including multiple domains within the beam spot (200 $\mu\text{m} \times 50 \mu\text{m}$). Therefore, photoemission spectra contain a superposition of all these signals. Selected photon energies are chosen to exploit the photon energy dependent matrix elements and enhance special features of the band structure of the adlayer and the substrate.

The photoemission intensity along the high symmetry directions $\bar{\Gamma}$ - $\bar{M}_{\text{Bi}_2\text{Se}_3}$ and $\bar{\Gamma}$ - $\bar{K}_{\text{Bi}_2\text{Se}_3}$ ⁴ are shown in fig. 3.6(a) and (b), respectively. Two separated Dirac cones with different amounts of doping are clearly observable. Comparing the photoemission spectra with the bare Bi₂Se₃ spectra shown in fig. 3.1(d) and Ref.⁹¹ suggests that the less n-doped Dirac cone originates from pristine Bi₂Se₃ while the more n-doped state is a stable topological surface state buried beneath the FeSe adlayer. The rigid shift of the substrate's electronic structure suggests indirectly an accompanying p-doping of the FeSe adlayer. In consideration of the short IMFP of the excited photoelectrons, the observation of the interlayer topological surface state further supports the interpretation that there are only a few layers of FeSe layers grown on Bi₂Se₃.

Furthermore, a broad and non-dispersing photoemission feature is observable at a binding energy of around 0.2 eV in fig. 3.6(a) and (b) (marked with blue arrow). The same state is also observable at photon energy of 26 eV in fig. 3.7(b) (also marked with blue arrows). This feature is assigned to the FeSe thin film, as it is not visible on clean Bi₂Se₃ in fig. 3.1(d).

The constant binding energy cuts in fig. 3.6(c) reveal a prominent hexagonal warping of both topological surface states at the Fermi level which enclose the conduction band feature at $\bar{\Gamma}$. However, with increasing binding energy the topological surface state contour alters from a hexagonal to a circular shape⁹². The binding energies of the buried and bare Bi₂Se₃ Dirac points are observed at 0.72 eV and 0.36 eV, respectively.

Fig. 3.6(d) shows the photoemission intensity integrated in a 110 meV range around the Fermi level to enhance features near the Fermi energy. By identifying the Bi₂Se₃ BZ centers $\bar{\Gamma}$ and $\bar{\Gamma}'_{\text{Bi}_2\text{Se}_3}$, the first and second BZ can be constructed. Furthermore, the LEED pattern in fig. 3.5(d) reveals the orientation of the three domains of FeSe with respect to Bi₂Se₃, and this is used here to align the three FeSe BZs relative to the Bi₂Se₃ BZ as seen in fig. 3.6(d). Besides the already discussed

⁴ $\bar{\Gamma}$ marks the center of the primary surface BZ and the subscripts on all other high-symmetry point labels the corresponding high-symmetry point of the material.

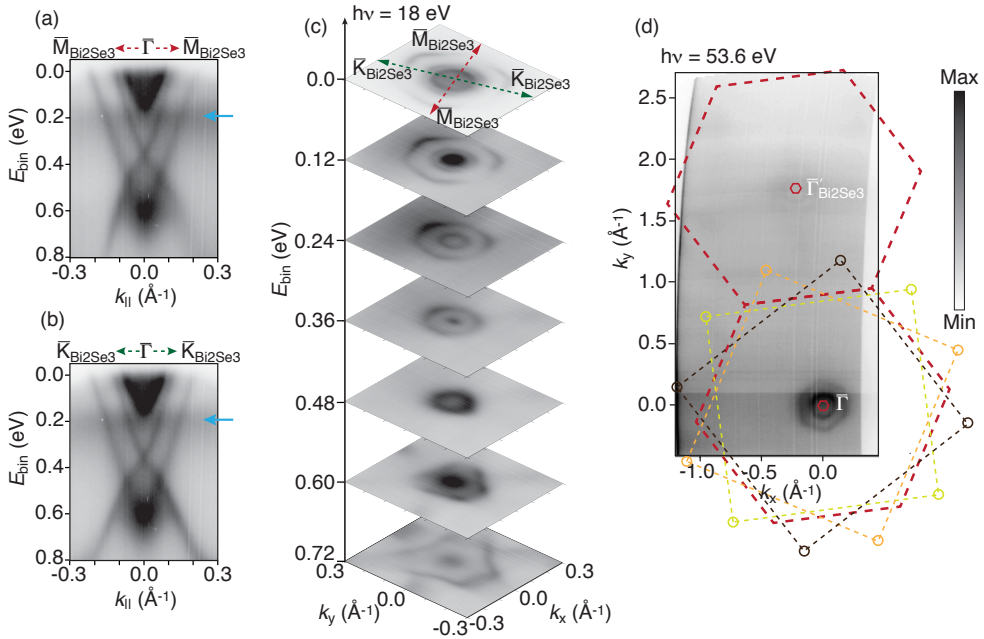


Figure 3.6: Photoemission intensity of FeSe thin films on Bi_2Se_3 along (a) $\bar{\Gamma}$ - $\bar{M}_{\text{Bi}_2\text{Se}_3}$ and (b) $\bar{\Gamma}$ - $\bar{K}_{\text{Bi}_2\text{Se}_3}$ directions, acquired at a temperature of 90 K with a photon energy of 18 eV. Two Dirac cone-like dispersions are observable. The red and green dashed arrows mark the directions in the k_x - k_y -plane of the cuts through the BZ of Bi_2Se_3 . The blue arrow indicates a non-dispersive FeSe feature at a binding energy of around 0.2 eV. (c) Photoemission intensity along constant energy contours at different binding energies exhibit clearly both topological surface states. (d) Constant energy contour acquired across a wider range of momenta, obtained by integrating the spectral weight in a range 110 meV around the Fermi level at a photon energy of 53.6 eV. The orientation of the hexagonal Bi_2Se_3 BZ (red dashed line) and the BZ of the three domains of FeSe (brown, orange and yellow dashed lines) are shown. The small colored circles indicate the \bar{M}_{FeSe} points of FeSe, and the $\bar{\Gamma}$ points of Bi_2Se_3 are marked with small red hexagons.

three features around $\bar{\Gamma}$ which are also observable at $\bar{\Gamma}'_{Bi_2Se_3}$ with suppressed intensity due to geometry and matrix elements effects, no other feature is visible at this photon energy.

Fig. 3.7(a) shows a Fermi surface acquired with a photon energy of 26 eV, which enhances the photoemission features from the FeSe thin films. In addition to photoemission signal stemming from the Bi_2Se_3 , which are still well observable, a new relatively weak features is visible at \bar{M}_{FeSe} . The adjusted contrast in the inset of fig. 3.7(a) reveals a small round intensity enhancement on the left hand-side (towards the first FeSe BZ) of \bar{M}_{FeSe} , and by further careful inspections another weaker round feature on the right hand-side side (towards the second FeSe BZ) is observable; these two features form together a dumbbell-like feature across the FeSe BZ boundary. The suppression of intensity for the lobe in the second BZ can presumably be assigned to matrix element effects mentioned above.

The photoemission intensity along the $\bar{\Gamma}\bar{X}_{FeSe}\bar{M}_{FeSe}\bar{\Gamma}$ directions in fig. 3.7(b) reveals that the dumbbell-like feature originates from a faint photoemission intensity near the Fermi surface. To investigate this faint feature more in detail, an analysis method based on the mathematical concept of curvature is used, which enhances the details of weak photoemission intensities on intense backgrounds⁹³. The curvature plot of the photoemission intensity along $\bar{\Gamma}\bar{X}_{FeSe}\bar{M}_{FeSe}\bar{\Gamma}$ directions in fig. 3.7(c) reveals that a small electron pocket located near \bar{M}_{FeSe} at the Fermi level forms the dumb-bell like feature (marked with green arrows).

In previous photoemission experiments on FeSe thin films on $SrTiO_3$, a circular features near \bar{M}_{FeSe} was associated with the superconductive phase of ML FeSe, while a similar dumb-bell like feature was observed for non-superconducting 3 ML films^{23,94,95}. Fig. 3.8(b) and (f) show the Fermi contour of the non-superconducting phase from Ref.²³ together with the Fermi contour from fig. 3.7(a) to underline the similarity of the photoemission features near \bar{M}_{FeSe} for the two systems. For further comparison, cuts through $\bar{\Gamma}$ (marked with blue line) and through \bar{M}_{FeSe} (marked with green line) and the corresponding curvature cuts of FeSe on Bi_2Se_3 are shown in fig. 3.8(c)-(d) together with similar cuts of 3 ML FeSe on $SrTiO_3$ in fig. 3.8(g). The direct comparison reveals that both multilayer FeSe samples exhibit a similar dome-like feature at $\bar{\Gamma}$ and a small electron pocket at \bar{M}_{FeSe} which leads to the formation of the dumbbell-like feature. In consideration of the findings in Ref.²³, together with the above presented STM results, a thickness of at least 3 ML is suggested for FeSe thin films on Bi_2Se_3 .

Complementary to the ARPES investigations, STS spectra were acquired in a

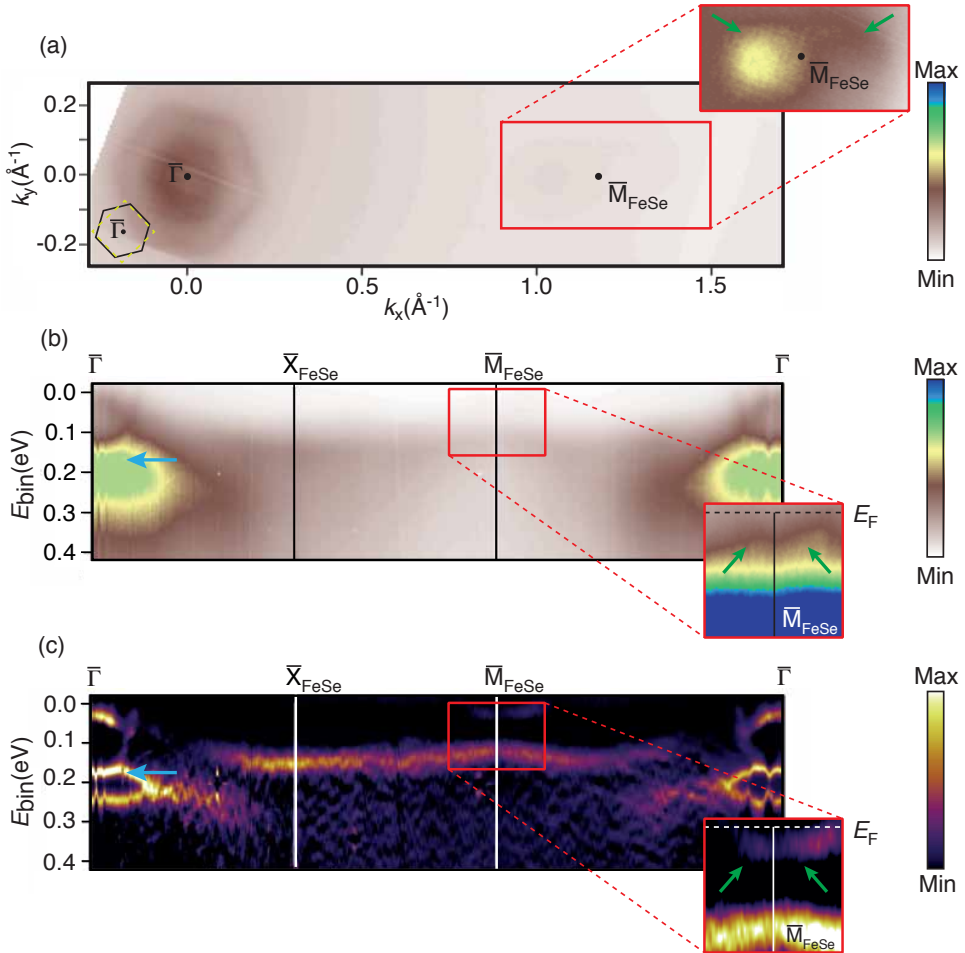


Figure 3.7: Overview of the photoemission intensity acquired with a photon energy of 26 eV at $T = 90$ K. (a) Fermi contour at the Fermi level for FeSe on Bi_2Se_3 . The corresponding high symmetry points of one of the FeSe domains are marked. The red square indicates the faint dumbbell-like feature around \bar{M}_{FeSe} . The red inset shows the faint feature with adjusted contrast and the green arrows mark the photoemission intensity of the faint dumbbell-like feature. A sketch of the BZ of the FeSe thin film (yellow dashed rectangle) and Bi_2Se_3 (black dashed hexagon) is shown in the bottom left inset. (b) Photoemission cut along the $\bar{\Gamma}\bar{X}_{\text{FeSe}}\bar{M}_{\text{FeSe}}\bar{\Gamma}$ directions, acquired with a photon energy of 26 eV and (c) its corresponding curvature plot. The faint feature is marked with green arrows and shown with adjusted contrast in the inset. The blue arrow indicates a non-dispersive FeSe feature at a binding energy of around 0.2 eV.

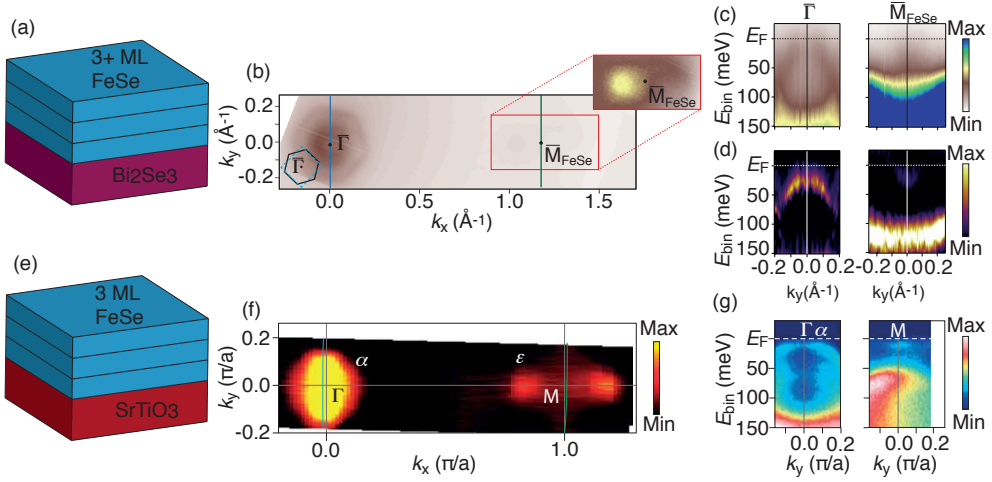


Figure 3.8: Comparison of photoemission spectra of 3+ ML of FeSe on Bi₂Se₃ and 3 ML of FeSe on SrTiO₃ adapted and modified from Ref.²³. (a) and (e) Schematic view of the different material systems. (b) and (f) Fermi contours of 3+ ML FeSe thin film synthesized on a Bi₂Se₃ and SrTiO₃, respectively. (c) and (g) photoemission intensity close to $\bar{\Gamma}$ and \bar{M} of the two systems, respectively. (d) Curvature plot of (c).

large energy range around the Fermi level on bare Bi₂Se₃ and FeSe thin films (fig. 3.5(e)). While the Bi₂Se₃ shows the typical STS spectrum⁹⁶ FeSe exhibits a characteristic broad peak at $V_s = -225$ mV, which is attributed to the non-dispersive feature marked with a blue arrow in fig. 3.6(a) and (b). Note that STS spectra were independent of the FeSe thickness.

High-resolution STS at $T = 5$ K was used to explore the possible existence of superconductivity. Fig. 3.5(f) shows one typical STS spectrum out of 400 measurements made on eleven different preparations of three different Bi₂Se₃ crystals. The measurements were made on different FeSe thicknesses and none showed a reproducible superconducting gap.

3.3 Bulk $\text{Fe}_{1.08}\text{Te}$

The following two sections are dedicated to the investigation of the crystal and electronic structure of bulk $\text{Fe}_{1.08}\text{Te}$ and FeTe thin films grown on Bi_2Te_3 using STM, LEED, ARPES and first principles calculations. STM measurements were performed in a collaboration with the group of Prof. Roland Wiesendanger (Universität Hamburg). Using the electronic structure results from the bulk $\text{Fe}_{1.08}\text{Te}$ it is possible to partly disentangle the contributions from three different rotational domains of the FeTe thin film. Furthermore, no significant change of the film's electronic structure is observed by alkali doping of the surface. The doping behavior is further supported by ab-initio calculations, performed by the group of Prof. Tim Wehling (Universität Bremen).

3.3.1 Structural and Electronic Analysis of Bulk $\text{Fe}_{1.08}\text{Te}$

So far, the focus in this thesis has been on thin films of FeSe a system which has been well studied in terms of substrate effects, excess Se, the influence of electronic structure on the superconducting behavior,^{22,56,57,59,71} while little work has been performed on FeTe thin films, a material which is not a bulk superconductor and exhibits as thin films grown on Bi_2Te_3 a critical temperature of 6 K⁶¹.

High-quality Fe_{1+y}Te single crystals were synthesized by the group of Prof. Martin Bremhold (Aarhus University) using the flux method: see Ref.⁹⁷. As the properties of bulk Fe_{1+y}Te depend strongly on the amount of excess Fe (y) in the system it was kept as low as possible⁷²⁻⁷⁴. X-ray diffraction led to an excess Fe content for the used crystals of $y \approx 0.08$. DFT calculations of the electronic structure for bulk FeTe ($y = 0$) and freestanding SL FeTe were performed by the group of Prof. Tim Wehling (Universität Bremen) and are shown in fig. 3.3(a), (b) and (c). The STM measurements were acquired by the group of Prof. Roland Wiesendanger (Universität Hamburg) with a homebuilt variable temperature STM in UHV where the sample and the tip were cooled down to 32 K^{98,99}.

The layered $\text{Fe}_{1.08}\text{Te}$ crystals were prepared by cleaving in air until a smooth surface was achieved. The samples were subsequently cleaved by the scotch tape method in UHV at room temperature to obtain a clean and adsorbate free surface. In atomically resolved STM images, the as-cleaved $\text{Fe}_{1.08}\text{Te}$ shows the square surface unit cell of FeTe but also excess Fe atoms which are visible as small circular bright protrusions as seen in fig. 3.10(a). Annealing at 430 K for 30 min removes the excess Fe resulting in a clean and high quality $\text{Fe}_{1.08}\text{Te}$ surface with a very low density of

defects as seen in fig. 3.10(b). Prior to acquisition of the ARPES data, the sample orientation was determined by LEED. A typical LEED pattern, shown in the inset of fig. 3.9(a), exhibits, besides the main diffraction points spots of the square surface lattice, small satellite spots which are attributed to crystallites with slightly different orientations. As the probing area of the LEED electron beam is around 1-2 mm in diameter, it is assumed that the dimensions of the crystallites are of the same order of magnitude. For ARPES measurements, it was verified that the light spot (horizontal diameter of 200 μm) was centered on one single domain of the $\text{Fe}_{1.08}\text{Te}$ crystal during data acquisition of an angle scan⁵. As already mentioned in section 3.1.3 instead of labeling the centre, edge and corner high symmetry points (*i.e.* as Γ , X and M), these points are labeled as the projected SBZ and marked in the following way with $\bar{\Gamma}$, \bar{M} and \bar{X} , respectively.

Fig. 3.9(a), (b) and (d) show the ARPES data of the cleaved bulk $\text{Fe}_{1.08}\text{Te}$ sample; in specific the photoemission intensity integrated in a 120 meV range around the Fermi level (fig. 3.9(a)) and high symmetry direction cuts through the BZ (fig. 3.9(b) and (d)). Note that identical high symmetry points in the different BZs are numbered starting with $\bar{\Gamma}_0$ for the first BZ and $\bar{\Gamma}_n$ ($n = 1, 2, \dots$) for subsequent BZs. The presented photoemission spectrum acquired at a sample temperature of 90 K in the paramagnetic state is characterized by overall broad features without the formation of a sharp quasiparticle peak close to the Fermi level consistent with previous findings for this material system¹⁰⁰⁻¹⁰². It is worth mentioning that the substitution of Te with only 10% Se in Fe_{1+y}Te results in much sharper and more well-defined electronic bands¹⁰³. A possible explanation for the remarkably strong difference between Fe_{1+y}Te and $\text{FeTe}_{1-x}\text{Se}_x$ may be strong electron correlation effects. Furthermore, previous studies on Fe_{1+y}Te show that strong matrix element effects suppress the photoemission intensity for specific light polarizations such that not all predicted bands are expected to be observable for the light polarization used at the SGM3 beamline^{77,100,104}. Using a photon energy of 65 eV, the photoemission features in the second BZ can be reached; see fig. 3.9(a). In the second BZ, the Fermi surface features, especially around $\bar{\Gamma}_1$, $\bar{\Gamma}_2$ and \bar{M}_1 , are clearer while in the first BZ, particularly near $\bar{\Gamma}_0$ and \bar{X} , only very broad features are observed. As the band structure features details are clearer in the second BZ we will focus here the following discussion.

Fig 3.9(b)-(e) show the band structure of bulk $\text{Fe}_{1.08}\text{Te}$ along the $\bar{\Gamma}_1\bar{M}_1\bar{\Gamma}_2$ and

⁵Angle scan: the sample is rotated around the axis of the manipulator (Θ) to measure the band structure from specified points in the BZ.

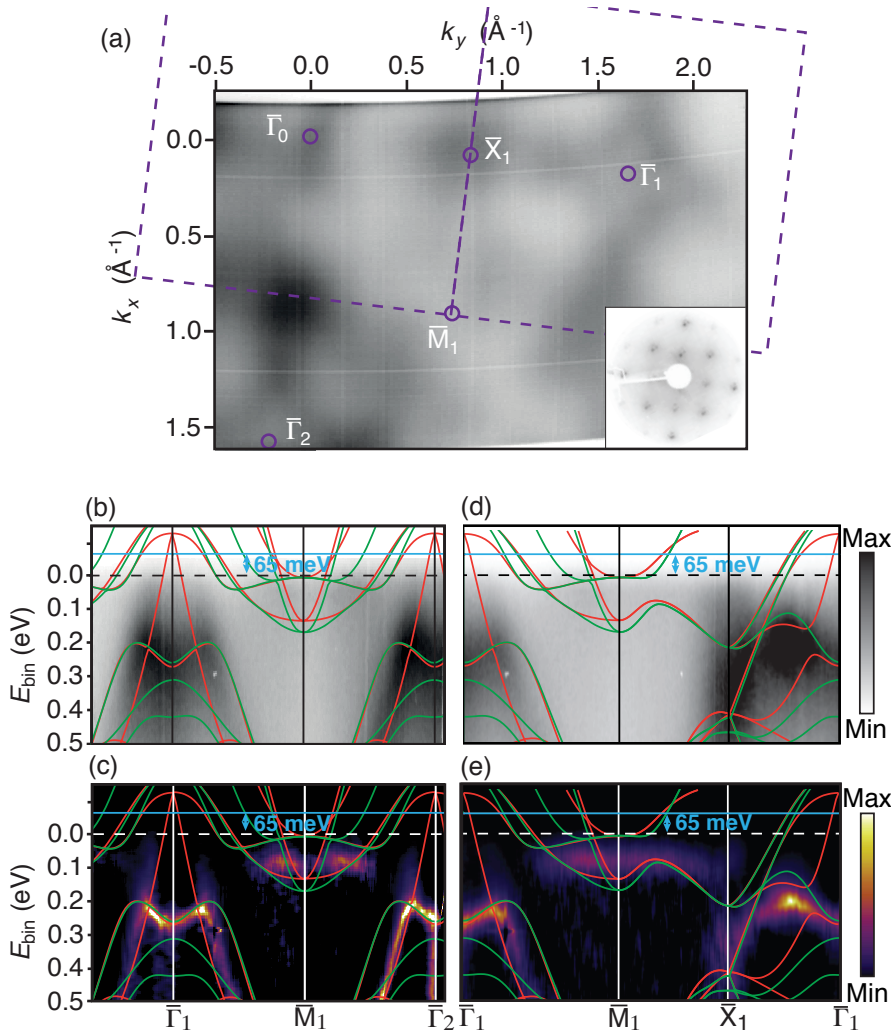


Figure 3.9: Photoemission data from bulk $\text{Fe}_{1.08}\text{Te}$ at a photon energy of $h\nu = 65\text{ eV}$ and at a temperature of 90 K . (a) Constant energy contour integrating the photoemission intensity over a range of 120 meV around the Fermi energy. The purple dashed lines mark the $\text{Fe}_{1.08}\text{Te}$ first and second BZs with the corresponding high symmetry points (small purple circles). An exemplary LEED pattern used to determine the orientation of the sample ($E_{\text{kin}} = 128\text{ eV}$) is shown in the inset. (b) Photoemission spectra along the $\bar{\Gamma}_1\bar{M}_1\bar{\Gamma}_2$ directions and (c) the corresponding curvature plot. The solid green and red lines are DFT calculations for the dispersion in the Z - A - R and the Γ - M - X plane, respectively. For best agreement with the experimental data the predicted band structure was renormalized (renormalization factor) by a factor of around 2 and shifted in binding energy. The dashed white and black lines indicate the Fermi level of the experimental data, while the light blue line indicates the position of the Fermi level determined from DFT. (d) Photoemission spectra along the $\bar{\Gamma}_1\bar{M}_1\bar{X}_1\bar{\Gamma}_1$ directions and (e) the corresponding curvature plot.

$\bar{\Gamma}_1\bar{M}_1\bar{X}_1\bar{\Gamma}_1$ directions, and their corresponding curvature plots⁹³ with the predicted band structure of bulk FeTe, from fig. 3.3(b), superimposed. For a detailed investigation of the ARPES results the 3D character of the Fe_{1.08}Te crystal has to be considered or in other words the momentum component perpendicular to the interface \mathbf{k}_\perp is not conserved during the photoemission process and hence the observed photoemission dispersion along the high symmetry directions cannot be assigned to the corresponding k_\perp . Furthermore, it cannot be assumed that the initial state of k_\perp is constant for covering a Fermi surface scan along two BZs at a fixed photon energy. This is not a serious concern for most states which exhibit quasi 2D character. However, in order to compare the experimental photoemission intensity in a meaningful manner with the DFT calculations, the predicted band structure of the middle plane of the 3D BZ (Γ - M - X , red solid line) and the corresponding band structure from the edge of the 3D BZ (along Z - A - R , green solid line) are superimposed on the ARPES results.

The photoemission spectra together with the predicted band structures shown in fig. 3.9(b)-(e) reveal features with distinct 3D character, i.e. band dispersion in k_\perp (see difference in green and red bands). The innermost red hole pocket around $\bar{\Gamma}_1$ exhibits strong 3D character and is even suppressed in the Z - A - R plane (green), a behavior which is expected from the d_{xz}/d_{yz} orbital character of this band⁷⁷. Other bands show strong 2D behavior, indicated by small dispersion in the Γ - Z direction and this is seen on the "camel-back" shaped band near $\bar{\Gamma}$ at a binding energy of ≈ 250 meV and the electron pockets around \bar{M} . These quasi 2D bands are not affected by broadening effects in k_\perp and assumed to be narrower in photoemission. Therefore, the "camel-back" shaped bands at $\bar{\Gamma}$ are used to align the predicted band structure and the best apparent agreement is achieved for a renormalization factor (see section 3.1.3) of around 2 and a rigid band shift of 65 meV to higher binding energy. Similar renormalization factors were required in previous studies for bulk Fe_{1+y}Te and were attributed to correlation effects¹⁰⁰. The band shift sounds consistent with a small p-doping of the Fe_{1.08}Te crystal. However, it is to point out that orbitally dependent many body renormalizations are also known to lead to a shift of special spectral features⁷⁸.

While the predicted hole pocket at $\bar{\Gamma}_1$ is clearly visible in the photoemission spectra in the second BZ, its intensity is suppressed around normal emission at $\bar{\Gamma}_0$. This character of the band structure emphasizes the strong effect of the matrix elements of this material and also justifies the significance of using the correct crystallographic "2-Fe" BZ instead of the "1-Fe" BZ which should not exhibit by necessity a hole pocket

at this location. The very intense photoemission intensity along the $\bar{X}_1\text{-}\bar{\Gamma}_1$ direction stems presumably from overlapping multiple broad bands. In order to visualize faint spectral weight in the presented photoemission spectra the curvature method is used as seen in fig. 3.9(c) and (e). The existence of an electron pocket at \bar{M} is observed, however, the intensity of these bands decrease closer to the Fermi level and are not longer visible even when the curvature method is used.

A further investigation of the Fermi surface in the second BZ shows the existence of a feature at \bar{X}_1 , which is not expected by the band structure calculations. A similar feature has been observed in several studies of bulk Fe_{1+y}Te ^{100,102} but the origin could not be determined. However, fig. 3.9(d) suggests that the unknown feature arises from a strong photoemission intensity at higher binding energy near \bar{X}_1 .

Before we present the study on the crystal and electronic structure of FeTe thin films on Bi_2Te_3 , and the effect of Rb surface doping on the electronic structure of the film, we characterize the distribution of Rb atoms on $\text{Fe}_{1.08}\text{Te}$ crystals using STM.

Single Rb atoms have been deposited by resistance heating of a (SAES) alkali metal dispenser facing the sample surface (sample temperature was maintained at 150 K). The coverage was determined by the ratio of Rb atoms compared to Fe atom in the Fe_{1+y}Te surface. Before depositing the Rb, the $\text{Fe}_{1.08}\text{Te}$ sample was annealed to 430 K to remove the excess Fe on the surface as seen in fig. 3.10(a) and (b).

STM images of increasing coverages from 0.5% to 4.5% are displayed in fig. 3.10(c)-(f) as labeled. The atomically resolved images reveal a distribution of single Rb atoms, appearing as circular protrusions with an apparent height of 1.4 Å, as shown by the line profile in fig. 3.10(g). A similar apparent height has been observed for single Rb atoms adsorbed on Bi_2Se_3 ¹⁰⁵. The STM images show that the Rb atoms do not cluster and form a very homogeneous, highly ordered distribution of Rb, best observable at a Rb coverage of 3.0% and 4.5% (fig. 3.10(e) and (f)).

This interpretation is further supported by an analysis of the coverage dependent distances between the Rb atoms. To this end, the insets in fig. 3.10(c)-(f) visualize the autocorrelation of the Rb atom positions within a $50\text{ nm}\times 50\text{ nm}$ area for each coverage. The autocorrelation images locate the displacement of all surrounding atoms with respect to a given atom, summed over all individual atoms and reveal a distribution on a square lattice¹⁰⁵. Most notably, the autocorrelation images exhibit a rather large unoccupied area in the center, clearly indicating a repulsive interaction between the Rb atoms. We attribute this interaction to the Coulomb repulsion between the Rb atoms which are presumably donating electrons to the substrate and thereby

become charged. Even though this experiment was carried out on the surface of a bulk $\text{Fe}_{1.08}\text{Te}$ crystal, a similar distribution of the Rb atoms might be expected for FeTe thin films.

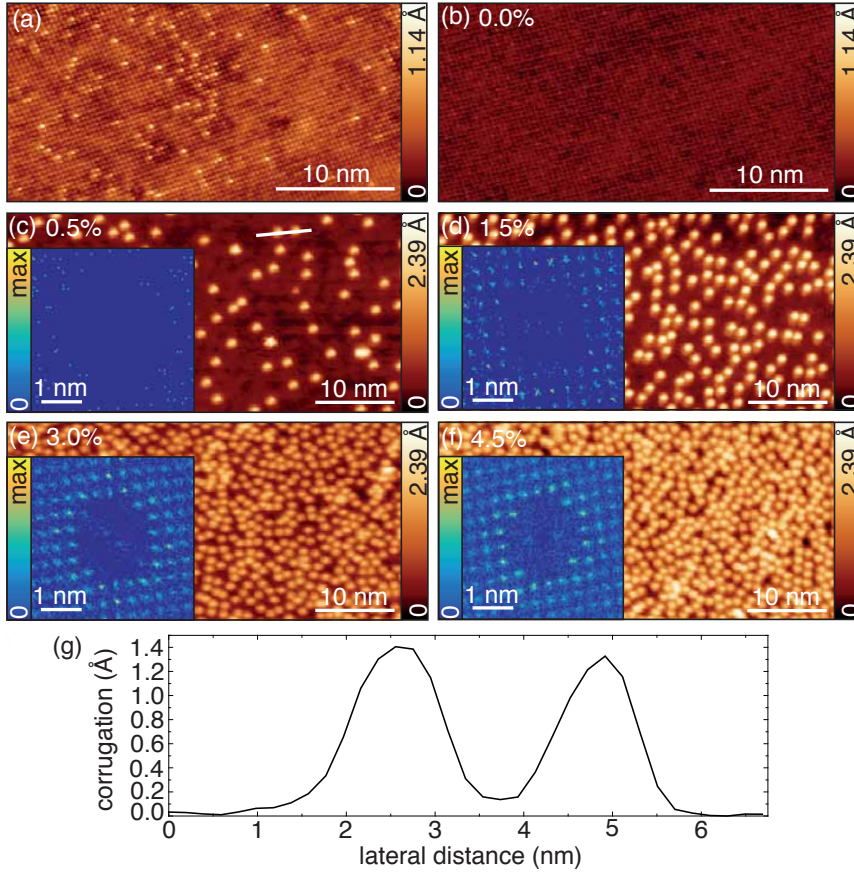


Figure 3.10: STM investigation of bulk $\text{Fe}_{1.08}\text{Te}$ for different Rb coverages. Constant current images of pristine bulk $\text{Fe}_{1.08}\text{Te}$ (a) before and (b) after annealing. (c)-(f) Constant current images of increasing Rb coverages on $\text{Fe}_{1.08}\text{Te}$ as labeled in each panel. The insets show the autocorrelation plots of the atom positions. (g) Line profile across two Rb atoms as marked by the white line in (c). Tunneling parameters: (a) $V_s = 40$ mV, $I_t = 150$ pA; (b) $V_s = 20$ mV, $I_t = 250$ pA; (c)-(f) $V_s = 1$ V, $I_t = 50$ pA.

3.4 FeTe Thin Films on Bi₂Te₃

3.4.1 Growth of FeTe Thin Films on Bi₂Te₃

FeTe thin films on Bi₂Te₃ samples and STM measurements were obtained as part of a collaboration with the group of Prof. Roland Wiesendanger (Universität Hamburg). For ARPES measurements the thin film samples, which were prepared at the Universität Hamburg, were transported in situ in a vacuum suitcase to the SGM3 endstation.

The synthesis of FeTe thin films on Bi₂Te₃ is based on a well-known approach documented in the literature^{57,61,106,107}, and is mostly analogous to the growth of FeSe thin films on Bi₂Se₃ as outlined in section 3.2.1 of this thesis. Firstly, the Bi₂Te₃ crystals, which are synthesized using a Stockbarger method⁶¹, are pre-cleaved in air and subsequently in UHV to achieve a clean surface without adsorbates. Before Fe is deposited with an electron beam evaporator on the surface of the crystal, the quality of substrate is checked with STM. The substrate is annealed for 30 min at 588 K in order to trigger Te segregation from the bulk to the surface and to introduce the formation of a FeTe adlayer. Note that during the annealing process the Bi₂Te₃ surface is partly fractured due to segregation of Te from the top quintuple layer¹⁰⁸. Ultimately this leads to the formation of embedded FeTe adlayers of different thicknesses on the Bi₂Te₃ substrate^{61,106}.

3.4.2 Structural Analysis of FeTe Thin Films on Bi₂Te₃

The combination of a three-fold substrate and a two-fold adlayer leads to the formation of three rotational domains of FeTe thin films with respect to Bi₂Te₃ as seen already in the case of FeSe thin films on Bi₂Se₃ in section 3.2. Before investigating the averaged electronic structure of the three rotational domains we will focus first on the local characterization with STM.

Fig. 3.11(a) shows the atomic resolution image of bare Bi₂Te₃ and two rotational domains of FeTe which are separated by a grain boundary marked with black arrows. The signature of Bi₂Te₃ is a hexagonal surface lattice (grey scale), while the FeTe thin films exhibit a surface square lattice (orange color scale). The simultaneous imaging of the Bi₂Te₃ and the FeTe atomic surface lattice not only reveal directly the orientations of the substrate and the adlayer with respect to each other but also shows the rotational domains of the FeTe thin film (indicated by colored lines). Therefore, it is evident that FeTe thin films grow in three domains on Bi₂Te₃ rotate by 0, 120°

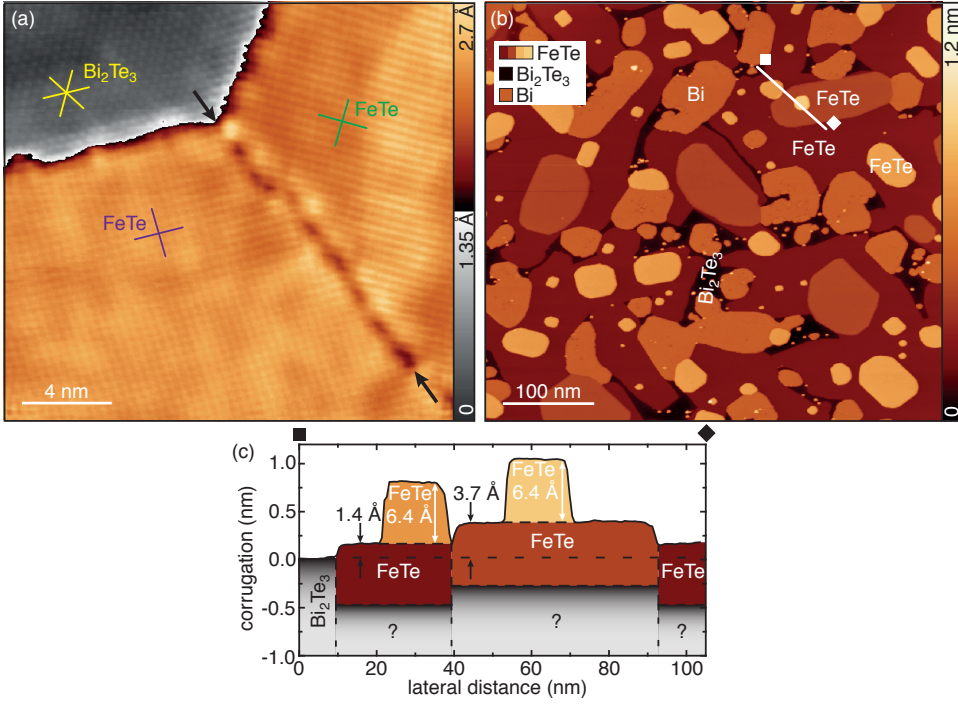


Figure 3.11: (a) Atomically resolved STM image showing two different rotational FeTe domains (square lattice, orange color scale) and bare Bi₂Te₃ (hexagonal lattice, grey scale). The black arrows indicate the grain boundary separating the two rotational domains of the FeTe thin films. The colored lines mark the orientation of the atomic lattices; purple and green for FeTe, yellow for Bi₂Te₃. Tunneling parameters: $V_s = -200$ mV, $I_t = 300$ pA. (b) Typical overview STM image of the FeTe thin films grown on Bi₂Te₃ sample investigated by ARPES. Tunneling parameters: $V_s = -400$ mV, $I_t = 100$ pA. The line profile plotted in (c) marks the apparent height along the solid white line in (b). The FeTe layers are visualized in a color-code corresponding to the colors in (b).

and 240° with respect to each other.

Fig. 3.11(b) shows a typical overview image of the FeTe layers surrounded by the Bi₂Te₃ substrate. The height profile in fig. 3.11(c) along the white line in (b) exhibits apparent heights of 1.4(0.1) Å and 3.7(0.1) Å with respect to the Bi₂Te₃ surface, which is much lower than the reported apparent height of 6.25 Å for the bulk FeTe unit cell¹⁰⁹. These findings suggest that similar to the FeSe thin film on Bi₂Se₃ case, the FeTe islands are embedded in the Bi₂Te₃ quintuple layer and further strongly point to the possibility of the integration of FeTe layers in the partly fractured topmost Bi₂Te₃ quintuple layer. In contrast to FeSe thin films on Bi₂Se₃ no clear linear moiré structure is visible in the case of FeTe thin films on Bi₂Te₃. The suppression of the moiré in STM is in line with a strongly fractured Bi₂Te₃ quintuple layer located under the FeTe film, on the other hand a multiply stacked FeTe layers would also result in a suppression of the moiré. However, FeTe layers grown on-top of the incorporated FeTe islands exhibit an apparent height of 6.4(0.1) Å which is close to the value of 6.25 Å for the thickness of a single bulk unit cell of FeTe¹⁰⁹. Besides the FeTe layers, islands with rough edges labeled with Bi and an apparent height of 4.8(0.1) Å are also observable in fig. 3.11(b). This apparent height is in good agreement with reported single Bi bilayer on Bi₂Te₃ of 4.7 Å and suggests that these islands are accumulated residual Bi from the FeTe thin film synthesis¹¹⁰. As the different surface regions are identified now, the overall coverage for the lowest apparent height of FeTe thin film can be determined to be ~ 70% with a ~ 10% grown on-top layer. Note that it can not be excluded that additional FeTe layers are formed under the embedded FeTe layers.

3.4.3 Electronic Structure of FeTe Thin Films on Bi₂Te₃

In contrast to STM, ARPES probes all three rotational domains within the beam spot size (200 μm × 50 μm) which leads to difficulties in the interpretation of the photoemission data. In this section a step-by-step guideline is presented to disentangle the complex photoemission features of FeTe thin films on Bi₂Te₃, exploiting the experience with the previously presented electronic structure of bulk Fe_{1.08}Te (section 3.3).

Fig. 3.12(a) shows the photoemission intensity of FeTe thin films on Bi₂Te₃ integrated in a 120 meV range around the Fermi level at a photon energy of $h\nu = 65$ eV. The complex Fermi contour consists of three prominent features: a star-like photoemission intensity around $\bar{\Gamma}_0$, a ring with slightly modulating intensity at ≈ 0.8 Å⁻¹

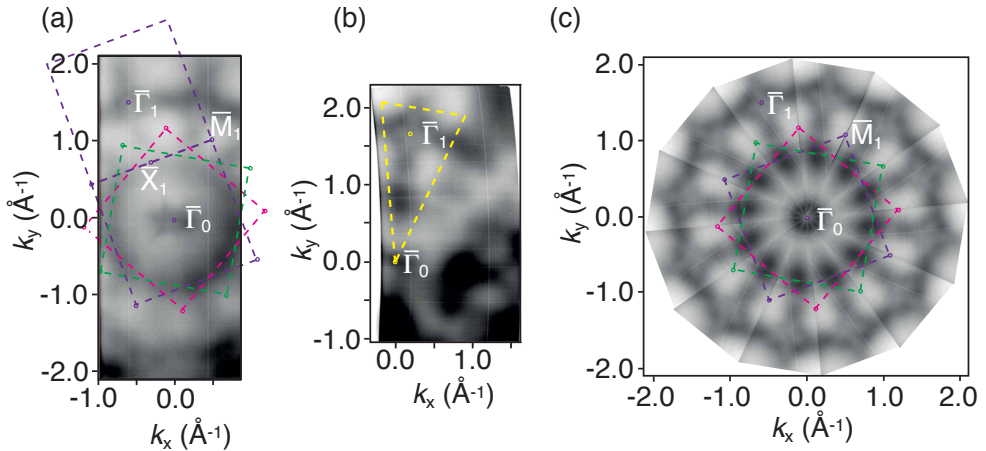


Figure 3.12: Comparison of the FeTe thin film and bulk $\text{Fe}_{1.08}\text{Te}$ Fermi contours acquired at a photon energy of 65 eV and a temperature of 90 K. (a) Photoemission intensity of thin film FeTe integrated over a 120 meV range around the Fermi energy. The BZ of the three rotational domains (120° to each other) are marked with colored dashed lines (pink, purple and green). The high symmetry points $\bar{\Gamma}_0$, \bar{M}_1 , \bar{X}_1 and $\bar{\Gamma}_1$ are labeled for the purple BZ and marked by small purple circles. (b) and (c) Construction of the thin film Fermi surface from the bulk one: (b) constant energy contour of bulk $\text{Fe}_{1.08}\text{Te}$ from fig. 3.9(a) but slightly saturated in contrast. The yellow dashed 30° wedge marks the area which is used for constructing the thin film Fermi surface. (c) By rotating the yellow wedge of (b) in steps of 30° the thin film Fermi surface is obtained.

and a periodic repetitive cross like feature at $\approx 1.7 \text{ \AA}^{-1}$ similar to that observed in bulk $\text{Fe}_{1.08}\text{Te}$ around $\bar{\Gamma}_1$ (fig. 3.9(a)).

In ARPES one observes the incoherent superposition of photoemission intensity for the different domains of the FeTe thin films, which results in a complex and confusing Fermi contour as seen in fig. 3.12(a). In order to disentangle the mix of electronic band structures one has to identify the contribution of each rotational domain. The cross like feature can be ascribed to the $\bar{\Gamma}_1$ point of bulk $\text{Fe}_{1.08}\text{Te}$ as seen in fig. 3.9(a) and serves as anchor point to determine the orientation of the BZs of the FeTe thin films. The three rotational domains of the FeTe thin film BZ are marked by the colored dashed lines (pink, purple and green) in fig. 3.12(a). The thin film Fermi surface can now be constructed by using the bulk $\text{Fe}_{1.08}\text{Te}$ photoemission data as explained in the remainder of this paragraph. Fig. 3.12(b) shows the exact same photoemission data of bulk $\text{Fe}_{1.08}\text{Te}$, as in fig. 3.9(a), but with slightly saturated

color-scale. The superimposed yellow 30° wedge contains all prominent features of the bulk Fe_{1.08}Te Fermi contour. By rotating the yellow wedge in 30° steps with respect to the equivalent directions of the three FeTe thin film domains, a similar looking Fermi contour in fig. 3.12(c) is constructed, as seen in the photoemission data for the thin film in fig. 3.12(a).

However, a closer inspection reveals minor variations between the thin film and the bulk Fermi contour in fig 3.12(a) and (b), respectively. The most evident change occurs around the cross-like feature at the $\bar{\Gamma}_1$ point. While in the bulk Fermi contour the cross-like feature exhibits a clear “hole” with weakened spectral intensity, the “hole” in the thin film contour is much smaller in diameter. Note that the cross-like feature is consistent with the Fermi contour expected from the presence of the calculated innermost hole pocket for bulk FeTe (fig. 3.3(a) and (b)) which is absent in the 2D case (fig. 3.3(c)). This not only shows the distinct 3D character of the FeTe thin film but also suggests that the smaller “hole” is associated with a lower p-doping of the thin film compared to the bulk case. However, due to very broad bands and polarization effects a determination of the doping based on the changes in the Fermi surface is not reliable. Furthermore, it has to be noted that a comparison of doping between thin films and bulk samples is a difficult point to address because screening, confinement effects or strain might alter the Fermi surface shape of the thin film¹¹¹.

However, a charge transfer from the FeTe adlayer to the substrate can be indirectly observed in a shift of the substrate’s band structure upon formation of the FeTe thin film. Hereby, we exploit the photon energy dependent photoemission cross section of the adlayer and the substrate to simultaneously enhance the Bi₂Te₃ and suppress partly the FeTe photoemission contribution for a photon energy of 20 eV. Fig. 3.13 shows an overview of the photoemission data for bare Bi₂Te₃ and covered with FeTe thin films. The Fermi contour and the dispersion along the $\bar{K}\bar{\Gamma}\bar{K}$ direction for the as-cleaved Bi₂Te₃ in fig. 3.13(a) and (c), respectively, show that the VBM and the Dirac point are located close to the Fermi level resulting in the topological surface state located in the unoccupied bands and therefore not reachable with ARPES. In the opposite situation the FeTe covered surface exhibits a strongly warped hexagonal Fermi contour of the topological surface state with an overall shift of the states to higher binding energies as seen in fig. 3.13(b) and (d). This is a sign of strong electron doping in the first layers of Bi₂Te₃ which is accompanied by p-doping in the FeTe thin films. The charge transfer is effectively so strong that it give rise to a Rashba-split two-dimensional electron gas in the conduction band states^{112,113} which is also observable in the Fermi contour as a weak spectral weight surrounded by the

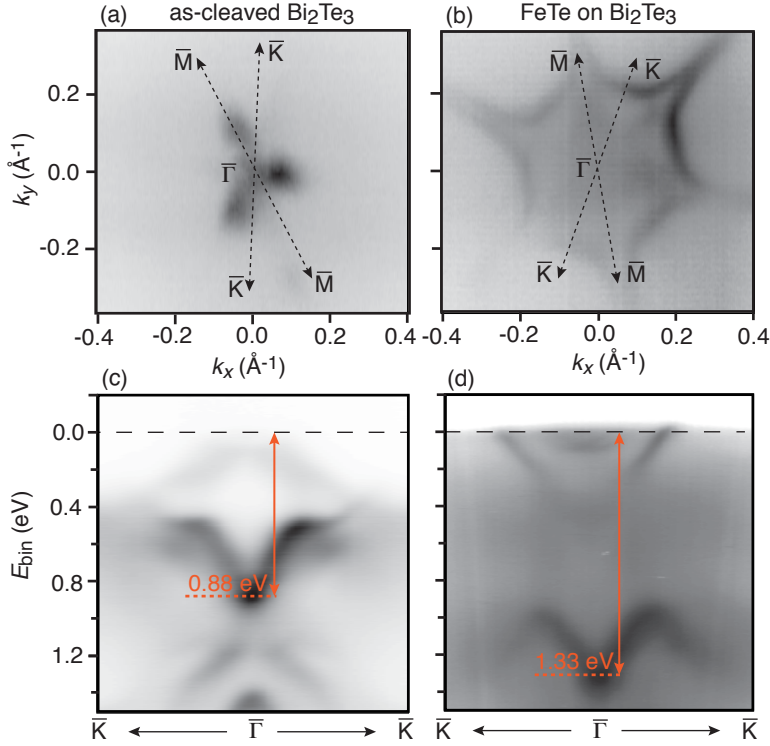


Figure 3.13: Doping behavior of the substrate acquired at a photon energy of 20 eV and at a temperature of 90 K. (a)-(b) Photoemission intensity integrated in a 3 meV range around the Fermi energy and (c)-(d) high symmetry cuts along the $\bar{K}\bar{\Gamma}\bar{K}$ direction for the clean Bi_2Te_3 and FeTe thin films on Bi_2Te_3 , respectively. The orange dashed lines mark the minimum of the V-shaped surface state. The orange arrows illustrate the binding energy of the V-shaped surface state.

hexagonally warped topological surface state in fig. 3.13(b). The dispersion of the covered Bi_2Te_3 states are well observable and only slightly deformed. The intense V-like state, which is identified as a surface state of clean Bi_2Te_3 ¹¹⁴, can be used to determine the shift of the band structures to ≈ 450 meV to higher binding energy upon formation of the FeTe thin films. Overall these results point to a net charge transfer from the thin film FeTe layers to the Bi_2Te_3 substrate leading to a p-doped adlayer as assumed by the investigation of the Fermi contours in fig. 3.12. It is worth mentioning that the shift is comparable to the one of the FeSe thin films on Bi_2Se_3 which amounts to 360 meV (section 3.2.3).

Since the next section of this chapter deals with alkali doping of FeTe thin films

grown on Bi₂Te₃ it is worth summarizing the important conclusions of section 3.3 and 3.4 so far. The autocorrelation image of Rb atoms distributed on bulk Fe_{1.08}Te indicates an electron transfer from Rb to bulk Fe_{1.08}Te, suggesting a similar behavior for the case of Rb on FeTe thin films. The complicated Fermi surface of the thin film can be viewed as a superposition of three rotational domains of bulk Fe_{1.08}Te and underlines hereby the 3D character of the thin films. Moreover, the Bi₂Te₃ surface covered with FeTe is strongly n-doped suggesting a net charge transfer from the FeTe adlayer to the substrate.

3.4.4 Electronic Structure of Alkali Doped FeTe Thin Films on Bi₂Te₃

Lastly, the electronic structure of purposely doped FeTe thin films is studied. The alkali doping of the FeTe thin film was carried out with resistance heating of a (SAES) Rb dispenser directly aligned with the sample in the MC manipulator of the SGM3 endstation. The sample was maintained at a temperature of 90 K during the Rb deposition and data acquisition. The alkali coverage was determined by the ratio of Rb/Te core level photoemission intensities.

Fig. 3.14 gives an overview of the electronic structure of FeTe on Bi₂Te₃ for a Rb coverage of 0-10%. Counterintuitively, both the integrated intensity in a 120 meV range around the Fermi energy (fig. 3.14(a)-(c)) and the high symmetry cut in the $\bar{M}\bar{\Gamma}_1\bar{M}_1$ directions (fig. 3.14(d)-(f)) does not show any recognizable change upon doping, even for a Rb atom concentration of $\sim 10\%$ on the surface.

As shown in fig. 3.10 alkali atoms such as Rb exhibit a strong ionic character and are commonly exploited for manipulating the work function of materials or, as used here, for surface doping¹⁰⁵. Therefore, it is rather unexpected that Rb deposition on FeTe thin films does not induce a visible doping effect. However, this behavior can be explained by DFT calculations which yields a density of states (DOS) at the Fermi level of around 5 eV^{-1} per unit cell equivalent to 2.5 eV^{-1} per Fe atom. An electron doping of 0.1 electron per Fe atom results, with such a DOS, in a rigid band shift of only 40 meV as seen in fig. 3.14(g). Furthermore, fig. 3.14(g) shows that for the predicted undoped (red) and heavily doped (purple) band structure no evident change is expected therefore the Fermi surfaces also remain similar.

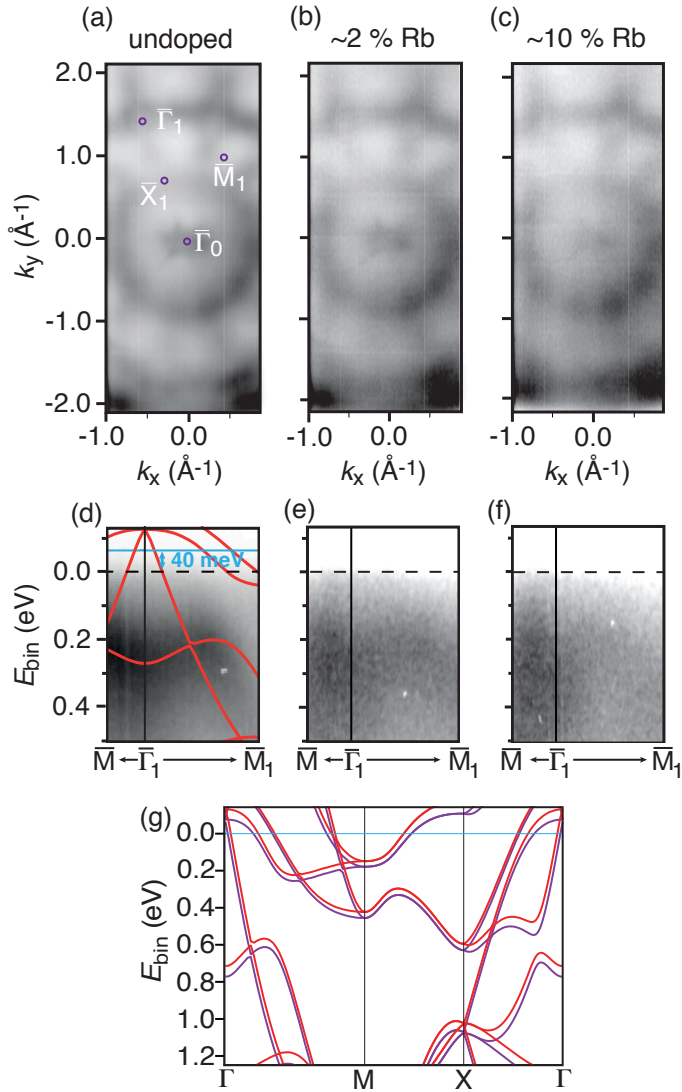


Figure 3.14: Doping behavior of FeTe thin films for different coverages of Rb atoms acquired at a photon energy of 65 eV and at a temperature of 90 K. Photoemission intensity of FeTe thin films integrated in a 120 meV range around the Fermi energy of (a) the undoped, (b) ~2% and (c) ~10% Rb doped thin films. High symmetry cuts for (d) the undoped, (e) ~2% and (f) ~10% Rb doped thin films. The red solid line indicates first principles calculations for bulk FeTe (Γ -M-X plane) and the light blue line indicates the Fermi level of the first principle calculation. The dashed black horizontal lines indicate the experimental Fermi level. (g) Calculated band structures for undoped (red) and doped (purple; 0.1 electron per Fe atom) FeTe.

3.5 Conclusion Iron Chalcogenides

In summary chapter 3 provides an opportunity to compare and contrast the crystal and electronic structure of the ICs, FeSe and FeTe, in the proximity of the 2D limit. The similar synthesis methods of FeSe and FeTe on respective topological insulators Bi₂Se₃ and Bi₂Te₃, result in both cases, to multilayer films embedded in the substrate in three rotational domains. Photoemission features which can be assigned to multilayer FeSe film and bulk FeTe show the materials' 3D character already at a few MLs. A net charge transfer from the FeTe adlayer to the substrate is indirectly observed by a shift in the band structure of the substrate upon formation of the thin film.

Despite the similarities, FeSe and FeTe also exhibit striking differences in terms of their electronic properties, which can be helpful to understand with regards to the underlying process of iron based unconventional superconductivity. Bulk FeSe exhibits a superconducting transition temperature of 8 K which can be impressively raised to over 100 K by synthesizing ML FeSe on SrTiO₃^{22,56}. However for the presented case FeSe thin films on Bi₂Se₃ show, surprisingly, no sign of a superconducting gap at 5 K, a temperature even lower than the reported T_C for bulk. On the other hand, it has to be noted that a limited quantity of $y = 0.03$ excess Fe in between the van der Waals gaps of this layered material results already in a suppression of the superconductive state⁶⁹⁻⁷¹. Thus a direct comparison of critical temperatures in these materials without a clear indication of the excess Fe has to be taken with a grain of salt. The cousin system FeTe instead, while showing no superconductivity in the bulk form, exhibits in the thin film limit a superconducting gap corresponding to a T_C of 6 K and coexisting with a bi-collinear antiferromagnetic order⁶¹. Strong electronic correlated effects in FeTe presumably lead to very broad bands while for FeSe the electronic structure is better defined. A complete understanding of the properties which lead to unconventional superconductivity remain an unsettled period.

Chapter 4. Single Layer $V_{1+x}S_2$ on Au(111)

The following chapter is dedicated to the synthesis methods employed for SL $V_{1+x}S_2$ on Au(111). STM and LEED measurements reveal two distinct phase transitions of the as-grown sample upon annealing in UHV. The crystal structure of all three phases is determined by a study that combines several methods of structural analysis. Finally, the electronic structure of the three phases is discussed. In the following the group of TMDCs is briefly discussed and as well the structure and properties of $V_{1+x}S_2$ are presented.

4.1 Introduction

4.1.1 Bulk and Two-Dimensional Transition Metal Dichalcogenides

The research on bulk TMDCs can be dated back to the 1960s¹¹⁵ and was reinitialized by the discovery of graphene through mechanical exfoliation in 2004¹⁵. The history of TMDCs and an overview about current research can be found in Ref.¹¹⁶. The chemical formula of TMDCs is MX_2 , where M labels the transition metal and X the chalcogen. Solely 40 of the 100 existing bulk TMDCs are layered and constructed in a sandwich-like manner that consists of a mid-layer of a transition metal (M) surrounded by one top and one bottom layer of chalcogens (X) (fig. 4.1 inset). In this configuration each chalcogen uses two electrons from one transition metal to fill the bonding state, a situation which results in a change of the oxidation state to +4 for the transition metal and to -2 for the chalcogen atom. The lone pair of X and the absence of dangling bonds on the surface makes each layer chemically inert and

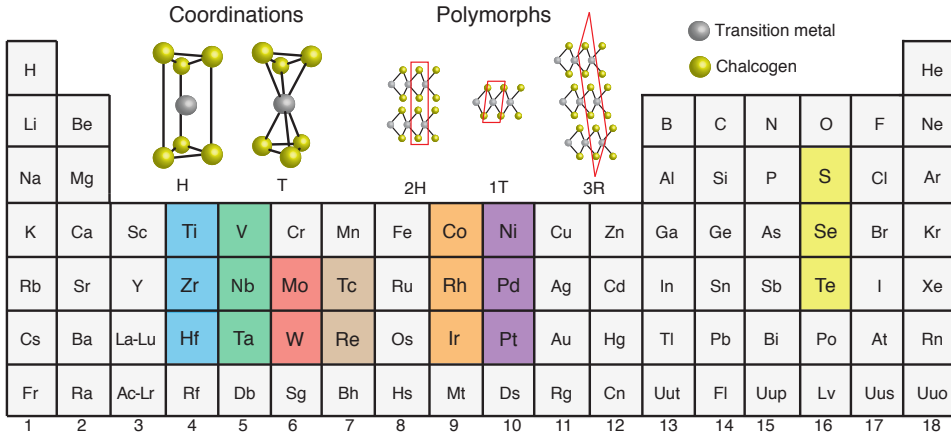


Figure 4.1: Periodic table: Chalcogens (yellow) and transition metals (other colors) forming layered TMDCs are highlighted. The inset shows the trigonal prismatic (H) and octahedral (T) coordination for TMDCs, together with the three most common polymorphs. Unit cells are marked by red lines. Adapted from Ref.¹¹⁶ and modified.

explains the nature of the layered structure: by contrast to the covalently bonded M-X intralayers, only weak van der Waals forces between the MX_2 - MX_2 layers are present and allow them easy to cleave, similar to graphene.

Bulk TMDCs show a variety of crystal morphologies caused by two possible coordinations of the transition metal M inside the sandwich structure as by different stacking orders of the MX_2 layers. One can distinguish between trigonal prismatic (H) or octahedral (T) coordination, and between the three most common polymorphs 1T, 2H (AB stacking) and 3R (ABC stacking)¹, as shown in fig. 4.1. Depending on the atomic composition (*i.e.*, the identities of the transition metal and the chalcogen atom), the electronic properties can vary significantly. While the majority of the layered TMDCs are semiconductors (groups 4, 6, 7, 9, 10), group 5 TMDCs are metallic. Intriguing physical phenomena such as metal-semiconductor transitions, superconductivity and charge-density waves were observed in this material system in bulk^{115–117}.

By contrast to the bulk parent compounds, SL TMDCs develop interesting additional properties. For example, WS_2 and MoS_2 exhibit an indirect-to-direct bandgap transition^{1–3}. Among the variety of monolayer TMDCs, SL VS_2 has attracted interest due to its theoretically predicted intrinsic magnetism and strong dependence

¹The number indicates the MX_2 layers within a unit cell.

of the magnetic state on the crystal structure^{118–125}. Controllable magnetism in 2D materials would be especially valuable for spintronics application and data storage systems.

4.1.2 Crystal and Electronic Structure of $V_{1+x}S_2$

Due to the thermodynamic metastability of stoichiometric bulk $V_{1+x}S_2$ ($x = 0$), the synthesis is rather challenging and the material system remains little studied^{126, 127}. However, previous studies have shown that octahedrally coordinated (1T) VS_2 can be synthesized by Li deintercalation of stoichiometric $LiVS_2$ ^{126, 128}. The VS_2 prepared with this method is in a metastable state which becomes S-depleted beyond 300°C and is therefore referred as $V_{1+x}S_2$. Due to the S depletion, interstitial V atoms are forming in between the van der Waals gaps of the layered 1T- $V_{1+x}S_2$ system driving a slight increase in lattice constant from 3.217 Å to 3.2703 Å for $x = 0$ to 0.172^{126, 127}. Moreover, at $x = 0.25$ the ordering of the interstitial V forces a phase transition from the octahedral coordination to monoclinic V_5S_8 (*i.e.* $V_{1.25}S_2$) as seen fig. 4.2¹²⁹. The figure also shows all other known compounds of $V_{1+x}S_2$. Previous studies show that bulk 1T- $V_{1+x}S_2$ can also be synthesized by high pressure S synthesis and that the x content influences such physical properties as electrical conduction and CDW¹²⁷.

A number of SL TMDCs, including MoS_2 , WS_2 and TaS_2 have been already synthesized as 2D materials and intriguing changes have been observed in the electronic properties compared to the bulk parent compound^{1–3}. In the case of bulk 1T- $V_{1+x}S_2$ the change in the lattice constant upon S depletion suggests a possible way to presumably modify the predicted magnetic moment in the SL through controlling the crystal structure^{121–125}. A precise and controllable magnetism in 2D materials would be especially valuable for potential applications such as high-performance functional nanomaterials¹¹⁸. However, in line with the synthesis of bulk VS_2 the growth of SL VS_2 is rather challenging and could not be realized until today.

The difficulties in the synthesis of the predicted 2D magnet VS_2 might be also partly attributable to the Mermin-Wagner theorem. This theorem prohibits long range magnetic order in 1D and 2D systems since strong thermal fluctuations destroy 2D ferromagnetism¹³⁰. Intrinsic magnetism in 2D materials could be realized neither in graphene nor in any synthesized SL TMDC so far. However, the latest discovery by Huang et al. and Gong et al. shows that magnetic anisotropy in 2D materials can lift the Mermin-Wagner restriction and introduce intrinsic long-range ferromagnetic order in 2D systems^{131, 132}.

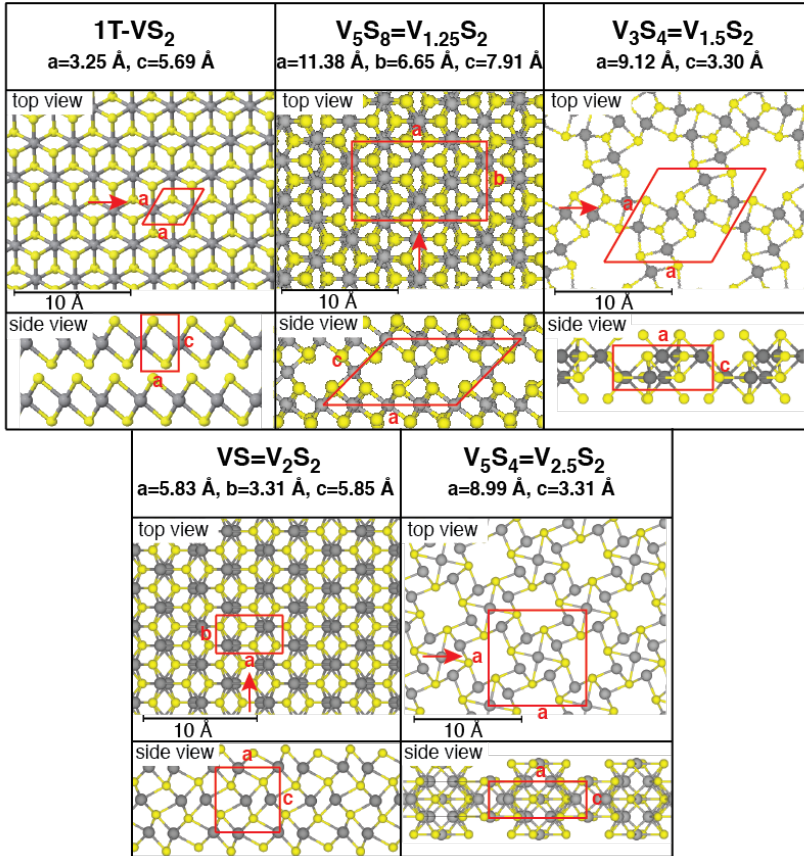


Figure 4.2: Top and side views of the crystal structures of all known stable bulk $V_{1+x}S_2$ compounds. The chemical compositions and the lattice constants are indicated in each panel. Yellow balls indicate S atoms and grey balls V atoms, respectively. Unit cells are marked by red lines; red arrows mark the points of view for the side view images. The structural information of the bulk $V_{1+x}S_2$ compounds are obtained by Ref.¹³³.

Fig. 4.3(a) and (b) show the predicted Fermi surfaces of SL 1H- and 1T- VS_2 for the non-spin polarized cases. The Fermi contour for the 1H case in fig. 4.3(a) consists of two hole pockets located at $\bar{\Gamma}$ and \bar{K}^2 . The former exhibits a hexagonal shaped feature at the center of the BZ, and the latter a roundish triangle at the BZ corner. The overall appearance is very similar to the Fermi contour previously obtained for SL 1H-TaS₂ on Au(111)². For the predicted 1T configuration in fig. 4.3(b), the Fermi contour consists of a flower-like electron pocket with six elongated petals centered at the \bar{M} points. While both of the predicted band structures exhibit a metallic character, the actual Fermi contour is rather different and can be directly assigned to the corresponding structural configuration.

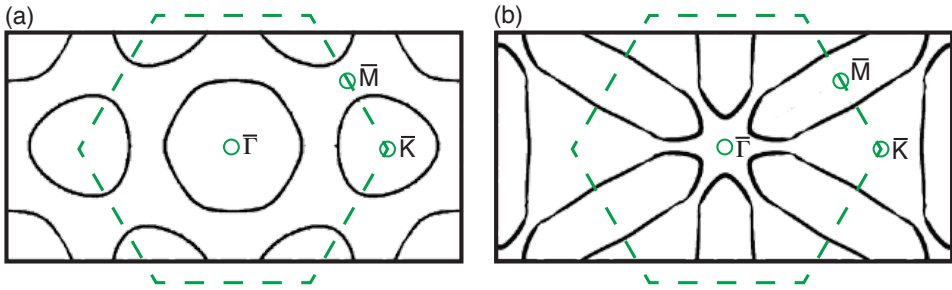


Figure 4.3: Predicted Fermi surface of stoichiometric SL VS_2 for the non-spin polarized case for (a) 1H and (b) 1T configuration. The black lines correspond to DFT-calculation, the green dashed lines indicate the hexagonal BZ of SL VS_2 and the green small circles mark the positions of the high symmetry points. Adapted and modified from Ref.¹²⁴.

4.2 Synthesis of Single Layer $V_{1+x}S_2$ on Au(111)

Similarly to graphene, the first experiments on thin film TMDCs were performed on mechanically exfoliated samples, which are easily produced by the scotch tape method^{134–137}. This technique leads to high quality thin film TMDC flakes with varying atomic layers and random distribution on the substrate. These sample are suitable for local measurement techniques as STM and transport measurements, where the focus lies in one flake with a defined orientation and thickness. In Micro-ARPES the spot size of the beam is small enough to obtain the electronic structure from only

²In Ref.¹²⁴ this is solely stated but not explicitly shown by band structure dispersions.

one domain flake¹³⁸. However, in traditional ARPES, as used at the SGM3 beamline, the photoemission signal is averaged over the whole beam spot ($200\ \mu\text{m} \times 50\ \mu\text{m}$, in our case) which results in an incoherent superposition of contributions to photoemission intensity from multiply oriented domains making it impossible to disentangle the measured band structure of exfoliated TMDCs. In the following, the SL samples are referred as $V_{1+x}S_2$ as we cannot exclude the formation of interstitial V in between the substrate and the adlayer, similar to what is observed in the bulk parent compound.

In order to synthesize SL $V_{1+x}S_2$ which is usable for ARPES, a well established epitaxial growth method is adapted which has successfully synthesized TMDC nanoislands for past studies of related materials systems¹³⁹ and can be modified for synthesizing various high quality SL semiconducting and metallic TMDCs^{1-3,7}. These growth procedures are based on the evaporation of a transition metal in a sulfur rich atmosphere on a clean Au(111) surface that shows a regular herringbone reconstruction.

Before the growth of SL $V_{1+x}S_2$, the surface of the Au(111) was treated by standard UHV cleaning which includes several cycles of Ne^+ ion sputtering and annealing up to 700°C until the Au(111) surface exhibits the regular herringbone reconstruction. During the deposition of V with an electron beam evaporator the Au(111) crystal was held at room temperature in UHV conditions. Subsequently, the substrate was located ca. 1 mm away from the home-build H_2S nozzle and the chamber was backfilled to an H_2S pressure of 8.5×10^{-5} to 1.2×10^{-4} mbar at a sample temperature of 400°C ³. It was observed that through further annealing in UHV two phase transitions of $V_{1+x}S_2$ were introduced at 450°C and 550°C (detailed discussion in section 4.3 and 4.4). For the sake of simplicity, the as grown crystalline phase is called phase I, the 450°C annealed phase is called phase II and the high temperature phase is called phase III.

The SGM3 endstation (for LEED and ARPES) is not equipped for performing all necessary structural characterization techniques to obtain a full picture of the crystal morphology of SL $V_{1+x}S_2$; therefore, complementary investigations were performed in a dedicated STM-chamber (described in section 2.2.3; for STM) and at the SuperESCA beamline at Elettra Sincrotrone Trieste (for XPD and XPS). Since the samples are air sensitive, we prepared them in situ in each measurement chamber. Therefore, SL $V_{1+x}S_2$ on Au(111) was synthesized with modified growth methods directly at each measurement setup: in the case of the STM-chamber the general synthesis procedure was the same as described above, but due to safety reasons H_2S

³The synthesis of $V_{1+x}S_2$ requires a high local H_2S pressure on the sample surface, as explained more in detail in section 4.3.

was substituted with the less toxic sulfur precursor DMDS. DMDS was introduced in the chamber via leak valve until a background pressure of 1.2×10^{-6} mbar was obtained⁴. The lower S background pressure and lifting of the requirement for high local pressure during the growth are presumably attributable to stronger interaction of the DMDS with the substrate¹⁴⁰; furthermore, DMDS provides two S atoms per molecule instead of only one as in the case of H_2S . It is worth mentioning that the different growth conditions do not change the basic properties of the material⁴¹. For SuperESCA a synthesis technique was used in which H_2S gas was dosed through a hot V-filament directly onto the surface of the sample at elevated temperature. Studies on SL TaS_2 on Au(111) for this growth method indicate the formation of larger size domains which are preferred single orientated².

Unless otherwise stated, STM measurements were performed in the dedicated STM-chamber in the SGM3 lab with an Aarhus-style STM at room temperature⁴³. The ARPES and LEED datasets were acquired at the SGM3 endstation at 35 K¹⁰⁴. XPS and XPD data were acquired at the SuperESCA beamline of the Elettra synchrotron radiation facility in Trieste (Italy) at room temperature¹⁴¹.

4.3 Structural Analysis of Single Layer $V_{1+x}S_2$ on Au(111)

4.3.1 Three Phases: Characterization with STM and LEED

Structural Characterization with STM

STM measurements reveal three distinct crystalline phases, which are shown in fig. 4.4. Phase I in fig. 4.4(a) forms well-separated up-pointing and down-pointing triangle islands which exhibit the typical hexagonal moiré structure observed on SL TMDCs grown on Au(111)^{1-3,7}. The intensity modulation of the moiré pattern is even better observable in the atomically resolved STM image in the red inset of fig. 4.4(a), which furthermore reveals the hexagonal surface lattice of phase I. Moreover, similar triangular island shapes have been observed in previous studies on metallic SL TaS_2 synthesized with the evaporator, while semiconducting SL WS_2 and MoS_2 on Au(111)

⁴In this work only STM results from the evaporator-DMDS growth method are shown, unless otherwise stated.

exhibit polygons for larger islands sizes^{1-3,7}. The STM results presented here are in line with previous STM studies of SL TMDCs on Au(111); however, considering the metastability of the bulk parent compound, one cannot on the basis of STM alone exclude the possibility that the islands might be a different $V_{1+x}S_2$ compound that forms similar triangularly shaped islands with a hexagonal moiré. Note that STM cannot necessarily distinguish between different polymorphs of materials if the surface structure is similar, as solely the top S atoms are imaged. This problem can be seen in the case of the tetragonal (1H) and octahedral (1T) coordinations for TMDCs.

Small bright irregularly shaped areas on top on the surface of phase I are visible, which might be ascribable to accumulated residual V from the $V_{1+x}S_2$ SL synthesis. It is worth mentioning that the sample's surface is rather "dirty" by the presence of adsorbates accumulated during the growth process, and these adsorbates are not removed until the sample is post-annealed (which also leads to the formation of phase II).

Upon annealing in UHV to 400°C a transition from phase I to phase II is induced. The STM image in fig. 4.4(b) shows coexisting phase I and phase II domains obtained by annealing precisely to the transition temperature. Both phases exhibit a hexagonal moiré superstructure. Phase I already shows a slightly deformed moiré pattern with clear observable dislocation lines, presumably due to the initiation of the phase change. Furthermore, the well separated triangles seen in fig. 4.4(a) are now fused together into larger islands, indicating mobility of the $V_{1+x}S_2$ islands at elevated temperature. Even though phase II exhibits a hexagonal moiré pattern, one can clearly distinguish the two moiré patterns which are separated by an irregularly shaped domain boundary marked by black arrows. Note that a tip effect which might create similar looking moiré structures can be excluded as both phases appear in the same STM line scan.

Fig. 4.4(c) shows the full transition to phase II after annealing to 450°C in UHV. Phase II exhibits a hexagonal moiré superstructure, similar to phase I. A well ordered hexagonal moiré pattern is the result of the superposition of two hexagonal surface lattices with a small lattice mismatch, indicating a hexagonal surface lattice in the case of phase II even without atomically resolved STM images. Furthermore, the well separated triangles of fig. 4.4(a) are now fused into larger uniform islands without visible domain boundaries. The formation of domain boundaries occurs if oppositely oriented TMDC islands collide during the growth/annealing process, so their absence suggests a single-domain formation for phase II, at least within the large island area⁷.

Annealing in UHV to 500°C leads to the transition to a third phase, whose signature is a striped superstructure. This so-called phase III is visible coexisting with

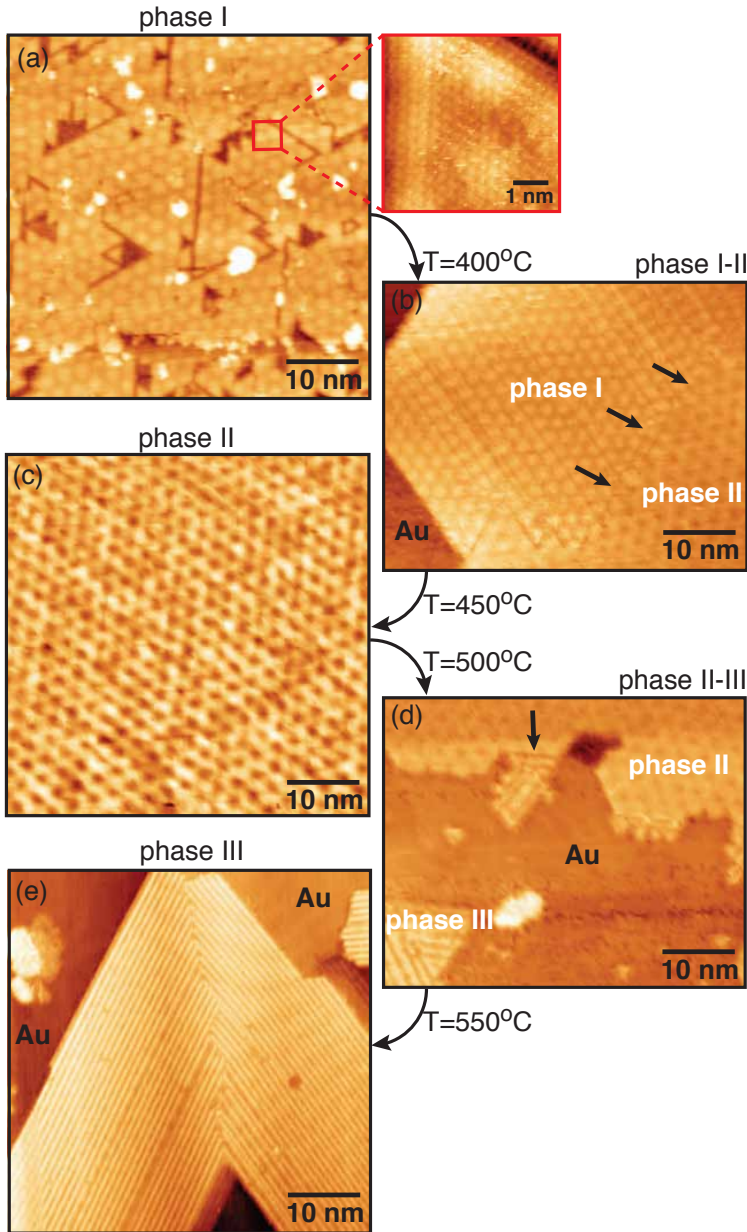


Figure 4.4: Evolution of the crystal morphology of $V_{1+x}S_2$ on Au(111) by annealing UHV. The different phases of $V_{1+x}S_2$ and the respective transition temperatures are indicated in the panels. STM images acquired at room temperature of (a) phase I, (b) intermediate phase I-II, (c) phase II, (d) intermediate phase II-III and (e) phase III. The red inset shows the atomic resolution image for phase I. The black arrows mark the grain boundaries between adjacent phases. Tunneling parameters: (a) $V_s = 825$ mV, $I_t = 0.30$ nA; inset of (a) $V_s = 300$ mV $I_t = 1.26$ nA; (b) $V_s = -656$ mV, $I_t = -0.26$ nA; (c) $V_s = -656$ mV, $I_t = -0.33$ nA; (d) $V_s = -565$ mV, $I_t = -0.48$ nA; (e) $V_s = 1117$ mV, $I_t = 0.32$ nA.

phase II in fig. 4.4(d). In the upper part of the STM image, the hexagonal moiré pattern of phase II is visible without any observable deformation; meanwhile, a triangular island with the striped structure appears in the bottom left corner of the image, and a similar striped domain is attached directly to the phase II island, with a sharp domain boundary (marked by a black arrow).

The full transition to phase III is completed after annealing to 550°C, and is shown in fig. 4.4(e). The typical linear stripe structure of phase III is rotated in three domains by 0, 120° and 240° with respect to each other. The surface crystal structure can be revealed by atomically resolved STM, as in the image acquired by the group of Prof. Alexander Khajetoorians (Radboud University) at 5K shown in fig. 4.5⁵. The overview image in fig. 4.5(a) shows the characteristic linear stripe structure for phase III in three rotational domains together with the herringbone reconstruction of the clean Au(111) substrate. At closer inspection, triangular loop-like distortions prevent the herringbone reconstruction to propagate underneath the phase III SL, suggesting a lifting of the native Au(111) surface reconstruction underneath the islands. Fig. 4.5(b) shows an atomically resolved STM image of a phase III island with the rectangular surface unit cell visualized by red lines. The lattice constants of the rectangular unit cell can be determined by STM to be 9.1(0.1) Å and 3.4(0.1) Å, values which are not in agreement with any $V_{1+x}S_2$ bulk compound of which we are aware (fig. 4.2). Furthermore, the height profile reveals that the stripe structure does not stem from a moiré superstructure but originates from an up-down modulation of the top S atoms as seen in fig. 4.5(c). A similar modulation of the top S can be also observed in distorted 1T-MX₂, *i.e.* 1T'-MX₂. In that case, the hexagonal $a \times a$ unit cell is distorted to a $\sqrt{3}a \times a$ rectangular unit cell by the formation of one-dimensional zigzag chains of the M atoms^{116,142}. However, in the case of the distorted 1T' configuration reported in the literature the ratio of the lateral lattice parameters is around 1.7, while for phase III the ratio is calculated to 2.7. This fact excludes the previously reported 1T' configuration as a possible crystal structure for our system. Neither any $V_{1+x}S_2$ compound of which we are aware nor any MX₂ distorted structures can explain the unconventional lattice formation of phase III, suggesting a new crystal structure presumably exclusively synthesizable in the 2D-limit.

Fig. 4.5(e) shows a corresponding STM image of phase III acquired with different scanning parameters than those of fig. 4.5(b). Instead of the atomic structure, a new pattern consisting of a three cigar-like shaped features (marked by black rectan-

⁵The $V_{1+x}S_2$ sample was synthesized with the H₂S-evaporator method at the SGM3 endstation and sent in a vacuum suitcase to Radboud University.

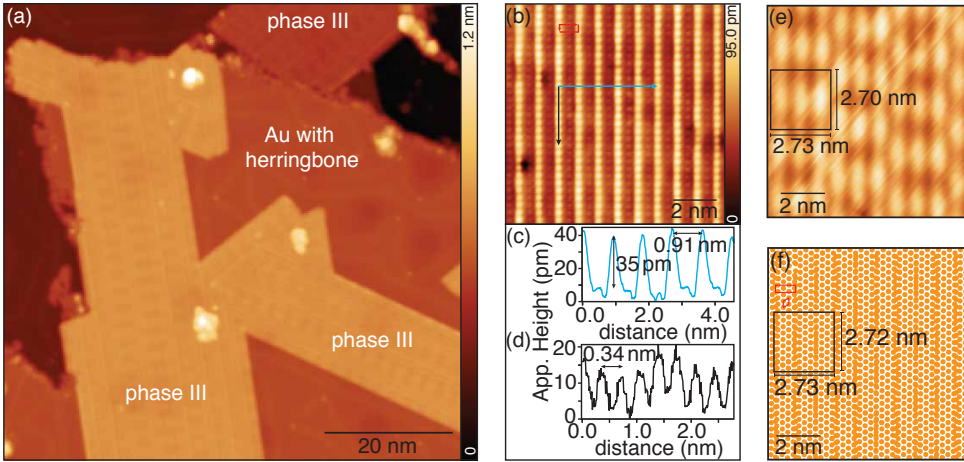


Figure 4.5: STM images of phase III acquired at 5 K by the group of Prof. Alexander Khajetoorians (Radboud University). (a) Typical overview STM image of sub-monolayer coverage for phase III on Au(111) shows the three rotational domains of phase III and the herringbone reconstruction of the substrate (marked in the figure). Tunneling parameters: $V_s = 800$ mV, $I_t = 50$ pA. (b) Atomic resolved STM image reveals the rectangular unit cell (red lines) of phase III. Tunneling parameters: $V_s = 3$ mV, $I_t = 3$ nA. (c) and (d) Apparent height profiles along the blue and black arrows in (b), respectively. (e) Corresponding STM image to (b) but acquired with different scanning parameters ($V_s = -800$ mV, $I_t = 3$ nA), revealing a moiré superstructure. The black rectangle marks three cigar-like shapes which generate the superstructure pattern. (f) Simple ball model to simulate the superstructure seen in (e). The rectangular unit cell of phase III is superimposed on the hexagonal Au(111) surface lattice. The red lines mark the unit cells of phase III and Au(111), respectively. The black rectangle marks three cigar-like shapes which generate the moiré pattern seen in (e).

gle) is observable. The supercell is identified as a superstructure with a periodicity of $2.73 \text{ nm} \times 2.70 \text{ nm}$. The experimental pattern can be simulated by a simple ball model superimposing the phase III rectangular lattice on the hexagonal Au(111) surface lattice as shown fig. 4.5(f). The theoretical periodicity of the superstructure is determined to be $2.73 \text{ nm} \times 2.72 \text{ nm}$ and well in agreement with the experimental data.

Structural Characterization with LEED

The STM results from the three crystalline phases are corroborated by LEED investigations shown in fig. 4.6. We note that the data shown in fig. 4.6 were all acquired from samples with partial monolayer coverage (around 0.7 ML), with considerable clean Au(111) exposed in between the single layer islands. In order to identify the diffraction spots originating from Au(111) and $V_{1+x}S_2$ the reciprocal lattice vectors are visualized by yellow and differently colored arrows in fig. 4.6, respectively.

The LEED pattern of phase I (fig. 4.6(a)) exhibits sharp diffraction spots accompanied by moiré satellite spots with strong intensity indicating a well crystallized ordering of the whole sample. Note that for the kinetic energy used here the moiré spots, even those of higher orders, are significantly stronger in intensity than the rather weak phase I main spots. The reasons for this are not entirely clear, but LEED intensity is a complex quantity involving multiple-scattering¹⁴³, and complex scattering events can affect the spot intensity in non-trivial ways. The moiré periodicity and atomic lattice constant obtained for phase I by LEED is $25.24(0.67) \text{ \AA}$ and $3.248(0.023) \text{ \AA}$, respectively, which is in agreement with the experimental values for the octahedral (1T) polymorph of bulk crystalline VS_2 ^{126,127} and does not match with any other $V_{1+x}S_2$ compound of which we are aware in the literature (fig. 4.2). Even if neither STM nor LEED can distinguish between the 1H and 1T, the combined results point to a possible 1T or 1H configuration for phase I. Note that bulk VS_2 is synthesized exclusively in the octahedral (1T) configuration^{126,127} and therefore a 1T configuration might be also expected in SL films. However, SL TaS_2 on Au(111) grows in the trigonal prismatic coordination whereas the bulk parent compound is synthesized in the octahedral coordination^{2,144}. An analogue 1T to 1H transformation cannot be excluded for $V_{1+x}S_2$. Furthermore, the simultaneous imaging of the Au(111) and phase I diffraction spots reveals that the hexagonal surface lattice of the substrate is well aligned with the hexagonal lattice of the adlayer. Three very weak diffraction lines which are marked by black arrows in fig. 4.6(a) are visible at closer inspection. The weaker diffraction lines can be presumably ascribed to domain

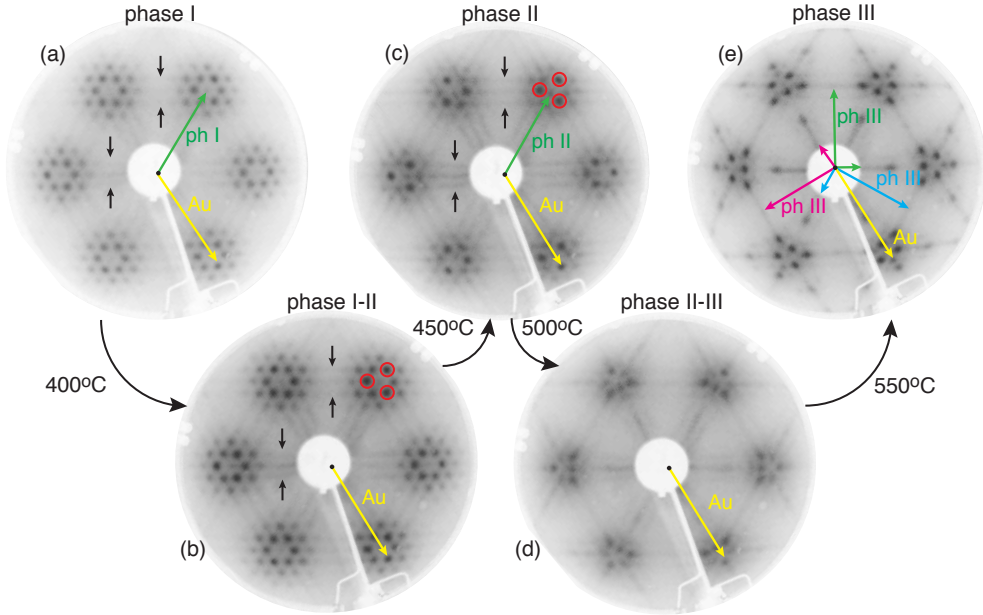


Figure 4.6: Evolution of the crystal morphology of SL $V_{1+x}S_2$ on Au(111) by annealing in UHV. The different phases of $V_{1+x}S_2$ and the respective transition temperatures are indicated in the panels. LEED images acquired with a kinetic energy of 92.8 eV at 35 K of (a) phase I, (b) intermediate phase I-II, (c) phase II, (d) intermediate phase II-III and (e) phase III. The black arrows mark weaker diffraction lines, the red circles diffraction spots of enhanced intensity. For phase I (ph I) and phase II (ph II) the reciprocal lattice vectors of the hexagonal surface lattice for Au(111) and $V_{1+x}S_2$ are indicated by yellow and green arrows, respectively. For phase III (ph III) the rectangular reciprocal unit cell vectors for the three orientations are marked by green, blue and pink arrows, respectively.

boundaries or dislocation boundaries oriented perpendicular to the diffraction lines.

Annealing in UHV to 400°C leads to the transition from phase I to phase II. The simultaneous existence of phase I and II results in a diffraction pattern which contains contributions from both phases as seen in fig. 4.6(b). Besides the moiré pattern of phase I, three additional spots with an enhanced intensity are arranged around each main $V_{1+x}S_2$ diffraction spot (marked with red circles). Furthermore, the above-mentioned three diffraction lines are enhanced in intensity, suggesting an increase of possible domain boundaries or dislocation boundaries on the sample (diffraction lines are marked with black arrows in the LEED panel).

Annealing to 450°C results in the full transition to phase II as seen in fig. 4.6(c).

The signature of the LEED for phase II is hexagonally arranged weak main spots (marked with green arrow) each accompanied by three strongly enhanced (marked by red circles) and three rather suppressed first order moiré spots. It is surprising that three spots of the moiré pattern are very enhanced in intensity, while the remaining moiré and the main diffraction spots are marginal. Indeed, one could argue that the three enhanced diffraction spots are the actual main spots surrounded by weaker moiré satellites. A similar LEED pattern could presumably be constructed with, for example, three distorted and slightly rotated hexagonal domains. However, we find strong indications that the three enhanced spots are a result from moiré satellites: A small distortion or rotation of the hexagonal adlayer with respect to the substrate should result in a visible change in the hexagonal moiré pattern, similar to what has been previously observed with STM in the case for graphene grown on different substrates^{145,146}. The observed moiré pattern in STM for phase II (fig. 4.4(c)), however, exhibits a well defined hexagonal moiré without distortions or variations in the moiré periodicity, suggesting an undistorted and well aligned adlayer on the substrate. Furthermore, the LEED spots of the Au(111) substrate are coincident with one of the enhanced diffraction spots which is a typical signature of a moiré satellite spot (fig. 4.6(c)).

The moiré periodicity and atomic lattice constant obtained for phase II by LEED are $23.60(0.52)$ Å and $3.332(0.035)$ Å, respectively; this atomic lattice constant is comparable with the experimental lattice parameter of the octahedral (1T) polymorph of bulk VS_2 ^{126,127}. With respect to phase I the lattice constant slightly increases by around 0.08 Å upon the transition to phase II. A similar phenomenon was observed previously in bulk 1T- $V_{1+x}S_2$, where the loss of S and the formation of interstitial V in the van der Waals gaps between the sandwich layers is accompanied by a small increase in the lattice constant^{126,127}. A similar process might also occur during the annealing of the SL: at elevated temperature S presumably desorbs from the material and leads to the formation of interstitial V between the Au(111) substrate and the adlayer, leading to a small increase of the lattice constant. Moreover, the three diffraction lines are still observable and stronger in intensity compared to phase I, suggesting that the possible domain boundaries or dislocation boundaries are more pronounced in phase II (marked with black arrows in LEED panel).

Annealing in UHV to 500°C leads to the transition from phase II to phase III. As seen in fig. 4.6(d) the coexistence of the two phases results in an overall blurry diffraction pattern. While the three intense moiré spots are still visible, they appear washed out and weaker in intensity, and the low intensity moiré spots vanish in the

background. Although the observed STM image in fig. 4.4(d) exhibits already clear stripe features, contributions from phase III in the LEED are not clearly observable, probably as a result of disorder within the structure.

The complete transition to phase III is seen after annealing in UHV to 550°C (fig. 4.6(e)). The LEED data for phase III exhibit a rather complicated diffraction pattern which at first resembles a hexagonal reciprocal lattice with Christmas-tree-like moiré satellite spots. However, this interpretation is not correct, as the STM data exhibit a $9.1 \text{ \AA} \times 3.4 \text{ \AA}$ rectangular unit cell grown in three rotational domains on Au(111). Taking into account the rectangular symmetry of the superstructure and the lattice constant for phase III obtained by STM, the LEED pattern for phase III can be constructed: fig. 4.7(a) shows the LEED pattern of phase III acquired at the same conditions as in fig. 4.6(e) superimposed with the reciprocal lattice vectors of the three rotational domains marked by green, blue and pink arrows, respectively. In the next step the rectangular reciprocal lattices of the three rotational domains (blue, pink and green lines) are constructed and the diffraction spots expected from STM for phase III, along with the spots for Au(111) obtained from LEED, are marked with the correspondingly colored circles as shown in fig. 4.7(b). In fig. 4.7(c), the reciprocal lattice grid of fig. 4.7(b) is removed and each diffraction spot can be assigned to the corresponding domains. We have an overall good agreement between the experimental LEED pattern and the constructed diffraction spots. The diffraction spots can now be assigned to the corresponding rotational domains and the lattice constants for phase III can be determined to $9.108(0.031) \text{ \AA}$ and $3.278(0.025) \text{ \AA}$, which is in agreement with the STM measurements.

A possible explanation for the drastic change in crystal morphology from phase II to phase III is found in previous results concerning bulk $V_{1+x}S_2$: As already mentioned above, Ref.¹²⁶ and Ref.¹²⁷ show that desulfidation upon annealing of bulk 1T-VS₂ is accompanied by a slight increase of the lattice parameters. A total S depletion of around 20% (equivalent to $x = 0.25$) leads further to the ordering of interstitial V which induces a transition from the octahedral 1T coordination to the monoclinic V_5S_8 (fig. 4.2). In the case of the SL a more elevated temperature might result in a further S desorption until the hexagonal lattice configuration cannot be retained and a second phase change is introduced, although not necessarily that which is seen in the bulk. If we would assume that phase I is stoichiometric VS₂, then a topographic image similar to that in fig. 4.5(b) is obtained, if around 50% of the top S have to desorb compared to the hypothetical SL 1T-VS₂. If, further, we assume that the majority of S loss during annealing is from the non-interfacial (top) S layer

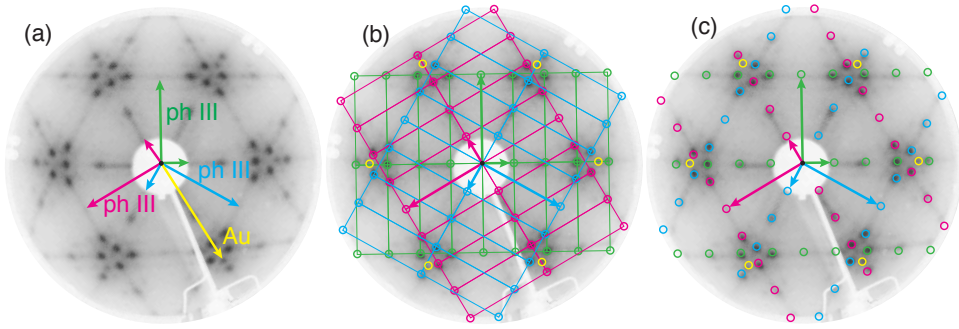


Figure 4.7: Explanation of the LEED pattern of phase III acquired at a kinetic energy of 92.8 eV and at a temperature of 35 K. (a) Same LEED image as in fig. 4.6(e). Green, blue and pink arrows indicate the reciprocal lattice vectors of the three rotational domains, and the yellow arrow the reciprocal surface lattice vector of Au(111). (b) The colored rectangles indicate the reciprocal unit cells of the three rotational domains, with the colors corresponding to those in panel (a). The diameter of the colored reciprocal unit cells are based on STM data. The colored circles show the predicted LEED spots for each domain and for the Au(111) substrate. (c) Identical to panel (b), but with the schematics of the rectangular reciprocal unit cells removed, to show more clearly the good agreement between the calculated and observed spots.

– implying that the underlying V and S layers remain more or less intact – then one can estimate the lower limit of the total S lost from 1T-VS₂ to phase III to around 25%, which is comparable to the bulk 1T-V_{1+x}S₂ transition threshold of 20%.

The experimental results point to the possibility that the phase transformations are caused by desulfidation upon annealing. A direct way to address the S loss in our experimental setup is not possible. However, an indirect way to demonstrate the effect of S on SL V_{1+x}S₂ is to anneal the supposedly most deficient S phase III in H₂S atmosphere in order to reverse the phase transformation. As each phase of V_{1+x}S₂ can fast and clearly be assigned by the diffraction pattern, LEED is used to obtain structural information about the phase. Note that the reversibility experiment was performed at the SuperESCA beamline at Elettra Sincrotrone Trieste and the samples were synthesized with the H₂S-filament method. Furthermore, it is important to mention that the temperature was measured on the front of the sample next to the Au(111) crystal (SGM3 endstation and the STM-chamber: the back of the sample). Therefore, the measured transition temperature values might differ compared to the SGM3 endstation and the STM-chamber ones. A phase III sample was located at

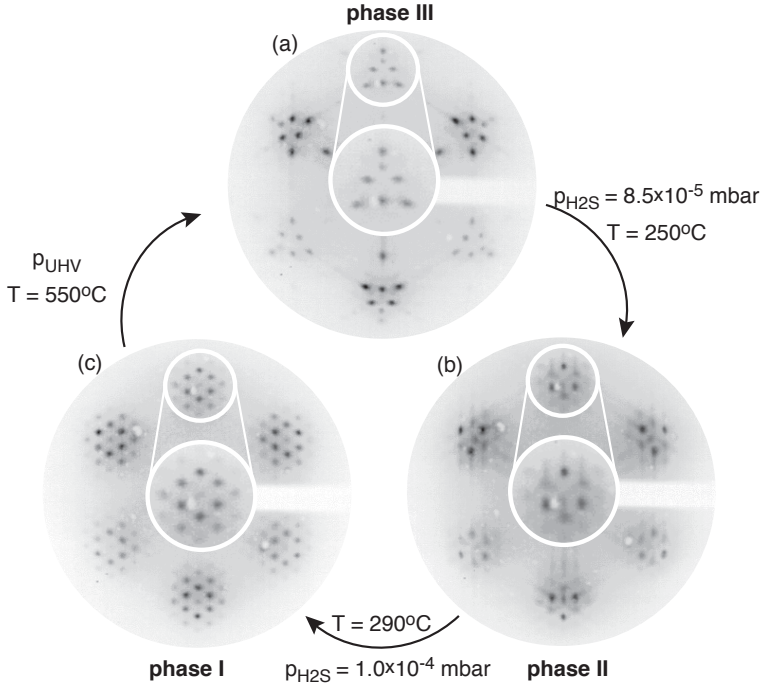


Figure 4.8: Reversibility of the three phases of SL $V_{1+x}S_2$ shown by the evolution of the LEED pattern. The corresponding $V_{1+x}S_2$ phases are indicated in the panels: (a) phase III, (b) phase II and (c) phase I. Annealing temperature and the pressure in the UHV chamber for the corresponding phase transformation is shown in the figure. The white inset shows the magnified part around the diffraction spots. Data acquired at room temperature at a kinetic energy of 93 eV at the SuperESCA beamline.

1 mm distance to the H_2S nozzle to create high local S pressure on the sample surface and simultaneously annealed in order to reverse the phase transformations.

The transformation cycle of phase III to phase I upon annealing in H_2S atmosphere is shown in fig. 4.8. Fig. 4.8(a) shows the characteristic phase III LEED pattern, which transforms into a well-defined phase II diffraction pattern at a H_2S background pressure of 8.5×10^{-5} mbar and an annealing temperature of $250^\circ C$ (fig. 4.8(b)). For a further transformation to phase I, both the H_2S background pressure and the temperature have to be increased, suggesting a more difficult integration of the S atoms in the $V_{1+x}S_2$ SL (fig. 4.8(b) and (c)). The resulting LEED image in fig. 4.8(c) exhibits the typical phase I moiré pattern. The full reversibility by annealing in an H_2S atmosphere underlines the importance of S in each phase transition

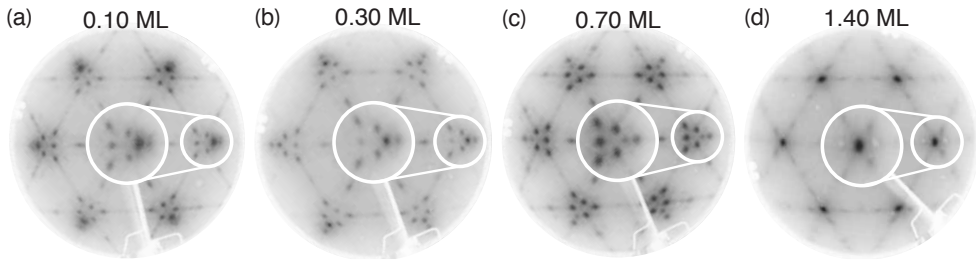


Figure 4.9: Evolution of the LEED pattern for phase III at different coverages of around (a) 0.10 ML, (b) 0.30 ML, (c) 0.70 ML and (d) 1.40 ML, respectively. Data are taken with a kinetic energy of 92.8 eV and at a temperature of 35 K. The white inset shows the magnified part around the diffraction spots.

and supports our hypothesis that phase II and phase III are S deficient compared to phase I.

The evolution of the diffraction pattern for different $V_{1+x}S_2$ coverages can be followed by LEED, as shown for phase III in fig. 4.9. For a coverage of around 0.10 ML (fig. 4.9(a)) the sharp diffraction spots forming the characteristic LEED pattern of phase III are accompanied by the hexagonal diffraction spots of Au(111). The moiré satellite spots of the herringbone reconstruction are clearly visible at low coverage indicating a clean Au(111) surface as seen in fig. 2.7(b). While a coverage of around 0.30 ML in fig. 4.9(b) leads to a noticeable suppression of the Au(111) moiré spots, the diffraction spots of $V_{1+x}S_2$ show no considerable change. Further increase of the coverage in fig. 4.9(c) results in an extinction of the Au(111) moiré satellites and a perceivable increase in intensity of the $V_{1+x}S_2$ contributions. Exceeding the SL limit results in a drastic change in the diffraction pattern as seen in 4.9(d). While most of the typical phase III diffraction contributions vanish, a concentric hexagonal pattern appears. The hexagonal symmetry in the newly appeared reciprocal lattice is compatible with the interpretation that the second layer presumably grows as either the 1T or 2H coordination; which would support the hypothesis that phase III is a purely 2D phase.

While the different growth methods (H_2S -evaporator, DMDS-evaporator and H_2S -filament method) do not influence the physical properties of the material, it can affect the island size, island shape, preferred mirror domain growth and the overall quality of the sample^{2,7,41}. In the case of SL TaS₂ on Au(111) the growth method using the H_2S -evaporator results in the formation of triangular islands with two predominant orientations rotated by 60° with respect to each other, similar to what is seen

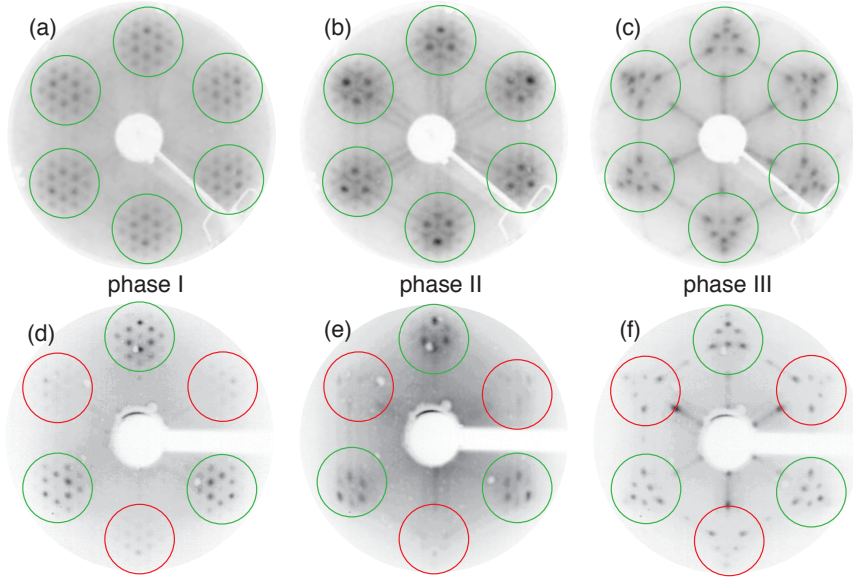


Figure 4.10: Comparison of LEED pattern of $V_{1+x}S_2$ on Au(111) synthesized with (a)-(c) the H_2S -evaporator and (d)-(f) H_2S -filament method, respectively. Data were acquired with a kinetic energy of 80 eV at a temperature of (a)-(c) 35 K at the SGM3 endstation and (d)-(f) at room temperature at the SuperESCA beamline. The phases corresponding to the respective LEED patterns are indicated in the figure. The green and red circles indicate LEED pattern with enhanced intensity and suppressed intensity, respectively.

for phase I in fig. 4.4(a), while the H_2S -filament method leads to the formation of large islands of several hundreds of nm in diameter². With respect to $V_{1+x}S_2$, in the following discussion the H_2S -evaporator and the H_2S -filament synthesis methods are compared concerning LEED, as seen in fig. 4.10. In LEED an uneven distribution of rotational domains is expected to affect the relative spot intensities, but not to influence the diffraction pattern itself. In fig. 4.10(a)-(c) the LEED pattern for the H_2S -evaporator grown samples exhibit a clear 6-fold symmetry. In contrast, the LEED pattern acquired at the same kinetic energy for the H_2S -filament growth (fig. 4.10(d)-(f)) displays a three-fold symmetry, which suggests a non equal distribution of $V_{1+x}S_2$ mirror domains. Only based on LEED, however, a firm statement about the domain distribution is not feasible. In traditional ARPES, as used in this thesis, 60° rotated mirror domains would not affect the overall electronic structure. However, a definite statement about the single orientation of $V_{1+x}S_2$ can be made with XPD,

as will be seen below. Surprisingly, even for phase III a three-fold symmetry is observed, as seen in fig. 4.10(f). A three-fold-like symmetry, as seen in fig. 4.10(f), for a system which consists of two-fold symmetric unit cells in three rotational domains is rather unusual and not expected. However, this fact may suggest that the three-fold hexagonal character of phase II is presumably still present within the V layer and the bottom S (S-Au interface) layer which are not visible by STM. In general the samples synthesized with the H_2S -filament method exhibit overall much sharper diffraction spots compared to the H_2S -evaporator method, indicating a general better quality of the crystal structure and less domain boundaries⁷.

4.3.2 Structural Determination by XPS and XPD

The investigations with STM and LEED could already address several important points for the structural understanding of the three $V_{1+x}S_2$ phases. However, XPS and XPD can give complementary chemical and structural information to answer several open questions about the crystal morphology. In the following three sections the structures of phase I, II and III are determined.

Characterization with XPS

Fig. 4.11 shows the S 2p and V 3p core level spectra from each of the three phases. The differences in the spectra are due to changes in the chemical environment related to the phase transformations. The S 2p core level spectrum of phase I is shown in fig. 4.11(a). The rather complex spectrum originates from two main phenomena: firstly, spin-orbit (SO) coupling leads to the splitting of the S 2p peak into the spin split components S 2p_{3/2} and S 2p_{1/2}. Secondly, chemical shifts give rise to several different components. This can be due to charge transfer to the interface S atoms, which can alter the initial state binding energy, while screening effects from the valence band electrons can alter the final state. In the case of SL TMDCs on Au(111) the interaction with the substrate can lead to different S 2p components which can be assigned to the S-Au(111) interface (bottom-layer) and the S-vacuum interface (top-layer), respectively. Note that it is not possible to ascribe the S 2p core level peaks with certainty to the corresponding bottom-layer and top-layer components *a priori* from the peak positions, as this requires more detailed information about the underlying interactions between the adlayer and the substrate. However, XPD can give information about the location of the emitter atoms and was therefore used to assign each peak component to the corresponding chemical environment of the S atoms. Firstly, we will briefly

characterize the XPS and XPD data before a detailed discussion about the XPS and XPD results is given in section “Discussion of XPS and XPD Data”.

The XPS spectrum for the S 2p core level of phase I is shown in fig. 4.11(a). Four spin-orbit doublets can be identified, with the $2p_{3/2}$ components centered at 160.65(0.02) eV (red), 161.07(0.02) eV (orange), 161.36(0.02) eV (green) and 163.26(0.05) eV (blue) each with a spin-orbit split replica at 1.20(0.04) eV higher binding energy¹⁴⁷.

Upon transformation to phase II (fig. 4.11(b)) no significant peak shift occurs: the $2p_{3/2}$ components are now centered at 160.66(0.02) eV (red), 161.11(0.02) eV (orange), 161.39(0.02) eV (green), and 163.52(0.05) eV (blue) and all the doublets manifest a SO splitting of 1.20(0.04) eV. The stability of the peak positions suggests solely minor changes in the chemical environment of the S atoms.

In fig. 4.11(c), corresponding to phase III, the red $2p_{3/2}$ component exhibits a small shift to higher binding energy (160.74(0.02) eV), and the intensity is significantly reduced, while the intensity of the green component is drastically enhanced, suggesting a more significant change in the crystal structure. Indeed, as described above, a significant structural change is seen in this phase by STM and LEED. The orange and green $2p_{3/2}$ components are now centered at 161.05(0.02) eV and 161.41(0.02) eV. The spin-orbit splitting of 1.19(0.04) eV is in agreement with the splitting of phase I and II.

All components in the S 2p spectra (fig. 4.11(a)-(c)) are fitted with Doniach-Šunjić functions³⁵ and a Shirley background³⁶. As the chemical environment is expected to have only marginal influence on the core hole life-time, the same Lorentzian line shape is used within one phase for all S $2p_{3/2}$ components; the same is assumed for the S $2p_{1/2}$ components. To improve fit reliability the Gaussian broadening of the green and orange components are constrained to be equal. The asymmetric factor α_{DS} of the Doniach-Šunjić function depends mainly on the local density of states at the Fermi energy around the photoemitting species, and therefore α_{DS} was constrained to be the same for corresponding spin-split components. No restriction on the ratio of the spin-split components intensity $2p_{1/2}/2p_{3/2}$ was given. However, the obtained ratio of around 0.5 for all corresponding spin-split component intensities satisfies the multiplicity relationship, neglecting diffraction effects.

The V 3p spectrum for phase I (fig. 4.11(d)) consists of three peaks (pink, purple and grey) centered around 37.32(0.03) eV (pink), 38.48(0.04) eV (purple), and 40.10(0.06) eV (grey). The splitting of around 1.16 eV and 2.78 eV with respect to the lowest binding energy component (pink) excludes the possibility of this being the

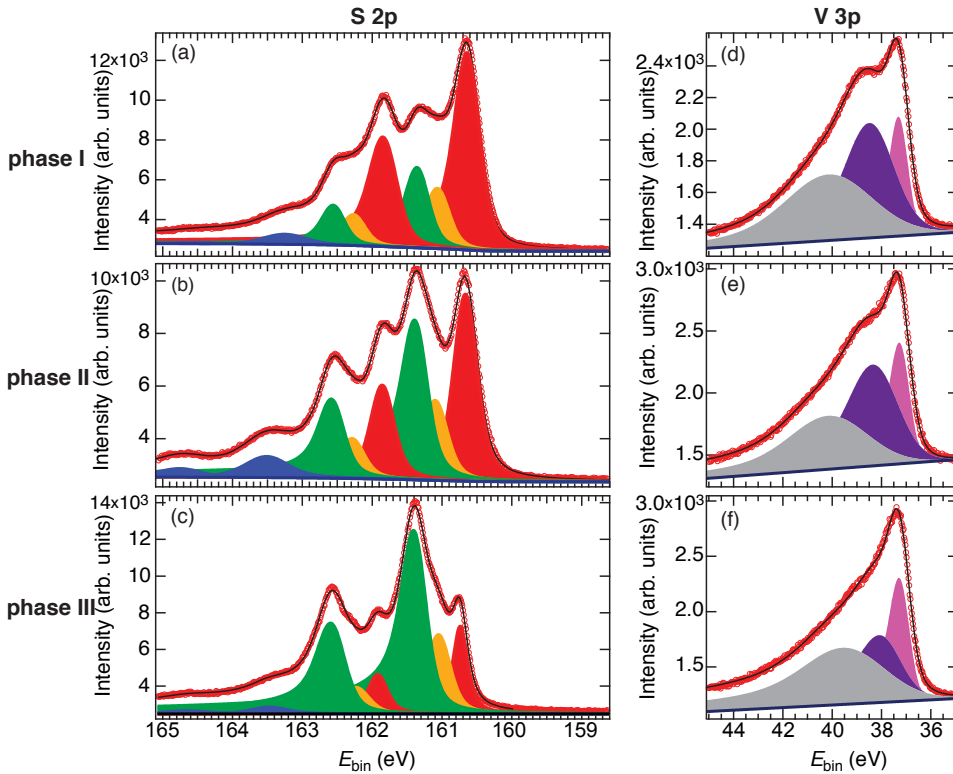


Figure 4.11: XPS spectra of the three phases of $V_{1+x}S_2$ acquired at normal emission and room temperature. The red circles represent the data points, the solid black line the fit and the solid dark blue line the background. Left side: XPS spectra for the spin-split S $2p_{1/2}$ and $2p_{3/2}$ core level states for (a) phase I, (b) phase II and (c) phase III acquired at a photon energy of 260 eV. The peaks are color-coded to indicate the emitter atom from which each core level state derives (see text section “Discussion of the XPS and XPD Data” for discussion): red peaks originate from top-layer S atoms, orange and green from bottom-layer S and the blue peaks are assigned to unordered sulfided species. For same colored peaks: the S $2p_{3/2}$ spin split component is the peak at lower binding energy. Right side: XPS spectra for the V $3p$ state for (d) phase I, (e) phase II and (f) phase III acquired at a photon energy of 170 eV. The different components in the V spectrum are indicated in pink, purple and grey (discussion in section “Discussion of the XPS and XPD Data”).

SO-splitting in V 3p, which is much smaller¹⁴⁸. As seen in fig. 4.11(d)-(f), a shift of the pink, purple and grey component of around 0.04 eV, 0.4 eV and 0.5 eV down in binding energy, respectively, is visible upon the transition to phase III. The change in relative intensity between the purple and pink component from phase II to phase III suggests a more significant change in the chemical environment.

A satisfying fit for the V spectra was obtained with three Doniach-Šunjić functions and a linear background. However, the V 3p is well known for its complex structure due to final states effects¹⁴⁸⁻¹⁵¹. Therefore, a quantitative meaning of the line-shape or the position of the V 3p can not be given. In case of the V 3p spectra, the fitted components are solely used to reliably obtain a measurement of the photoemission intensity.

Characterization with XPD

The determination of the crystal structure of $V_{1+x}S_2$ based on techniques as STM and LEED is rather problematic because of the layered structure, structural flexibility, and complexity of the material. XPD measurements, however, can lift these restraints and can distinguish between the 1T or 1H configurations of TMDCs. In fact, it is even possible to develop new structural models for unknown SL materials based on the diffraction pattern as we will see in the following. However, several technical details need to be considered to take full advantage of this powerful technique.

For example, the choice of the photon energy is crucial, as the kinetic energy of the photoelectrons defines the preferred scattering events: for photoelectron kinetic energies higher than 150 eV, forward scattering prevails, and backscattering is suppressed. By contrast, at lower kinetic energies, forward scattering is suppressed and backscattering is enhanced. Therefore, we used a high photon energy for XPD measurements pertaining to the bottom-layer S atoms and for V, from which we wanted to obtain data primarily resulting from forward scattering processes involving the top-layer S and V while simultaneously suppressing the influence of the Au(111) substrate on the XPD pattern. On the contrary, a low photon energy backscattering regime was used for probing the top-layer S atoms.

In order to interpret XPD data, simulations were made using the EDAC package⁴⁶. In the following, simulations are shown in grey-scale while measurements are shown in an orange-color scale superimposed on the simulations as seen in fig. 4.12. To compare the experimental XPD patterns quantitatively with the simulated data, the so called reliability-factor (R-factor) is computed which contains information about the general agreement of experimental and simulated data. The R-factor is defined

as a mean-square deviation (χ^2) of the experimental χ_{ex} and theoretical modulation function χ_{th} (see equation 2.20) and can be calculated as:

$$R = \sum (\chi_{th} - \chi_{ex})^2 / \sum (\chi_{th}^2 + \chi_{ex}^2), \quad (4.1)$$

where R can have values between 0 and 2, with 0 corresponds to perfect agreement, a value of 1 to uncorrelated data, and a value of 2 to anti-correlated data⁴⁵. In our case a value ≤ 0.3 is considered as an acceptance threshold. For all three phases several lattice constants and different crystal structures were used until the best agreement between the experimental and simulated data was obtained: the final structure is determined by minimizing the R-factor. The obtained R-factors for the presented data and simulations are noted in the corresponding panels in fig. 4.12.

In the simulations the substrate was neglected. This neglect is motivated by requirements of computational feasibility, but is justified physically: a multitude of adsorption sites can exist when, as here, the lattice mismatch leads to a supercell, in which a variety of relationships exist between the atomic positions of the emitter atoms and of the substrate that tend to average out the effect on the diffraction pattern. Moreover, because we are able to enhance forward scattering at the expense of backscattering by the choice of photon energies, we minimize the impact of the substrate on the measurements of the bottom-layer S and the V layers, which would presumably be most affected by its proximity. As we see in the next section, the assumed simplification appears to be confirmed by the excellent agreement obtained between the XPD simulations and the XPD data.

In order to demonstrate the possibilities of XPD, EDAC simulations (grey discs) under the same conditions for 1H- and 1T- VS_2 are performed. As we can see in fig. 4.12, it is possible to unequivocally assign top- and bottom-layer S atoms to the corresponding diffraction pattern. The bottom S $2p_{3/2}$ simulations for the 1H and 1T configurations can be instantly distinguished (fig. 4.12(a) and (e)). However, the XPD simulations for 1H and 1T V 3p and top S $2p_{3/2}$ look similar (fig. 4.12(b)-(c) and (f)-(g)). This can be explained by the fact that forward-scattered electrons emitted from the bottom S atoms face a totally different scattering environment in 1H versus 1T layers, as can be seen in the ball models in fig. 4.12(d) and (h). Forward-scattered V 3p photoelectrons, however, show an identical local arrangement of top S atoms in 1H and 1T configurations, and therefore the resulting XPD patterns are very similar; the same argument applies for backscattered top S $2p_{3/2}$ photoelectrons. The small differences in the 1H and 1T V 3p simulations stem from a contribution of partly backscattered electrons that see the bottom S layer and also from multiply

scattering events. In the case of the top S $2p_{3/2}$ simulations, the electrons of 1H and 1T are identically backscattered by the V layer, and the smaller contributions from the differently arranged bottom S layer leads to only very small differences between the 1H and 1T simulations. However, major differences in the diffraction pattern for the respective bottom-layer S $2p_{3/2}$ core level allow to directly identify the 1H and 1T configuration with XPD.

Discussion of the XPS and XPD Data

In order to interpret XPD data, the experimental and simulated diffraction pattern have to be quantitatively compared. Note that for the following XPD analysis only the S $2p_{3/2}$ and the pink V 3p component are considered as these peaks show the clearest intensity modulation for photoelectrons stemming from the same chemical environment. Fig. 4.12(e)-(g) show the experimental XPD pattern for phase I superimposed on the XPD simulation of 1T- VS_2 . All three diffraction patterns obtained from phase I show excellent agreement with simulations of an idealized 1T single rotational domain. The poor visible agreement between the 1H simulation of bottom-layer S $2p_{3/2}$ rules out the possibility that phase I is the 1H coordination. Note that the distinct three-fold symmetry and the excellent agreement of the simulation and the experiment in all phase I XPD patterns points to the possibility of a preferred single-domain orientation of phase I with high structural quality. The S $2p_{3/2}$ and V 3p core level components in the XPS spectra in fig. 4.11 can be unequivocally assigned to the emitter atoms by the XPD patterns and the corresponding XPD simulations, as indicated by the colored circles and small arrows in fig. 4.12. In the case of S $2p_{3/2}$, the red component can be ascribed to the top-layer S atoms, and the green one to the bottom-layer S atoms. The similar XPD pattern for the orange and green component (fig. 4.13(a) and (b)) indicate that the corresponding photoelectrons both stem from bottom-layer S atoms. The splitting of 0.29(0.03) eV between the orange and green peak is presumably explainable with the presence of the moiré structure observed in the $V_{1+x}S_2$ phases: different contributions of interaction strengths between the bottom S layer and the Au(111) substrate leading to a great number of small core level contributions shifted in binding energy and forming together a “weak” and “strong” interacting main peak, similar to what has been observed in previous studies of epitaxial graphene on transition metal surfaces¹⁵². Note that the direct identification of the weak and strong interacting components is not possible even with XPD. A lower-intensity S $2p_{3/2}$ component at 163.26(0.05) eV is indicated in blue and does not show any modulation in the XPD pattern. This, together with the big shift on

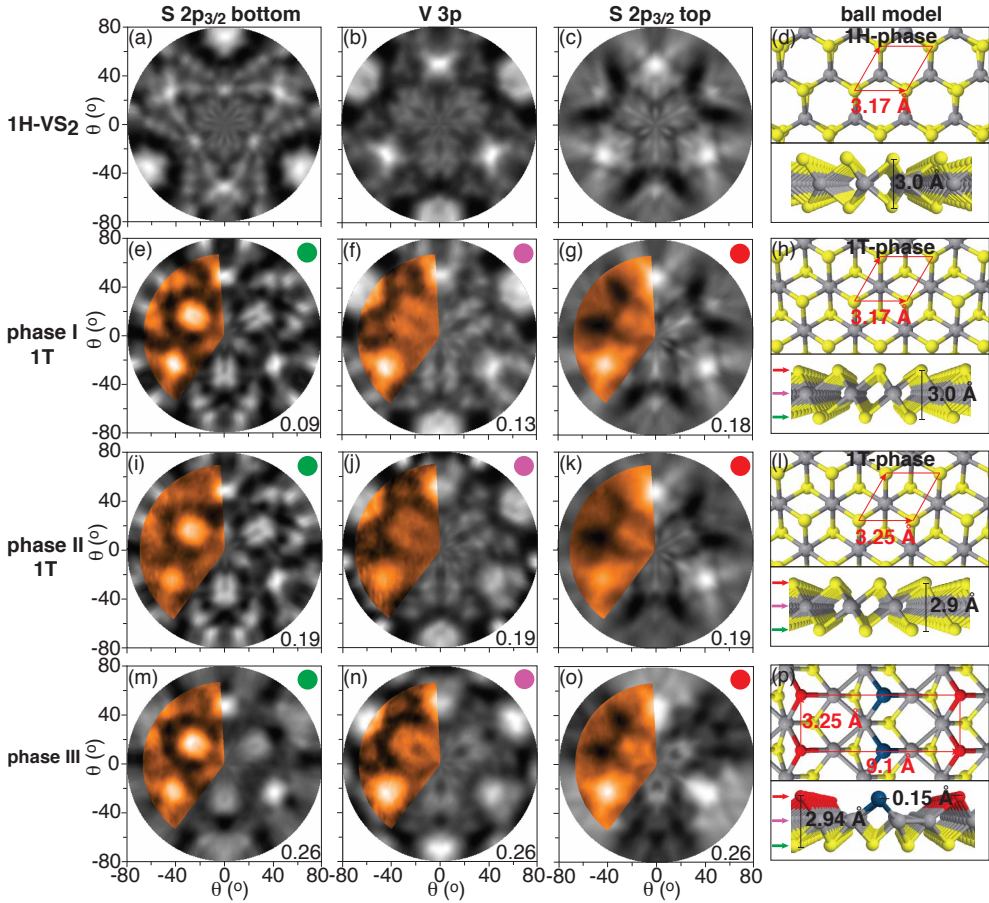


Figure 4.12: Overview of the XPD data for the three phases of $V_{1+x}S_2$. Top row: XPD simulations for 1H- VS_2 (a) bottom-layer S $2p_{3/2}$, (b) V $3p$ and (c) top-layer S $2p_{3/2}$ simulated for kinetic energies of 239 eV, 233 eV and 109 eV, respectively. (d) Crystal lattice used for the simulation in (a)-(c) with the lattice constants noted in the panel. Second row: stereographic projections of the modulation function for phase I for (e) bottom-layer S $2p_{3/2}$, (f) V $3p$ and (g) top-layer S $2p_{3/2}$ taken at a photon energy of 400 eV, 270 eV and 270 eV, corresponding to a kinetic energy of 239 eV, 233 eV and 109 eV, respectively. The orange colored sectors are the experimental data and the grey discs are the XPD simulations for 1T- VS_2 . The colored circles in each panel mark the corresponding colored peak in fig. 4.11 used for XPD and the corresponding color coded arrows in the ball model side view indicate the corresponding emitter atoms. The number in each panel refers to the obtained R-factor. (h) Crystal lattice used for the simulations in (e)-(g) with the lattice constants noted in the panel. Third row: (i)-(h) corresponding stereographic projections of the modulation function for phase II with the used lattice for the simulations shown in (l) and the lattice constants noted in the panel. Bottom row: (m)-(o) corresponding stereographic projections of the modulation function for phase III with the used lattice for the simulations shown in (p) and lattice constants noted in the panel. In the case of phase III only one of the three domains is illustrated in (p), but the three orientations were included in the simulations.

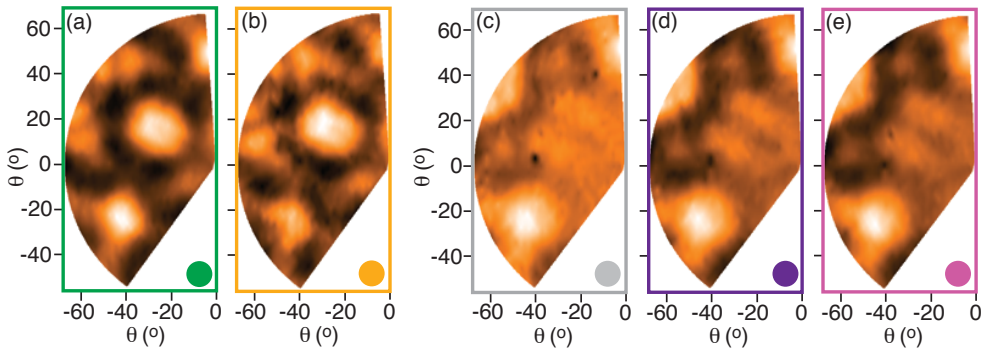


Figure 4.13: Stereographic projections of the modulation function for phase I. The colored circles in each panel mark the corresponding peak component in fig. 4.11. For the bottom-layer S $2p_{3/2}$ core levels: (a) green component and (b) orange component in fig. 4.11(a). And for V $3p$ core levels: (c) grey, (d) purple and (e) pink component in fig. 4.11(d). Acquired at a photon energy of 400 eV for S $2p$ and 270 eV for V $3p$.

binding energy and the large peak width of the blue component points to a small amount of unordered sulfided species on the surface.

In the case of V, the existence of three distinct V $3p$ components would naïvely suggest the presence of V in different chemical environments. However, as mentioned above, the V $3p$ is well known for its complex structure due to final state effects and furthermore all three peaks exhibit a similar XPD pattern as seen in fig. 4.13(c)-(e), which indicates that they stem from the same chemical environment. A similar V $3p$ triplet structure with two broad peaks and one more defined peak has been previously observed on vanadium sesquioxide (V_2O_3), where the more defined peak at lower binding energy (here pink) was ascribed to a shake-down satellite of the second peak (here purple)^{149–151}. The very broad component at higher binding energy (grey) is presumably attributed to secondary energy losses of the photoelectrons or excitation of plasmons resulting in shake-up satellites^{34,148}. Due to the complex structure of the V $3p$ core level, a quantitative analysis of the line-shape or the position of the V $3p$ components upon the phase transition will not be performed.

The XPD data for phase II, fig. 4.12(i)-(k), sustain all main features seen for phase I (fig. 4.12(e)-(g)), with only minor changes observable. The best agreement between XPD measurements and simulation is again found for a single-domain orientation of the 1T coordination, but with slightly increased lattice constant (fig. 4.12(l)) similar to what has been observed in LEED. This result supports the finding

of Ref.¹²⁷ that S depletion in the bulk is accompanied by a small increase of the lattice constant that nevertheless preserves the 1T configuration. Indeed, it is tempting to make a statement about phase-transformation-induced S loss, using as a basis the change in the relative peak intensities from panels (a) to (b) in fig. 4.11. However, such a statement would be tenuous, since photoemission intensity is influenced not only by stoichiometry, but also by the fact that photoelectrons experience scattering processes that modulate the core level intensity as a result of changes in the crystal structure. Note that the relative intensity of the blue contamination component increases, which is attributed in this case to an annealing step in H_2S atmosphere⁶. It worth mentioning that the V spectra should show an additional component for the presumably formed interstitial V upon the phase transition. However, in our case this peak cannot be directly observed due to the very broad and partly overlapping V peaks. Therefore, we cannot totally exclude the formation of interstitial V already in phase I and we still refer to phase I as 1T- $V_{1+x}S_2$ and not as the stoichiometric 1T- VS_2 .

The lattice structure of phase III is not compatible with any known bulk $V_{1+x}S_2$ compound as shown by the STM and LEED results. It is worth mentioning that due to the up-down modulation of the top S atoms (observed in fig. 4.5(b) and (c)), a splitting of the red core level component might be expected. However, the effect on the core level seems marginal, and therefore the top-down modulating S atoms were fitted as one peak. The intensity of the bottom S component (green) is enhanced and shows no significant shift, while the orange $2p_{3/2}$ component has shifted slightly to 161.05(0.02) eV. However, as the weak and strong interacting bottom S peaks consist of a contribution of a great number of small components, a statement about the change in the chemical environment solely based on the core level shift would not be accurate. The intensity of the blue component located at 163.47(0.05) eV is reduced, as might be expected simply as a result of the desorption of the unordered sulfided species at elevated temperatures.

Regarding phase III, a structural model needs to be identified by finding the structural parameters that simulate the observed XPD data the best. The structure must, furthermore, be consistent with STM and LEED data which means it must possess a rectangular $9.1 \text{ \AA} \times 3.28 \text{ \AA}$ surface unit cell (from LEED) and exhibit up-down modulations of the top S along the direction of the longer side of the unit cell,

⁶As the annealing temperature was too high during the phase I to II transformation, phase III was unintentionally obtained. Therefore, the phase transition cycle for XPS and XPD has been phase I to phase III to phase II.

and must be obtainable by a plausible phase transition (involving S loss) from the known structure of phase II (fig. 4.12(l)). The simulation must also be optimized to agree with the XPD measurements. The resulting structure is shown in fig. 4.12(p). To form such a structure, every second top S line in the $\langle 11\bar{2}2 \rangle$ direction of phase II has to desorb and the remaining top S rearrange to obtain the required rectangular unit cell. The positions of the hexagonally arranged V and bottom S atoms have to be adjusted as well, as shown in the figure, with the V atoms forming zig-zag wires. Note that the coordination of the V atoms remained “octahedral-like” in phase III as suggested by the similarity of the experimental XPD data of phase III with phase I and II (fig. 4.12). Furthermore, we have to consider that XPD, similar to ARPES, is a space averaging technique that considers all intensity contributions within the beam-spot. Therefore, the simulations which are shown in grey-scale in panels (m)-(o), account for three domains rotated by 0 , 120° and 240° , in accordance with STM and LEED observations. It should be mentioned that the different contributions of the three rotational domains lead to the three-fold symmetry observed in XPD, suggesting minor changes in the structure in the V layer and the bottom-layer S atoms as also seen in the model structure in fig. 4.12(p). In general we find a qualitative and quantitative agreement between the simulated XPD pattern and the experimental XPD data, suggesting that the proposed crystal structure for phase III is indeed close to the actual crystal morphology.

4.4 Electronic Structure of Single Layer $V_{1+x}S_2$ on Au(111)

Finally, we compare the effect of the phase transitions on the electronic structure of the SL phases. Before performing ARPES measurements, we confirmed the structural phase of each sample using LEED. Note that for all phases a photon energy of 94 eV was chosen to enable a direct comparison of the electronic structures without interference of the photon energy dependent matrix element effects. We note that the data presented in this section were all acquired from samples with partial mono-layer coverage (around 0.7 ML), with considerable clean Au(111) exposed in between the single layer islands. Furthermore, a cleaning of the sample by annealing was not possible before measurements of the phase I structure, as the elevated temperature would induce a phase transformation. Therefore, it is expected that the electronic structure of phase I might be appear broader due to additional secondary scattering

effects.

The ARPES data of phase I in fig. 4.14(a) and (b) show the photoemission intensity along constant energy contours at different binding energies, together with the high symmetry cut in the $\bar{M}\bar{\Gamma}\bar{K}\bar{M}$ directions, respectively. The BZ of SL phase I is marked by green dashed lines. The photoemission data reveals both Au(111) features¹⁵³ and additional features that can be assigned to the SL. Apart from the hexagonal-looking bulk Au sp states near the edge of the BZ, phase I exhibits a Fermi contour consisting of a round feature around $\bar{\Gamma}$ and a flower-like pattern consisting of six elongated petal-shaped electron pockets centered around \bar{M} . Comparison of the measurements with Fermi surfaces calculated from DFT in fig. 4.3(a) and (b) support the identification by XPD of the crystal structures as 1T and derivatives therefrom: The calculation of the 1T Fermi surface (fig. 4.3(b)) shows a flower-like structure with petals radiating toward \bar{M} , similar to the measurements, while the calculation for 1H (fig. 4.3(a)) manifests an entirely dissimilar hexagonal contour around the BZ center and double rounded-triangles at the \bar{K} points. The band crossings through the Fermi surface immediately establish the metallic nature of phase I. As seen in the high symmetry cut in fig. 4.14(b) the photoemission features are broad, a fact which remains to be understood but is likely due to a combination of factors including adsorbates on the surface, possible occurrence of strongly correlated electronic states in this system¹¹⁸⁻¹²⁰ and interaction of the $V_{1+x}S_2$ states with the projected bulk band structure of Au(111)¹⁵⁴. Additional challenges arise due to the presence of the intense Au sp bands, although the photon energy was chosen to simultaneously enhance the features of interest and suppress the Au sp states to the greatest degree possible. Note that the Au(111) surface state (SS) is not clearly visible in the photoemission spectra which indicates a great number of adsorbates on the surface.

ARPES measurements of phase II (fig. 4.14(c) and (d)) show a strong similarity to those of phase I. All the characteristic photoemission features observable in phase I can also be identified in phase II, including the round feature near $\bar{\Gamma}$ originating from an electron pocket and the flower-like pattern consisting of six elongated petal-shaped electron pockets centered around \bar{M} . This finding is consistent with the observations from LEED, STM and XPD that for phase II the 1T configuration is preserved, with a slight expansion of the 2D lattice. Note that such a small variation in the lattice constant is not perceptible in the photoemission data, particularly in view of the rather broad and poorly defined bands; however, the 1T character of the electronic band structure of phase II is clearly observable. Moreover, the Au(111) SS is better visible but still not clearly observable suggesting a partial desorption of contaminants

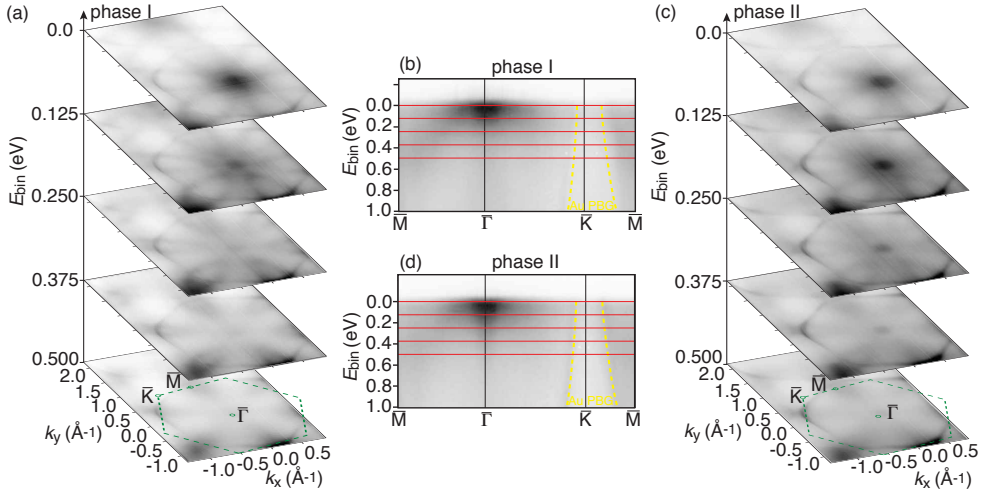


Figure 4.14: Comparison of the ARPES data for phase I and II on Au(111). Acquired at a photon energy of 94 eV and a temperature of 35 K. (a) Photoemission intensity along constant energy contours for different binding energies for phase I. The green dashed hexagon marks the BZ for phase I. The high symmetry points are labeled in the panel. (b) Photoemission intensity along the $\bar{M}\bar{\Gamma}\bar{K}\bar{M}$ directions for phase I. The dashed yellow lines indicate the projected bulk band gaps (PBG) of Au(111). The red solid lines mark the binding energies used for the constant energy contours in (a). (c) Photoemission intensity along constant energy contours for different binding energies for phase II and (d) photoemission intensity along the $\bar{M}\bar{\Gamma}\bar{K}\bar{M}$ directions for phase II. The green dashed hexagon marks the BZ for phase II.

upon annealing.

Lastly, the electronic structure of SL phase III is studied. Fig. 4.15(a) and (b) show the ARPES data of phase III with the photoemission intensity along constant energy contours at different binding energies, together with the high symmetry cut along the $\bar{Y}\bar{\Gamma}\bar{R}\bar{X}\bar{\Gamma}$ directions, respectively. An important point to address is that ARPES probes simultaneously all three domains of phase III within the beam spot dimension ($200\ \mu\text{m} \times 50\ \mu\text{m}$) and therefore the photoemission intensity acquired for phase III is in fact an incoherent superposition of the intensities of three coexisting rotational domains. The BZs for each domain has been constructed based on the unit cell parameter obtained from LEED and STM, and these are marked in fig. 4.15(a) in green, pink and blue, respectively. In the case of phase III, the main photoemission features of the constant energy cut at the Fermi level are an enhanced intensity

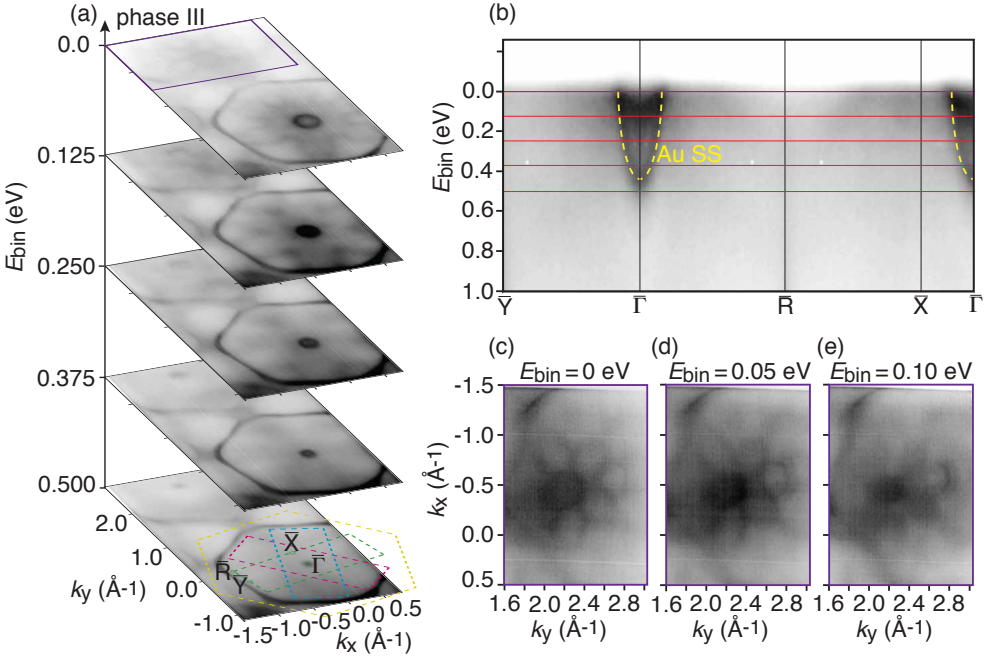


Figure 4.15: (a) Photoemission intensity along constant energy contours for different binding energies for phase III on Au(111). Acquired at a photon energy of 94 eV and a temperature of 35 K. The green, blue and pink rectangles indicate the BZs for phase III and the yellow hexagon the BZ for Au(111). The high symmetry points of phase III are labeled in the panel for the green BZ domain. The purple rectangle marks the collection of the seven circles (Christmas-tree-like feature). (b) Photoemission intensity along the $\bar{Y}\bar{\Gamma}\bar{R}\bar{X}\bar{\Gamma}$ directions for phase III. The dashed yellow lines indicate the Au(111) SS. The red solid lines mark the binding energies for constant energy contours used in (a). (c)-(e) Magnified constant energy cuts of the area marked with the purple rectangle from (a) (Christmas-tree-like feature). The contrast is slightly saturated for a better observations of the photoemission features. The binding energy of each constant energy cut is marked in the corresponding panel.

around $\bar{\Gamma}$ and a snowflake-like feature that appears, for the photon energies used here, contained within the Au sp states. The high symmetry cut along the $\bar{Y}\bar{\Gamma}\bar{R}\bar{X}\bar{\Gamma}$ directions reveals furthermore that the round feature around the first $\bar{\Gamma}$ originates from two distinct electron pockets with minima at binding energies of around 0.12 eV and 0.45 eV. The electron pocket at higher binding energy can be ascribed to the Au(111) SS¹⁵³, whereas the electron pocket located closer to the Fermi level can be assigned to an electronic feature of phase III. Furthermore, an unusual collection of seven circles

forming a Christmas-tree-like feature (marked with a purple rectangle in fig. 4.15(a) and better visible in fig. 4.15(c) magnified and with slightly saturated contrast) is observable in the second Au(111) BZ. The constant energy cuts in fig. 4.15(c)-(e) reveal that the seven circles consist of six shallow electron pockets and the Au(111) SS in the second BZ (see fig. 4.15(a)). As we shall see below, this unusual features can be qualitative explained by the three rotational domains of phase III. In order to ascribe special photoemission features of phase III to a specific rotational domain the electronic structure of a single-domain bulk sample (as in section 3.4) or theoretical calculations are needed. As the crystal structure of phase III is, as far as we know, not existent in bulk form, and the DFT-calculation could not be completed before the hand-in of this thesis, a quantitative discussion of the photoemission features is unfortunately not possible at the current time.

However, some of the observed photoemission features of the Fermi contour can be qualitatively explained by constructing the $\bar{\Gamma}$ point positions of higher order BZs for the three rotational domains over the whole available k-space. Fig. 4.16(a) shows the photoemission intensity from phase III integrated in a 120 meV window around the Fermi level in order to enhance the intensity of the Christmas-tree-like feature. As the orientation of the Au(111) substrate with respect to the phase III domains is known from LEED (fig. 4.7), higher order BZs for one single rotational domain (green dashed lines) can be superimposed on the Fermi surface as shown in fig. 4.16(a), and rotated to 120° and 240° to obtain fig. 4.16(b). By marking the $\bar{\Gamma}$ points of all constructed BZs with corresponding colored circles and subsequently deleting the constructed BZs grids, the positions of the $\bar{\Gamma}$ points of the three rotational domains over the whole available k-space can be directly identified in the Fermi surface shown in fig. 4.16(c). The agreement is excellent for the positions of the higher order $\bar{\Gamma}$ points coincident with the low intensity areas of the snowflake-like feature as well with the center of the 7 circles forming the Christmas-tree-like structure. In consideration of the fact that $\bar{\Gamma}$ in the first BZ of phase III exhibits a round electron pocket feature the formation of the Christmas-tree-like feature can be assigned to higher order $\bar{\Gamma}$ points from different domains of phase III together with the $\bar{\Gamma}$ point of Au(111) (yellow circle) in the second Au BZ as seen fig. 4.16(d), similar to what we observe in LEED (fig. 4.16(e)). However, it is to point out that this qualitative analysis of the Fermi surface does not explain all observable photoemission features, especially in the case of the snowflake-like feature. Therefore, theoretical calculations are crucial for a more detailed investigation of the electronic structure of phase III.

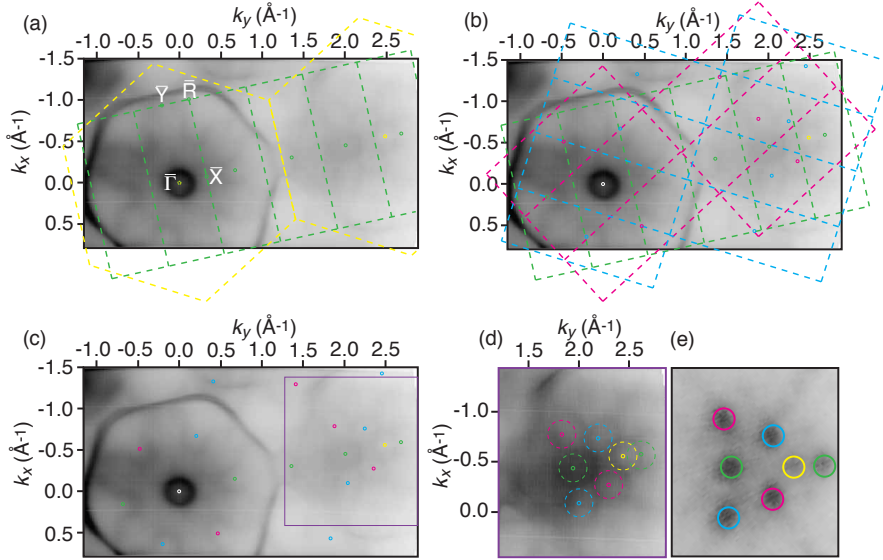


Figure 4.16: Qualitative explanation of the phase III Fermi surface, acquired at a photon energy of 94 eV and a temperature of 35 K. (a) Photoemission intensity of phase III on Au(111) integrated over a 120 meV range around the Fermi energy. The green rectangles and the yellow dashed hexagons indicate the BZ of one of three rotational domains of phase III and Au(111), respectively. The high symmetry points of phase III are labeled in the panels and marked with green circles. The yellow circles correspond to the $\bar{\Gamma}$ points of Au(111). (b) Same image as (a) but the green, blue and pink rectangles indicate the BZs of the three rotational domains of phase III. The colored circles (green, blue and pink) show the $\bar{\Gamma}$ points of the different domains of phase III. (c) Same image as (a) but with the BZ grid removed in order to observe better the positions of the $\bar{\Gamma}$ points. The purple rectangle marks the collection of the seven circles (Christmas-tree-like feature). (d) Magnification of the purple rectangle (slightly saturated contrast) in (c) and compared with (e) the magnification from LEED (fig. 4.7(c)).

Chapter 5. Conclusion and Outlook

In this last chapter a short summary of the main results of this work are outlined, as well as a brief outlook on experiments, particularly pertaining to the $V_{1+x}S_2$ project, that are currently in progress or planned for the near future.

5.1 Summary

The work presented in this thesis can be divided into the following two main topics: the synthesis of thin film ICs on a topological insulator, *i.e.* Bi_2Se_3 and Bi_2Te_3 , and the synthesis of SL $V_{1+x}S_2$ on Au(111). The crystal and electronic structure of the films were investigated in detail, exploiting STM, LEED and ARPES techniques, and in the case of SL $V_{1+x}S_2$ additionally with XPS and XPD. The experimental results have been supported with theoretical band structure calculations and in the case of XPD measurements, with simulations performed using the EDAC package⁴⁶. The results and conclusions that have been reached in each chapter are summarized here:

- **Thin film FeSe on Bi_2Se_3 :** FeSe thin films with a thickness of 3-5 ML were grown on Bi_2Se_3 in three rotational domains. Superconducting properties have been observed in previous studies for monolayer FeSe²³, however low temperature STS shows no sign of a superconducting gap for any measured layer thickness in FeSe thin films on Bi_2Se_3 at the temperature down to 5 K. Photoemission measurements reveal a faint dumbbell-like feature at the \bar{M} point, which is associated with a similar feature of the non-superconducting phase of 3 ML FeSe grown on $SrTiO_3$ ²³. Two well defined coexisting topological surface states are observable, which can be ascribed to the exposed Bi_2Se_3 substrate and to a strongly n-doped state at the FeSe/ Bi_2Se_3 interface.

- **Thin film FeTe on Bi₂Te₃:** The synthesis approach for thin film FeSe on Bi₂Se₃ was successfully modified in order to grow a few layers of FeTe on Bi₂Te₃. The main photoemission features of the bulk Fe_{1.08}Te crystal and the thin film exhibit close similarity to one another. The electronic band structure of bulk Fe_{1.08}Te are therefore utilized as a guide to disentangle the complex photoemission features of the thin film. This approach solves the problem of simultaneously probing the three rotational domains of the FeTe thin films. A charge transfer from the FeTe adlayer to the substrate is indirectly observed as a shift in the bands towards deeper binding energy of the substrate's photoemission features upon formation of the thin film. Intentional surface doping with Rb atoms, however, results in an insignificant shift of the overall band structure which can be assigned to the high density of states near the Fermi level and is further supported by ab-initio calculations. The analysis techniques developed for FeTe thin films on Bi₂Te₃ in this section can be adapted for similar approaches to analyzing other multiple rotational domain systems.
- **Single layer V_{1+x}S₂ on Au(111):** A growth procedure for SL TMDCs (WS₂, MoS₂ and TaS₂) on Au(111) was successfully modified for the synthesis of metallic V_{1+x}S₂ on Au(111). Two distinct phase transformations of the as-grown layer were observed by simply annealing in UHV. Annealing in H₂S atmosphere, however, reversed the transformations, and this fact implicates S loss as the trigger for the phase transformation. The complementary use of several structural techniques allowed the development of a model structure for each phase. The crystal morphology of the so-called phase I and phase II were identified as the 1T coordination with slightly different lattice constants. The crystal structure for phase III, however, exhibits a crystal morphology different from that of any known V_{1+x}S₂ compound. The structural findings for phase I and II are further supported by ARPES measurements and DFT band structure calculations of free standing VS₂. Phase III was found to exhibit three rotational domains rotated by 0, 120° and 240° with respect to the Au(111) substrate. In the presence of the three rotational domains of phase III a part of the photoemission intensity at the Fermi level can be qualitative explained by mirroring the feature at normal emission according to the higher order BZs.

With the surge of interest in TMDC research, SL V_{1+x}S₂ is a promising and versatile material and this thesis has laid the groundwork to underpin a number of exciting future experiments.

We plan to explore phase III in greater detail because this structure appears to only exist at the SL limit. The underlying processes which might stabilize phase III might be for example confinement effects or substrate-adlayer interactions. To verify this hypothesis, we plan to use a combination of STM, LEED and ARPES to look at both the crystal structure and electronic structure of phase III on multiple substrates and different thicknesses. The growth of SL $V_{1+x}S_2$ on graphene should minimize the effect of the substrate and reveal if phase III can still be obtained or even another structural morphology can be observed⁶. Furthermore, STM measurements of partly bilayer phase III grown on Au(111) allow the simultaneously imaging of single and bilayer islands and should reveal if the formation of the characteristic stripe pattern is still observable at multiply layer thicknesses.

Another open question is whether to lift the Mermin-Wagner restriction in SL $V_{1+x}S_2$ to introduce long-range ferromagnetic ordering in the 2D limit. The first test measurements with a antiferromagnetic Cr-tip on phase III of $V_{1+x}S_2$, performed by the group of Prof. Alexander Khajetoorians (Radboud University), point to the possible existence of spin density waves or intrinsic magnetic order in the material. However, this very preliminary result has to be investigated more carefully and additional measurements are planned for spin STM with an applied magnetic field.

The aim of this work was to understand some of the intriguing and remarkable properties of the presented novel 2D transition metal chalcogenides. In the case of ICs, the direct comparison of FeSe and FeTe near the 2D limit shows differences in their electronic structures which might take us one step closer to understanding the key ingredients for unconventional superconductivity. Single layer VS_2 , however, is especially interesting due to its predicted 2D intrinsic magnetism. The ability to synthesize SL $V_{1+x}S_2$ on Au(111) in three different phases and induce and reverse a phase transition may be especially interesting in the light of controllable 2D magnetism in this system. The properties of these novel 2D transition metal chalcogenides combined with the ability to synthesize them in atomically thin layers make them especially interesting for high-performance functional nanomaterials, spintronics application and data storage systems, and therefore to a key element for the development of future technologies.

Bibliography

- [1] M. Dendzik, M. Michiardi, C. Sanders, M. Bianchi, J. A. Miwa, S. S. Grønberg, J. V. Lauritsen, A. Bruix, B. Hammer, and Ph. Hofmann. Growth and electronic structure of epitaxial single-layer WS₂ on Au(111). *Phys. Rev. B*, 92:245442, 2015.
- [2] C. E. Sanders, M. Dendzik, A. S. Nганкеу, A. Eich, A. Bruix, M. Bianchi, J. A. Miwa, B. Hammer, A. A. Khajetoorians, and Ph. Hofmann. Crystalline and electronic structure of single-layer TaS₂. *Phys. Rev. B*, 94:081404, 2016.
- [3] J. A. Miwa, S. Ulstrup, S. G. Sørensen, M. Dendzik, A. G. Cabo, M. Bianchi, J. V. Lauritsen, and Ph. Hofmann. Electronic structure of epitaxial single-layer MoS₂. *Phys. Rev. Lett.*, 114:046802, 2015.
- [4] X. Xu, W. Yao, D. Xiao, and T. F. Heinz. Spin and pseudospins in layered transition metal dichalcogenides. *Nat. Phys.*, 10:343–350, 2014.
- [5] Z. Y. Zhu, Y. C. Cheng, and U. Schwingenschlögl. Giant spin-orbit-induced spin splitting in two-dimensional transition-metal dichalcogenide semiconductors. *Phys. Rev. B*, 84:153402, 2011.
- [6] J. A. Miwa, M. Dendzik, S. S. Grønberg, M. Bianchi, J. V. Lauritsen, Ph. Hofmann, and S. Ulstrup. Van der waals epitaxy of two-dimensional MoS₂–graphene heterostructures in ultrahigh vacuum. *ACS Nano*, 9:6502–6510, 2015.
- [7] S. S. Grønberg, S. Ulstrup, M. Bianchi, M. Dendzik, C. E. Sanders, J. V. Lauritsen, Ph. Hofmann, and J. A. Miwa. Synthesis of epitaxial single-layer MoS₂ on Au(111). *Langmuir*, 31:9700–9706, 2015.
- [8] N. D. Mermin. Crystalline order in two dimensions. *Phys. Rev.*, 176:250, 1968.
- [9] J. C. Meyer, A. K. Geim, M. I. Katsnelson, K. S. Novoselov, T. J. Booth, and S. Roth. The structure of suspended graphene sheets. *Nature*, 446:60–63, 2007.

- [10] A. Fasolino, J. H. Los, and M. I. Katsnelson. Intrinsic ripples in graphene. *Nat. Mater.*, 6:858–861, 2007.
- [11] P. R. Wallace. The band theory of graphite. *Phys. Rev.*, 71:622, 1947.
- [12] S. Hagstrom, H. B. Lyon, and G. A. Somorjai. Surface structures on the clean platinum (100) surface. *Phys. Rev. Lett.*, 15:491, 1965.
- [13] J. W. May. Platinum surface LEED rings. *Surf. Sci.*, 17:267 – 270, 1969.
- [14] J. C. Shelton, H. R. Patil, and J. M. Blakely. Equilibrium segregation of carbon to a nickel (111) surface: A surface phase transition. *Surf. Sci.*, 43:493–520, 1974.
- [15] K. S. Novoselov, A. K. Geim, S. V. Morozov, D. Jiang, Y. Zhang, S. V. Dubonos, I. V. Grigorieva, and A. A. Firsov. Electric field effect in atomically thin carbon films. *Science*, 306:666–669, 2004.
- [16] C. Gómez-Navarro, M. Burghard, and K. Kern. Elastic properties of chemically derived single graphene sheets. *Nano Lett.*, 8:2045–2049, 2008.
- [17] K. S. Novoselov, V. I. Fal’ko, L. Colombo, P. R. Gellert, M. G. Schwab, and K. Kim. A roadmap for graphene. *Nature*, 490:192–200, 2012.
- [18] Y. Zhang, Y.-W. Tan, H. L. Stormer, and P. Kim. Experimental observation of the quantum hall effect and berry’s phase in graphene. *Nature*, 438:201–204, 2005.
- [19] K. S. Novoselov, Z. Jiang, Y. Zhang, S. V. Morozov, H. L. Stormer, U. Zeitler, J. C. Maan, G. S. Boebinger, P. Kim, and A. K. Geim. Room-temperature quantum hall effect in graphene. *Science*, 315:1379–1379, 2007.
- [20] K. S. Novoselov, A. K. Geim, S. V. Morozov, D. Jiang, M. I. Katsnelson, I. V. Grigorieva, S. V. Dubonos, and A. A. Firsov. Two-dimensional gas of massless dirac fermions in graphene. *Nature*, 438:197–200, 2005.
- [21] A. K. Geim. Random walk to graphene (nobel lecture). *Angewandte Chemie International Edition*, 50:6966–6985, 2011.
- [22] J.-F. Ge, Z.-L. Liu, C. Liu, C.-L. Gao, D. Qian, Q.-K. Xue, Y. Liu, and J.-F. Jia. Superconductivity above 100 K in single-layer FeSe films on doped SrTiO₃. *Nat. Mater.*, 14:285–289, 2015.

- [23] Y. Miyata, K. Nakayama, K. Sugawara, T. Sato, and T. Takahashi. High-temperature superconductivity in potassium-coated multilayer FeSe thin films. *Nat. Mater.*, 14:775–779, 2015.
- [24] F. Arnold. Absence of superconductivity in FeSe/Bi₂Se₃ near the two-dimensional limit. *Part A*, 2016.
- [25] H. Hertz. Über einen Einfluss des ultravioletten Lichtes auf die elektrische Entladung. *Annalen der Physik*, 267:983–1000, 1887.
- [26] A. Einstein. Über einen die Erzeugung und Verwandlung des Lichtes betreffenden heuristischen Gesichtspunkt. *Annalen der Physik*, 322:132–148, 1905.
- [27] A. Damascelli. Probing the electronic structure of complex systems by ARPES. *Phys. Scripta*, 2004:61, 2004.
- [28] M. P. Seah and W. A. Dench. Quantitative electron spectroscopy of surfaces: A standard data base for electron inelastic mean free paths in solids. *Surf. Interface Anal.*, 1:2–11, 1979.
- [29] S. Hüfner. *Photoelectron Spectroscopy*, volume 3rd edition. Springer, 2003.
- [30] S. Kevan. *Angle-Resolved Photoemission*. Elsevier, 1st edition, 1992.
- [31] A. Damascelli, Z. Hussain, and Z.-X. Shen. Angle-resolved photoemission studies of the cuprate superconductors. *Rev. Mod. Phys.*, 75:473–541, 2003.
- [32] P. Heimann, J. F. van der Veen, and D. E. Eastman. Structure-dependent surface core level shifts for the Au(111), (100), and (110) surfaces. *Solid State Commun.*, 38:595–598, 1981.
- [33] G. K. Wertheim, F. J. Disalvo, and S. Chiang. Sign and amplitude of charge density waves in 1T-TaS₂ and TaSe₂. *Phys. Lett. A*, 54:304–306, 1975.
- [34] N. Radutoiu and C. M. Teodorescu. Satellites in Ce 3d x-ray photoelectron spectroscopy of ceria. *Digest Journal of Nanomaterials and Biostructures*, 8:1535–1549, 2013.
- [35] S. Doniach and M. Šunjić. Many-electron singularity in x-ray photoemission and x-ray line spectra from metals. *J. Phys. C Solid State Phys.*, 3:285, 1970.
- [36] J. Végh. The shirley background revised. *J. Electron. Spectros. Relat. Phenomena*, 151:159–164, 2006.
- [37] Ph. Hofmann. *Surface Physics: An Introduction*. Wiley, 2013.

- [38] F. Besenbacher, E. Laegsgaard, K. Mortensen, U. Nielsen, and I. Stensgaard. Compact, high-stability, “thimble-size” scanning tunneling microscope. *Rev. Sci. Instrum.*, 59:1035–1038, 1988.
- [39] S. P. Møller, N. Hertel, and J. Nielsen. *Status and very first commissioning of the ASTRID2 synchrotron light source*. IPAC, IEEE, 2012.
- [40] Aarhus Centre for Storage Ring Facilities. On the web: <http://www.isa.au.dk>.
- [41] H. G. Füchtbauer, A. K. Tuxen, Z. Li, H. Topsøe, J. V. Lauritsen, and F. Besenbacher. Morphology and atomic-scale structure of MoS₂ nanoclusters synthesized with different sulfiding agents. *Top. Catal.*, 57:207–214, 2014.
- [42] C. Julian Chen. *Introduction to Scanning Tunneling Microscopy Press, 2007*. Oxford University Press, 2007.
- [43] E. Laegsgaard, L. Österlund, P. Thostrup, P. B. Rasmussen, I. Stensgaard, and F. Besenbacher. A high-pressure scanning tunneling microscope. *Rev. Sci. Instrum.*, 72:3537, 2001.
- [44] J. V. Barth, H. Brune, G. Ertl, and R. J. Behm. Scanning tunneling microscopy observations on the reconstructed Au(111) surface: Atomic structure, long-range superstructure, rotational domains, and surface defects. *Phys. Rev. B*, 42:9307, 1990.
- [45] D. P. Woodruff. Adsorbate structure determination using photoelectron diffraction: Methods and applications. *Surf. Sci. Rep.*, 62:1–38, 2007.
- [46] F. J. García de Abajo, M. A. Van Hove, and C. S. Fadley. Multiple scattering of electrons in solids and molecules: A cluster-model approach. *Phys. Rev. B*, 63:075404, 2001.
- [47] H. K. Onnes. The resistance of pure mercury at helium temperatures. *Commun. Phys. Lab. Univ. Leiden*, 12, 1911.
- [48] L. N. Cooper. Bound electron pairs in a degenerate fermi gas. *Phys. Rev.*, 104:1189–1190, 1956.
- [49] J. G. Bednorz and K. A. Müller. Possible high T_c superconductivity in the Ba-La-Cu-O system. *Zeitschrift für Physik B Condensed Matter*, 64:189–193, 1986.
- [50] J. J. Lee, F. T. Schmitt, R. G. Moore, S. Johnston, Y. T. Cui, W. Li, M. Yi, Z. K. Liu, M. Hashimoto, Y. Zhang, D. H. Lu, T. P. Devereaux, D. H. Lee, and

- Z. X. Shen. Interfacial mode coupling as the origin of the enhancement of T_c in FeSe films on SrTiO₃. *Nature*, 515:245–248, 2014.
- [51] M. H. Fang, H. M. Pham, B. Qian, T. J. Liu, E. K. Vehstedt, Y. Liu, L. Spinu, and Z. Q. Mao. Superconductivity close to magnetic instability in Fe(Se_{1-x}Te_x)_{0.82}. *Phys. Rev. B*, 78:224503, 2008.
- [52] J. J. Seo, B. Y. Kim, B. S. Kim, J. K. Jeong, J. M. Ok, J. S. Kim, J. D. Denlinger, S. K. Mo, C. Kim, and Y. K. Kim. Superconductivity below 20 K in heavily electron-doped surface layer of FeSe bulk crystal. *Nat. Commun.*, 7:11116, 2016.
- [53] C.-L. Song, Y.-L. Wang, Y.-P. Jiang, Z. Li, L. Wang, K. He, X. Chen, X.-C. Ma, and Q.-K. Xue. Molecular-beam epitaxy and robust superconductivity of stoichiometric FeSe crystalline films on bilayer graphene. *Phys. Rev. B*, 84:020503, 2011.
- [54] C.-L. Song, H.-M. Zhang, Y. Zhong, X.-P. Hu, S.-H. Ji, L. Wang, K. He, X.-C. Ma, and Q.-K. Xue. Observation of double-dome superconductivity in potassium-doped FeSe thin films. *Phys. Rev. Lett.*, 116:157001, 2016.
- [55] W. Zhang, Z. Li, F. Li, H. Zhang, J. Peng, C. Tang, Q. Wang, K. He, X. Chen, L. Wang, X. Ma, and Q.-K. Xue. Interface charge doping effects on superconductivity of single-unit-cell FeSe films on SrTiO₃ substrates. *Phys. Rev. B*, 89:060506, 2014.
- [56] F.-C. Hsu, J.-Y. Luo, K.-W. Yeh, T.-K. Chen, T.-W. Huang, P. M. Wu, Y.-C. Lee, Y.-L. Huang, Y.-Y. Chu, D.-C. Yan, and M.-K. Wu. Superconductivity in the PbO-type structure α -FeSe. *Proc. Natl. Acad. Sci.*, 105:14262–14264, 2008.
- [57] U. R. Singh, J. Warmuth, V. Markmann, J. Wiebe, and R. Wiesendanger. Structural and electronic properties of ultrathin FeSe films grown on Bi₂Se₃ (0001) studied by STM/STS. *J. Phys. Condens. Matter.*, 29:025004, 2016.
- [58] X. Liu, L. Zhao, S. He, J. He, D. Liu, D. Mou, B. Shen, Y. Hu, J. Huang, and X. J. Zhou. Electronic structure and superconductivity of FeSe-related superconductors. *J. Phys. Condens. Matter.*, 27:183201, 2015.
- [59] J. Paglione and R. L. Greene. High-temperature superconductivity in iron-based materials. *Nat. Phys.*, 6:645–658, 2010.
- [60] Q. L. He, H. Liu, M. He, Y. H. Lai, H. He, G. Wang, K. T. Law, R. Lortz, J. Wang, and I. K. Sou. Two-dimensional superconductivity at the interface of a Bi₂Te₃/FeTe heterostructure. *Nat. Commun.*, 5:4247, 2014.

- [61] S. Manna, A. Kamlapure, L. Cornils, T. Hänke, E. M. J. Hedegaard, M. Bremholm, B. B. Iversen, Ph. Hofmann, J. Wiebe, and R. Wiesendanger. Interfacial superconductivity in a bi-collinear antiferromagnetically ordered FeTe monolayer on a topological insulator. *Nat. Commun.*, 8:14074, 2017.
- [62] R. J. Cava, Huiwen Ji, M. K. Fuccillo, Q. D. Gibson, and Y. S. Hor. Crystal structure and chemistry of topological insulators. *J. Mater. Chem. C*, 1:3176–3189, 2013.
- [63] H. Zhang, C.-X. Liu, X.-L. Qi, X. Dai, Z. Fang, and S.-C. Zhang. Topological insulators in Bi_2Se_3 , Bi_2Te_3 and Sb_2Te_3 with a single dirac cone on the surface. *Nat. Phys.*, 5:438–442, 2009.
- [64] M. Michiardi. *Study of electronic states in novel materials: Topological insulators and rare-earth diantimonides*. PhD thesis, Aarhus University, 2015.
- [65] Ph. Hofmann. *Synchrotron-Radiation Studies of Topological Insulators*. Springer International Publishing, 2013.
- [66] L. Fu. Hexagonal warping effects in the surface states of the topological insulator Bi_2Te_3 . *Phys. Rev. Lett.*, 103:266801, 2009.
- [67] E. Frantzeskakis and M. Grioni. Anisotropy effects on rashba and topological insulator spin-polarized surface states: A unified phenomenological description. *Phys. Rev. B*, 84:155453, 2011.
- [68] I. A. Nechaev, R. C. Hatch, M. Bianchi, D. Guan, C. Friedrich, I. Aguilera, J. L. Mi, B. B. Iversen, S. Blügel, Ph. Hofmann, and E. V. Chulkov. Evidence for a direct band gap in the topological insulator Bi_2Se_3 from theory and experiment. *Phys. Rev. B*, 87:121111, 2013.
- [69] T. M. McQueen, A. J. Williams, P. W. Stephens, J. Tao, Y. Zhu, V. Ksenofontov, F. Casper, C. Felser, and R. J. Cava. Tetragonal-to-orthorhombic structural phase transition at 90 K in the superconductor $\text{Fe}_{1.01}\text{Se}$. *Phys. Rev. Lett.*, 103:057002, 2009.
- [70] A. J. Williams, T. M. McQueen, and R. J. Cava. The stoichiometry of FeSe. *Solid State Commun.*, 149:1507–1509, 2009.
- [71] T. M. McQueen, Q. Huang, V. Ksenofontov, C. Felser, Q. Xu, H. Zandbergen, Y. S. Hor, J. Allred, A. J. Williams, D. Qu, J. Checkelsky, N. P. Ong, and R. J. Cava. Extreme sensitivity of superconductivity to stoichiometry in $\text{Fe}_{1+\delta}\text{Se}$. *Phys. Rev. B*, 79:014522, 2009.

- [72] G. F. Chen, Z. G. Chen, J. Dong, W. Z. Hu, G. Li, X. D. Zhang, P. Zheng, J. L. Luo, and N. L. Wang. Electronic properties of single-crystalline $\text{Fe}_{1.05}\text{Te}$ and $\text{Fe}_{1.03}\text{Se}_{0.30}\text{Te}_{0.70}$. *Phys. Rev. B*, 79:140509, 2009.
- [73] W. Bao, Y. Qiu, Q. Huang, M. A. Green, P. Zajdel, M. R. Fitzsimmons, M. Zhernenkov, S. Chang, M. Fang, B. Qian, and et al. Tunable $(\delta\pi, \delta\pi)$ -Type Antiferromagnetic Order in α -Fe(Te,Se) superconductors. *Phys. Rev. Lett.*, 102:247001, 2009.
- [74] L. Liu, T. Mikami, M. Takahashi, S. Ishida, T. Kakeshita, K. Okazaki, A. Fujimori, and S. Uchida. Reversed anisotropy of the in-plane resistivity in the antiferromagnetic phase of iron tellurides. *Phys. Rev. B*, 91:134502, 2015.
- [75] A. Subedi, L. Zhang, D. J. Singh, and M. H. Du. Density functional study of FeS, FeSe, and FeTe: Electronic structure, magnetism, phonons, and superconductivity. *Phys. Rev. B*, 78:134514, 2008.
- [76] T. Bazhiron and M. L. Cohen. Effects of charge doping and constrained magnetization on the electronic structure of an FeSe monolayer. *J. Phys. Condens. Matter*, 25:105506, 2013.
- [77] P. Starowicz, H. Schwab, J. Goraus, P. Zajdel, F. Forster, J. R. Rak, M. A. Green, I. Vobornik, and F. Reinert. A flat band at the chemical potential of a $\text{Fe}_{1.03}\text{Te}_{0.94}\text{S}_{0.06}$ superconductor observed by angle-resolved photoemission spectroscopy. *J. Phys. Condens. Matter.*, 25:195701, 2013.
- [78] Z. P. Yin, K. Haule, and G. Kotliar. Kinetic frustration and the nature of the magnetic and paramagnetic states in iron pnictides and iron chalcogenides. *Nat. Mater.*, 10:932–935, 2011.
- [79] Z. P. Yin, K. Haule, and G. Kotliar. Fractional power-law behavior and its origin in iron-chalcogenide and ruthenate superconductors: Insights from first-principles calculations. *Phys. Rev. B*, 86:195141, 2012.
- [80] A. Ciechan, M. J. Winiarski, and M. Samsel-Czekala. Magnetic phase transitions and superconductivity in strained FeTe. *J. Phys. Condens. Matter*, 26:025702, 2014.
- [81] M. J. Han and S. Y. Savrasov. Doping driven $(\pi, 0)$ nesting and magnetic properties of Fe_{1+x}Te superconductors. *Phys. Rev. Lett.*, 103:067001, 2009.
- [82] M. D. Watson, S. Backes, A. A. Haghighirad, M. Hoesch, T. K. Kim, A. I. Coldea, and R. Valentí. Formation of hubbard-like bands as a fingerprint of strong electron-electron interactions in FeSe. *Phys. Rev. B*, 95:081106, 2017.

- [83] A. Cavallin, V. Sevriuk, K. N. Fischer, S. Manna, S. Ouazi, M. Ellguth, C. Tusche, H. L. Meyerheim, D. Sander, and J. Kirschner. Preparation and characterization of Bi_2Se_3 (0001) and of epitaxial FeSe nanocrystals on Bi_2Se_3 (0001). *Surf. Sci.*, 646:72–82, 2016.
- [84] D. D. dos Reis, L. Barreto, M. Bianchi, G. A. S. Ribeiro, E. A. Soares, W. Simões e Silva, V. E. de Carvalho, J. Rawle, M. Hoesch, C. Nicklin, W. P. Fernandes, J. Mi, B. B. Iversen, and Ph. Hofmann. Surface structure of Bi_2Se_3 (111) determined by low-energy electron diffraction and surface x-ray diffraction. *Phys. Rev. B*, 88:041404, 2013.
- [85] M. Bianchi, R. C. Hatch, D. Guan, T. Planke, J. Mi, B. B. Iversen, and Ph. Hofmann. The electronic structure of clean and adsorbate-covered Bi_2Se_3 : An angle-resolved photoemission study. *Semicond. Sci. Technol.*, 27:124001, 2012.
- [86] M. Schmid, A. Biedermann, H. Stadler, and P. Varga. Lattice mismatch dislocations in a preferentially sputtered alloy studied by scanning tunneling microscopy. *Phys. Rev. Lett.*, 69:925, 1992.
- [87] M. K. Wu, F. C. Hsu, K. W. Yeh, T. W. Huang, J. Y. Luo, M. J. Wang, H. H. Chang, T. K. Chen, S. M. Rao, B. H. Mok, C. L. Chen, Y. L. Huang, C. T. Ke, P. M. Wu, A. M. Chang, C. T. Wu, and T. P. Perng. The development of the superconducting PbO-type β -FeSe and related compounds. *Physica C Supercond.*, 469:340–349, 2009.
- [88] D. Huang, T. A. Webb, C.-L. Song, C.-Z. Chang, J. S. Moodera, E. Kaxiras, and J. E. Hoffman. Dumbbell defects in FeSe films: A scanning tunneling microscopy and first-principles investigation. *Nano Lett.*, 16:4224–4229, 2016.
- [89] P. Choubey, T. Berlijn, A. Kreisel, C. Cao, and P. J. Hirschfeld. Visualization of atomic-scale phenomena in superconductors: Application to FeSe. *Phys. Rev. B*, 90:134520, 2014.
- [90] C.-Li Song, Y.-L. Wang, Y.-P. Jiang, L. Wang, K. He, X. Chen, J. E. Hoffman, X.-C. Ma, and Q.-K. Xue. Suppression of superconductivity by twin boundaries in FeSe. *Phys. Rev. Lett.*, 109:137004, 2012.
- [91] T. Schlenk, M. Bianchi, M. Koleini, A. Eich, O. Pietzsch, T. O. Wehling, T. Frauenheim, A. Balatsky, J.-L. Mi, B. B. Iversen, J. Wiebe, A. A. Kha-jetoorians, Ph. Hofmann, and R. Wiesendanger. Controllable magnetic doping of the surface state of a topological insulator. *Phys. Rev. Lett.*, 110:126804, 2013.

- [92] K. Kuroda, M. Arita, K. Miyamoto, M. Ye, J. Jiang, A. Kimura, E. E. Krasovskii, E. V. Chulkov, H. Iwasawa, T. Okuda, K. Shimada, Y. Ueda, H. Namatame, and M. Taniguchi. Hexagonally deformed fermi surface of the 3D topological insulator Bi_2Se_3 . *Phys. Rev. Lett.*, 105:076802, 2010.
- [93] P. Zhang, P. Richard, T. Qian, Y.-M. Xu, X. Dai, and H. Ding. A precise method for visualizing dispersive features in image plots. *Rev. Sci. Instrum.*, 82:043712, 2011.
- [94] D. Liu, W. Zhang, D. Mou, J. He, Y.-B. Ou, Q.-Y. Wang, Z. Li, L. Wang, L. Zhao, S. He, Y. Peng, X. Liu, C. Chen, L. Yu, G. Liu, X. Dong, J. Zhang, C. Chen, Z. Xu, J. Hu, X. Chen, X. Ma, Q. Xue, and X. J. Zhou. Electronic origin of high-temperature superconductivity in single-layer FeSe superconductor. *Nat. Commun.*, 3:931, 2012.
- [95] S. He, J. He, W. Zhang, L. Zhao, D. Liu, X. Liu, D. Mou, Y.-B. Ou, Q.-Y. Wang, Z. Li, L. Wang, Yingying Peng, Y. Liu, C. Chen, L. Yu, G. Liu, X. Dong, J. Zhang, C. Chen, Z. Xu, X. Chen, X. Ma, Q. Xue, and X. J. Zhou. Phase diagram and electronic indication of high-temperature superconductivity at 65 K in single-layer FeSe films. *Nat. Mater.*, 12:605–610, 2013.
- [96] Y. S. Hor, A. Richardella, P. Roushan, Y. Xia, J. G. Checkelsky, A. Yazdani, M. Z. Hasan, N. P. Ong, and R. J. Cava. P-type Bi_2Se_3 for topological insulator and low-temperature thermoelectric applications. *Phys. Rev. B*, 79:195208, 2009.
- [97] T. J. Liu, X. Ke, B. Qian, J. Hu, D. Fobes, E. K. Vehstedt, H. Pham, J. H. Yang, M. H. Fang, L. Spinu, P. Schiffer, Y. Liu, and Z. Q. Mao. Charge-carrier localization induced by excess Fe in the superconductor $\text{Fe}_{1+y}\text{Te}_{1-x}\text{Se}_x$. *Phys. Rev. B*, 80:174509, 2009.
- [98] A. Eich, M. Michiardi, G. Bihlmayer, X. Zhu, J. Mi, B. B. Iversen, R. Wiesendanger, Ph. Hofmann, A. A. Khajetoorians, and J. Wiebe. Intra- and interband electron scattering in a hybrid topological insulator : Bismuth bilayer on Bi_2Se_3 . *Phys. Rev. B*, 90:155414, 2014.
- [99] J. Warmuth, A. Bruix, M. Michiardi, T.n Hä nke, M. Bianchi, J. Wiebe, R. Wiesendanger, B. Hammer, Ph. Hofmann, and A. A. Khajetoorians. Band-gap engineering by Bi intercalation of graphene on Ir(111). *Phys. Rev. B*, 93:165437, 2016.

- [100] Y. Xia, D. Qian, L. Wray, D. Hsieh, G. F. Chen, J. L. Luo, N. L. Wang, and M. Z. Hasan. Fermi surface topology and low-lying quasiparticle dynamics of parent $\text{Fe}_{1+x}\text{Te}/\text{Se}$ superconductor. *Phys. Rev. Lett.*, 103:037002, 2009.
- [101] Y. Zhang, F. Chen, C. He, L. X. Yang, B. P. Xie, Y. L. Xie, X. H. Chen, Minghu Fang, M. Arita, K. Shimada, H. Namatame, M. Taniguchi, J. P. Hu, and D. L. Feng. Strong correlations and spin-density-wave phase induced by a massive spectral weight redistribution in $\alpha\text{-Fe}_{1.06}\text{Te}$. *Phys. Rev. B*, 82:165113, 2010.
- [102] Z. K. Liu, R.-H. He, D. H. Lu, M. Yi, Y. L. Chen, M. Hashimoto, R. G. Moore, S.-K. Mo, E. A. Nowadnick, J. Hu, T. J. Liu, Z. Q. Mao, T. P. Devereaux, Z. Hussain, and Z.-X. Shen. Measurement of coherent polarons in the strongly coupled antiferromagnetically ordered iron-chalcogenide $\text{Fe}_{1.02}\text{Te}$ using angle-resolved photoemission spectroscopy. *Phys. Rev. Lett.*, 110:037003, 2013.
- [103] Z. R. Ye, Y. Zhang, F. Chen, M. Xu, J. Jiang, X. H. Niu, C. H. P. Wen, L. Y. Xing, X. C. Wang, C. Q. Jin, B. P. Xie, and D. L. Feng. Extraordinary doping effects on quasiparticle scattering and bandwidth in iron-based superconductors. *Phys. Rev. X*, 4:031041, 2014.
- [104] S.V. Hoffmann, Ch. Søndergaard, Ch. Schultz, Z. Li, and Ph. Hofmann. An undulator-based spherical grating monochromator beamline for angle-resolved photoemission spectroscopy. *Nucl. Instr. Meth. Phys. Res.*, 523:441–453, 2004.
- [105] P. Löptien, L. Zhou, J. Wiebe, a. a. Khajetoorians, J. L. Mi, B. B. Iversen, Ph. Hofmann, and R. Wiesendanger. Screening and atomic-scale engineering of the potential at a topological insulator surface. *Phys. Rev. B*, 89:085401, 2014.
- [106] T. Hänke, U. R. Singh, L. Cornils, S. Manna, A. Kamlapure, M. Bremholm, E. M. J. Hedegaard, B. B. Iversen, Ph. Hofmann, J. Hu, Z. Mao, J. Wiebe, and R. Wiesendanger. Reorientation of the diagonal double-stripe spin structure at Fe_{1+y}Te bulk and thin-film surfaces. *Nat. Commun.*, 8:13939, 2017.
- [107] A. Kamlapure, S. Manna, L. Cornils, T. Hänke, M. Bremholm, Ph. Hofmann, J. Wiebe, and R. Wiesendanger. Spatial variation of the two-fold anisotropic superconducting gap in a monolayer of $\text{FeSe}_{0.5}\text{Te}_{0.5}$ on a topological insulator. *Phys. Rev. B*, 95:104509, 2017.
- [108] K. Schouteden, K. Govaerts, J. Debehets, U. Thupakula, T. Chen, Z. Li, A. Netsou, F. Song, D. Lamoen, C. Van Haesendonck, B. Partoens, and K. Park. Annealing-induced Bi bilayer on Bi_2Te_3 investigated via quasi-particle-interference mapping. *ACS Nano*, 10:8778–8787, 2016.

- [109] S. Li, C. De La Cruz, Q. Huang, Y. Chen, J. W. Lynn, J. Hu, Y. L. Huang, F. C. Hsu, K. W. Yeh, M. K. Wu, and P. Dai. First-order magnetic and structural phase transitions in $\text{Fe}_{1+y}\text{Se}_x\text{Te}_{1-x}$. *Phys. Rev. B*, 79:054503, 2009.
- [110] F. Yang, L. Miao, Z. F. Wang, M.-Y. Yao, F. Zhu, Y. R. Song, M.-X. Wang, J.-P. Xu, A. I. V. Fedorov, Z. Sun, and et al. Spatial and energy distribution of topological edge states in single Bi(111) bilayer. *Phys. Rev. Lett.*, 109:016801, 2012.
- [111] X. Wu, S. Qin, Y. Liang, H. Fan, and J. Hu. Topological characters in $\text{Fe}(\text{Te}_{1-x}\text{Se}_x)$ thin films. *Phys. Rev. B*, 93:115129, 2016.
- [112] M. Bianchi, D. Guan, S. Bao, J. Mi, Bo B. Iversen, P. D. C. King, and Ph. Hofmann. Coexistence of the topological state and a two-dimensional electron gas on the surface of Bi_2Se_3 . *Nat. Commun.*, 1:128, 2010.
- [113] P. D. C. King, R. C. Hatch, M. Bianchi, R. Ovsyannikov, C. Lupulescu, G. Landolt, B. Slomski, J. H. Dil, D. Guan, J. L. Mi, E. D. L. Rienks, J. Fink, A. Lindblad, S. Svensson, S. Bao, G. Balakrishnan, B. B. Iversen, J. Osterwalder, W. Eberhardt, F. Baumberger, and Ph. Hofmann. Large tunable rashba spin splitting of a two-dimensional electron gas in Bi_2Se_3 . *Phys. Rev. Lett.*, 107:096802, 2011.
- [114] M. Michiardi, I. Aguilera, M. Bianchi, V. E. de Carvalho, L. O. Ladeira, N. G. Teixeira, E. A. Soares, C. Friedrich, S. Blügel, and Ph. Hofmann. Bulk band structure of Bi_2Te_3 . *Phys. Rev. B*, 90:075105, 2014.
- [115] J.A. Wilson and A.D. Yoffe. The transition metal dichalcogenides discussion and interpretation of the observed optical, electrical and structural properties. *Adv. Phys.*, 18:193–335, 1969.
- [116] M. Chhowalla, H. S. Shin, G. Eda, L.-J. Li, K. P. Loh, and H. Zhang. The chemistry of two-dimensional layered transition metal dichalcogenide nanosheets. *Nat. Chem.*, 5:263–275, 2013.
- [117] S. Nagata, T. Aochi, T. Abe, S. Ebisu, T. Hagino, Y. Seki, and K. Tsutsumi. Superconductivity in the layered compound 2H-TaS_2 . *J. Phys. Chem. Solids*, 53:1259–1263, 1992.
- [118] H. Zhang, L.-M. Liu, and W.-M. Lau. Dimension-dependent phase transition and magnetic properties of VS_2 . *J. Mater. Chem. A*, 1:10821–10828, 2013.

- [119] M. Kan, B. Wang, Y. H. Lee, and Q. Sun. A density functional theory study of the tunable structure, magnetism and metal-insulator phase transition in VS_2 monolayers induced by in-plane biaxial strain. *Nano Res.*, 8:1348–1356, 2015.
- [120] Y. Ma, Y. Dai, M. Guo, C. Niu, Y. Zhu, and B. Huang. Evidence of the existence of magnetism in pristine VX_2 monolayers ($X = \text{S}, \text{Se}$) and their strain-induced tunable magnetic properties. *ACS Nano*, 6:1695–1701, 2012.
- [121] H. Pan. Electronic and magnetic properties of vanadium dichalcogenides monolayers tuned by hydrogenation. *J. Phys. Chem. C*, 118:13248–13253, 2014.
- [122] N. Luo, C. Si, and W. Duan. Structural and electronic phase transitions in ferromagnetic monolayer VS_2 induced by charge doping. *Phys. Rev. B*, 95:205432, 2017.
- [123] Y. Guo, H. Deng, X. Sun, X. Li, J. Zhao, J. Wu, W. Chu, S. Zhang, H. Pan, X. Zheng, X. Wu, C. Jin, C. Wu, and Y. Xie. Modulation of metal and insulator states in 2D ferromagnetic VS_2 by van der waals interaction engineering. *Adv. Mater.*, 29:1700715, 2017.
- [124] E. B. Isaacs and C. A. Marianetti. Electronic correlations in monolayer VS_2 . *Phys. Rev. B*, 94:035120, 2016.
- [125] H. L. Zhuang and R. G. Hennig. Stability and magnetism of strongly correlated single-layer VS_2 . *Phys. Rev. B*, 93:054429, 2016.
- [126] D. W. Murphy, C. Cros, F. J. Di Salvo, and J. V. Waszczak. Preparation and properties of Li_xVS_2 ($0 \leq x \leq 1$). *Inorg. Chem.*, 16:3027–3031, 1977.
- [127] H. Moutaabbid, Y. Le Godec, D. Taverna, B. Baptiste, Y. Klein, G. Louprias, and A. Gauzzi. High-pressure control of vanadium self-intercalation and enhanced metallic properties in $1\text{T-V}_{1+x}\text{S}_2$ single crystals. *Inorg. Chem.*, 55:6481–6486, 2016.
- [128] M. Mulazzi, A. Chainani, N. Katayama, R. Eguchi, M. Matsunami, H. Ohashi, Y. Senba, M. Nohara, M. Uchida, H. Takagi, and S. Shin. Absence of nesting in the charge-density-wave system 1T-VS_2 as seen by photoelectron spectroscopy. *Phys. Rev. B*, 82:075130, 2010.
- [129] W. Bensch and J. Koy. The single crystal structure of V_5S_8 determined at two different temperatures: Anisotropic changes of the metal atom network. *Inorg. Chim. Acta*, 206:221–223, 1993.

- [130] N. D. Mermin and H. Wagner. Absence of ferromagnetism or antiferromagnetism in one- or two-dimensional isotropic Heisenberg models. *Phys. Rev. Lett.*, 17:1133, 1966.
- [131] B. Huang, G. Clark, E. Navarro-Moratalla, D. R. Klein, R. Cheng, K. L. Seyler, D. Zhong, E. Schmidgall, M. A. McGuire, D. H. Cobden, W. Yao, D. Xiao, P. Jarillo-Herrero, and X. Xu. Layer-dependent ferromagnetism in a van der waals crystal down to the monolayer limit. *Nature*, 546:270–273, 2017.
- [132] C. Gong, L. Li, Z. Li, H. Ji, A. Stern, Y. Xia, T. Cao, W. Bao, C. Wang, Y. Wang, Z. Q. Qiu, R. J. Cava, S. G. Louie, J. Xia, and X. Zhang. Discovery of intrinsic ferromagnetism in two-dimensional van der waals crystals. *Nature*, 546:265, 2017.
- [133] FIZ Karlsruhe. On the web: <http://icsd.fiz-karlsruhe.de/>.
- [134] A. Splendiani, L. Sun, Y. Zhang, T. Li, J. Kim, C.-Y. Chim, G. Galli, and F. Wang. Emerging photoluminescence in monolayer MoS₂. *Nano Lett.*, 10:1271–1275, 2010.
- [135] K. F. Mak, C. Lee, J. Hone, J. Shan, and T. F. Heinz. Atomically thin MoS₂: A new direct-gap semiconductor. *Phys. Rev. Lett.*, 105:136805, 2010.
- [136] H. Zeng, J. Dai, W. Yao, D. Xiao, and X. Cui. Valley polarization in MoS₂ monolayers by optical pumping. *Nat. Nano.*, 7:490–493, 2012.
- [137] K. S. Novoselov, D. Jiang, F. Schedin, T. J. Booth, V. V. Khotkevich, S. V. Morozov, and A. K. Geim. Two-dimensional atomic crystals. *Proc. Natl. Acad. Sci. U.S.A.*, 102:10451–10453, 2005.
- [138] P.-C. Yeh, W. Jin, N. Zaki, D. Zhang, J. T. Liou, J. T. Sadowski, A. Al-Mahboob, J. I. Dadap, I. P. Herman, P. Sutter, and R. M. Osgood. Layer-dependent electronic structure of an atomically heavy two-dimensional dichalcogenide. *Phys. Rev. B*, 91:041407, 2015.
- [139] S. Helveg, J. V. Lauritsen, E. Lægsgaard, I. Stensgaard, J. K. Nørskov, B. S. Clausen, H. Topsøe, and F. Besenbacher. Atomic-scale structure of single-layer MoS₂ nanoclusters. *Phys. Rev. Lett.*, 84:951, 2000.
- [140] S. Y. Lee, E. Ito, H. Kang, M. Hara, H. Lee, and J. Noh. Surface structure, adsorption, and thermal desorption behaviors of methaneselenolate monolayers on Au(111) from dimethyl diselenides. *J. Phys. Chem. C*, 118:8322–8330, 2014.

- [141] A. Baraldi, G. Comelli, S. Lizzit, M. Kiskinova, and G. Paolucci. Real-time X-ray photoelectron spectroscopy of surface reactions. *Surf. Sci. Rep.*, 49:169–224, 2003.
- [142] G. Eda, T. Fujita, H. Yamaguchi, D. Voiry, M. Chen, and M. Chhowalla. Coherent atomic and electronic heterostructures of single-layer MoS₂. *ACS Nano*, 6:7311–7317, 2012. PMID: 22799455.
- [143] P. J. Rous, J. B. Pendry, D. K. Saldin, K. Heinz, K. Müller, and N. Bickel. Tensor LEED: A technique for high-speed surface-structure determination. *Phys. Rev. Lett.*, 57:2951, 1986.
- [144] A. Spijkerman, J. L. de Boer, A. Meetsma, G. A. Wiegers, and S. van Smaalen. X-ray crystal-structure refinement of the nearly commensurate phase of 1T-TaS₂ in (3 + 2)-dimensional superspace. *Phys. Rev. B*, 56:13757, 1997.
- [145] Z. Wu, W. Li, M. N. Yogeesh, S. Jung, A. L. Lee, K. McNicholas, A. Briggs, S. R. Bank, M. A. Belkin, D. Akinwande, and Y. Zheng. Tunable graphene metasurfaces with gradient features by self-assembly-based moiré nanosphere lithography. *Adv. Opt. Mater.*, 4:2035–2043, 2016.
- [146] A. H. MacDonald and R. Bistritzer. Materials science: Graphene moiré mystery solved? *Nature*, 474:453–454, 2011.
- [147] S. G. Sørensen, H. G. Füchtbauer, A. K. Tuxen, A. S. Walton, and J. V. Lauritsen. Structure and electronic properties of in situ synthesized single-layer MoS₂ on a gold surface. *ACS Nano*, 8:6788–6796, 2014.
- [148] J. Barth, F. Gerken, and C. Kunz. Experimental study of the 3p-3d intershell interaction in Ca, Sc, Ti, V, and Cr metals. *Phys. Rev. B*, 31:2022, 1985.
- [149] G. Panaccione, M. Altarelli, A. Fondacaro, A. Georges, S. Huotari, P. Lacovig, A. Lichtenstein, P. Metcalf, G. Monaco, F. Offi, L. Paolasini, A. Poteryaev, O. Tjernberg, and M. Sacchi. Coherent peaks and minimal probing depth in photoemission spectroscopy of mott-hubbard systems. *Phys. Rev. Lett.*, 97:116401, 2006.
- [150] G. A. Sawatzky and D. Post. X-ray photoelectron and auger spectroscopy study of some vanadium oxides. *Phys. Rev. B*, 20:1546, 1979.
- [151] T. Nakamura, Y. Sugizaki, S. Ishida, K. Edamoto, and K. Ozawa. Growth of ultrathin vanadium oxide films on Ag(100). *Jpn. J. Appl. Phys.*, 55:075501, 2016.

-
- [152] F. Presel, N. Jabeen, M. Pozzo, D. Curcio, L. Omiciuolo, P. Lacovig, S. Lizzit, D. Alfè, and A. Baraldi. Unravelling the roles of surface chemical composition and geometry for the graphene–metal interaction through C1s core-level spectroscopy. *Carbon*, 93:187–198, 2015.
- [153] C. Tusche, A. Krasnyuk, and J. Kirschner. Spin resolved bandstructure imaging with a high resolution momentum microscope. *Ultramicroscopy*, 159:520–529, 2015.
- [154] N. Takeuchi, C. T. Chan, and K. M. Ho. Au(111): A theoretical study of the surface reconstruction and the surface electronic structure. *Phys. Rev. B*, 43:13899, 1991.